

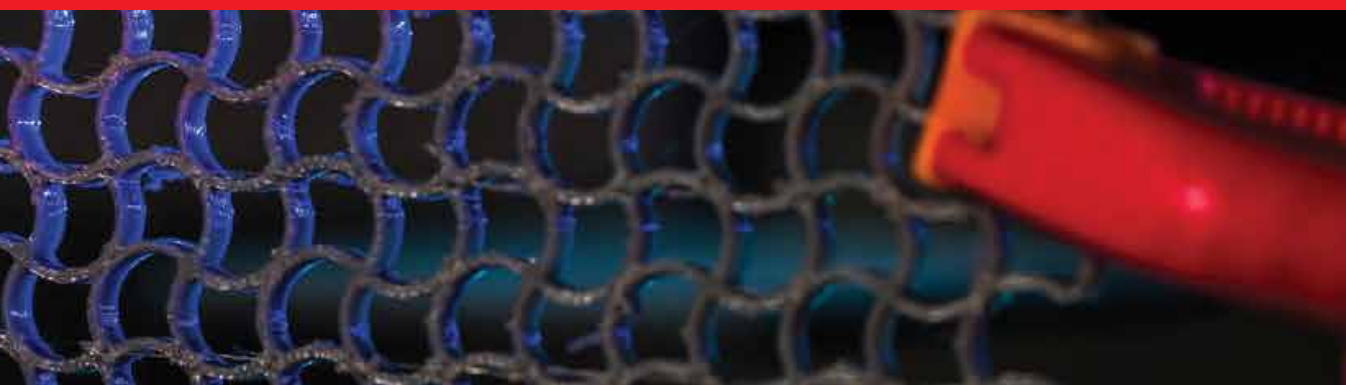


IntechOpen

# Plasmonic Nanostructures

Basic Concepts, Optimization and Applications

*Edited by Patrick Steglich*





---

Plasmonic Nanostructures  
- Basic Concepts,  
Optimization and  
Applications

*Edited by Patrick Steglich*

Published in London, United Kingdom

---

Plasmonic Nanostructures – Basic Concepts, Optimization and Applications

<http://dx.doi.org/10.5772/intechopen.97923>

Edited by Patrick Steglich

Contributors

Ehab Awad, Kaweri Gambhir, Agnikumar G. Vedeshwar, Rasha H. Mahdi, Hussein A. Jawad, Lu He, Dietrich R. T. Zahn, Teresa I. Madeira, Sanele Nyembe, Bambesiwe May, Andile Mkhohlakali, Nikiwe Mhlanga

© The Editor(s) and the Author(s) 2023

The rights of the editor(s) and the author(s) have been asserted in accordance with the Copyright, Designs and Patents Act 1988. All rights to the book as a whole are reserved by INTECHOPEN LIMITED. The book as a whole (compilation) cannot be reproduced, distributed or used for commercial or non-commercial purposes without INTECHOPEN LIMITED's written permission. Enquiries concerning the use of the book should be directed to INTECHOPEN LIMITED rights and permissions department ([permissions@intechopen.com](mailto:permissions@intechopen.com)).

Violations are liable to prosecution under the governing Copyright Law.



Individual chapters of this publication are distributed under the terms of the Creative Commons Attribution 3.0 Unported License which permits commercial use, distribution and reproduction of the individual chapters, provided the original author(s) and source publication are appropriately acknowledged. If so indicated, certain images may not be included under the Creative Commons license. In such cases users will need to obtain permission from the license holder to reproduce the material. More details and guidelines concerning content reuse and adaptation can be found at <http://www.intechopen.com/copyright-policy.html>.

Notice

Statements and opinions expressed in the chapters are those of the individual contributors and not necessarily those of the editors or publisher. No responsibility is accepted for the accuracy of information contained in the published chapters. The publisher assumes no responsibility for any damage or injury to persons or property arising out of the use of any materials, instructions, methods or ideas contained in the book.

First published in London, United Kingdom, 2023 by IntechOpen

IntechOpen is the global imprint of INTECHOPEN LIMITED, registered in England and Wales, registration number: 11086078, 5 Princes Gate Court, London, SW7 2QJ, United Kingdom

British Library Cataloguing-in-Publication Data

A catalogue record for this book is available from the British Library

Additional hard and PDF copies can be obtained from [orders@intechopen.com](mailto:orders@intechopen.com)

Plasmonic Nanostructures – Basic Concepts, Optimization and Applications

Edited by Patrick Steglich

p. cm.

Print ISBN 978-1-80356-002-1

Online ISBN 978-1-80356-003-8

eBook (PDF) ISBN 978-1-80356-004-5

# We are IntechOpen, the world's leading publisher of Open Access books Built by scientists, for scientists

**6,300+**

Open access books available

**171,000+**

International authors and editors

**190M+**

Downloads

**156**

Countries delivered to

Our authors are among the  
**Top 1%**

most cited scientists

**12.2%**

Contributors from top 500 universities



**WEB OF SCIENCE™**

Selection of our books indexed in the Book Citation Index  
in Web of Science™ Core Collection (BKCI)

Interested in publishing with us?  
Contact [book.department@intechopen.com](mailto:book.department@intechopen.com)

Numbers displayed above are based on latest data collected.  
For more information visit [www.intechopen.com](http://www.intechopen.com)





# Meet the editor



Patrick Steglich received his Ph.D. in industrial engineering in 2017 from the Università degli Studi di Roma Tor Vergata, Rome, Italy, with a focus on integrated photonics for communication and sensing. He is a research associate with the IHP—Leibniz-Institut für Innovative Mikroelektronik, Frankfurt (Oder), Germany, and also a lecturer in photonics and optical technologies at the Technische Hochschule, Wildau. His current research is focused on the hybrid integration of novel materials into a photonic integrated circuit technology for telecommunications and biosensing applications. Key applications include silicon-organic hybrid modulators and photonic biosensors for point-of-care and environmental monitoring.





# Contents

<b>Preface</b>	<b>XI</b>
<b>Section 1</b>	
Fundamentals and Optimization of Plasmonic Nanostructures	1
<b>Chapter 1</b>	<b>3</b>
The Influence of Geometry on Plasmonic Resonances in Surface- and Tip-Enhanced Raman Spectroscopy <i>by Lu He, Dietrich R.T. Zahn and Teresa I. Madeira</i>	
<b>Chapter 2</b>	<b>39</b>
Types of Nonlinear Interactions between Plasmonic-Excitonic Hybrids <i>by Kaweri Gambhir and Agnikumar G. Vedeshwar</i>	
<b>Chapter 3</b>	<b>61</b>
Infrared Nano-Focusing by a Novel Plasmonic Bundt Optenna <i>by Ehab Awad</i>	
<b>Section 2</b>	
Plasmonic Nanostructures for Biosensors and Diagnostics	77
<b>Chapter 4</b>	<b>79</b>
Application of Plasmonic Nanostructures in Molecular Diagnostics and Biosensor Technology: Challenges and Current Developments <i>by Sanele Nyembe, Andile Mkhohlakali, Bambesiwe May and Nikiwe Mhlanga</i>	
<b>Chapter 5</b>	<b>101</b>
Plasmonic Optical Nano-Antenna for Biomedical Applications <i>by Rasha H. Mahdi and Hussein A. Jawad</i>	



# Preface

Plasmonics refers to the generation, detection, and manipulation of signals at optical frequencies along metal-dielectric interfaces at the nanometer scale. Similar to electronics and photonics, plasmonics follows the trend of miniaturizing optical devices, and its applications can be found in sensing, microscopy, optical communications, and bio-photonics. The era of plasmonics started in the 1950s with the discovery of surface plasmon polaritons (SPPs). Another milestone for plasmonic research was the development of surface-enhanced Raman scattering in the mid-1970s. However, it took several more decades for plasmonics to receive a new wave of attention. In particular, new manufacturing technologies in micro-electronics have led to novel applications. SPPs are coherent electron oscillations traveling together with an electromagnetic wave along the interface between a dielectric material like silicon dioxide, glass or a polymer, and a metal like silver or gold. The SPP modes are strongly confined to their supporting interface, giving rise to strong light-matter interactions. In particular, the electron gas in the metal oscillates with the electromagnetic wave.

Plasmonics has attracted widespread attention in both science and industry, with the number of applications increasing rapidly. This book presents, in five chapters, a collection of recent advances in the broad field of plasmonics, including theory, simulation and fabrication aspects, along with emergent applications.

Lu He et al. provide a comprehensive analysis of the influence of geometry on plasmonic resonances in surface- and tip-enhanced Raman spectroscopy.

Kaweri Gambhir and Agnikumar G. Vedeshwar discuss the physical interactions of plasmons and their excitonic hybrids and describe their experimental realizations.

Ehab Awad investigates the design and optimization of a Bundt Optenna and demonstrates polarization insensitivity and ultra-broad bandwidth with a large fractional bandwidth within the near, short-wave, and mid-wave infrared bands.

Sanele Nyembe et al. discuss current challenges and developments of plasmonic nanostructures for molecular diagnostics and biosensors.

Hashem Rasha describes a plasmonic bowtie nano-antenna designed for biomedical applications.

We thank all the authors for their contributions. We also wish to express our thanks to the editorial staff of IntechOpen, particularly Ms. Karla Skuliber.

**Patrick Steglich**  
Technische Hochschule Wildau,  
Wildau, Germany



---

Section 1

Fundamentals and  
Optimization of Plasmonic  
Nanostructures

---



## Chapter 1

# The Influence of Geometry on Plasmonic Resonances in Surface- and Tip-Enhanced Raman Spectroscopy

*Lu He, Dietrich R.T. Zahn and Teresa I. Madeira*

### Abstract

Plasmonic nanostructures have attracted growing interest over the last decades due to their efficiency in improving the performance in various application fields such as catalysis, photovoltaics, (opto-)electronic devices, and biomedicine. The behavior of a specific metal plasmonic system depends on many factors such as the material, the size, the shape, and the dielectric environment. The geometry, that is, size and shape of both single plasmonic elements and patterned arrays of plasmonic nanostructures, plays an essential role, and it provides considerable freedom to tune the plasmonic properties of a single plasmonic nanostructure or any combination of nanostructures. This freedom is mainly used in the application fields of surface-enhanced Raman spectroscopy (SERS) and tip-enhanced Raman spectroscopy (TERS). In this context, the chapter encompasses how the geometry of the SERS-active plasmonic nanostructures and tips with/without metal substrates used in TERS influences the localized surface plasmon resonances of the plasmonic systems.

**Keywords:** plasmonics, metal nanostructures, geometry, SERS, TERS, simulation

### 1. Introduction

Almost 50 years ago, in 1974, Fleischmann et al. observed an enhanced Raman signal from a monolayer coverage of pyridine molecules adsorbed on a silver electrode [1]. Such unexpected behavior opened and initiated a new field of spectroscopic analysis including experimental and theoretical studies. Creighton's group [2] and Van Duyne's group [3] published similar results regarding pyridine molecules on silver anode surfaces using relatively low laser power and they brought forward different explanations for their results on the variation of Raman signal. Creighton explained that the enhanced signal is, on one hand, due to a surface effect increasing the molecular Raman scattering cross section and, on the other hand, due to the broadening of the electronic energy levels of molecules at rough metal surfaces, which may induce resonant Raman scattering from the adsorbed molecules *via* interaction with surface plasmons. Additionally, Van Duyne discovered that the enhancement of the

Raman signal is related to the roughness of the surface of the silver electrode and together they established the hypothesis that the phenomenon is due to electric field enhancement. Both explanations were accepted, but the electromagnetic enhancement was more prevailing [4] compared with the chemical or first-layer enhancement when molecules are in contact with metals.

In 1978, Moskovitz [5] put forward a possible explanation for the excitation-wavelength-dependent behavior observed by Creighton et al. [6] and Jeanmarie and Van Duyne [3]. He suggested that the observed behavior originates from the adsorbate-covered metal bumps on the metal surface, which could be considered as a two-dimensional colloid of metal spheres covered with the adsorbate and embedded in a dielectric medium on top of a smooth metal mirror. Additional absorption appears for those metal colloidal particles, for which interband electronic transitions exist [7].

Such resonance from the collective oscillation of conduction electrons on the metal surface and limited by the physical dimensions of the metal nanostructure is called localized surface plasmon resonance (LSPR). Typical metals used for plasmonic nanostructures are copper, silver, and gold [8, 9]. Due to the strong confinement of the electric field in the vicinity of such plasmonic metal nanostructures, they can be employed to break the optical diffraction limit and offer a vast range of applications in the fields of biology [10], chemistry [11–14], information [15], optical devices [16–19], and energy science [20, 21]. As a fast-developing field, researchers have studied plasmonic-related phenomena in all directions including the ultimate theoretical understanding from classical theory (e.g., Mie theory [22–26]) to quantum theory [27–29] aiming at providing a solid theoretical background to the main experimental and technological applications.

It is known that many factors, such as the material, size, shape, and dielectric environment, play important roles in determining the LSPR [30]. Among these factors, the geometry [31–37] of the plasmonic nanostructure provides the largest freedom and a straightforward way to tune the plasmonic resonance condition. Therefore, in this chapter, we focus on different geometries of plasmonic structures starting from introducing mathematical solutions for a single metal sphere representing a monomer system and two coupled metal spheres representing a dimer system. Then, we give a review on theoretical approaches that have been used in two powerful analytical techniques: SERS and TERS. Both experiment and simulation provide solid input to the understanding of the mechanisms and the principles of the techniques.

## **2. Theory on monomer and dimer systems**

### **2.1 Single metal sphere: monomer systems**

We refer to monomer systems when considering a single plasmonic nanostructure. Practically, for each system, in which metal nanoparticles are sparsely distributed in a dielectric environment, the interaction between the individual nanostructures can often be neglected so that each nanostructure can be considered as a monomer. Here, we address the equations for a single metal sphere regarding the light-matter interaction in detail [38–40], while the solution for further arbitrarily shaped single elements, which may appear more frequently in reality, is not derived, but related theoretical work can be found in refs. [41–46].

In the quasistatic approximation, light scattering by a spherical particle, the radius of which is  $a$  ( $a \ll \lambda$ ), in a uniformly distributed electric field of  $E = E_0 r \cos \theta$



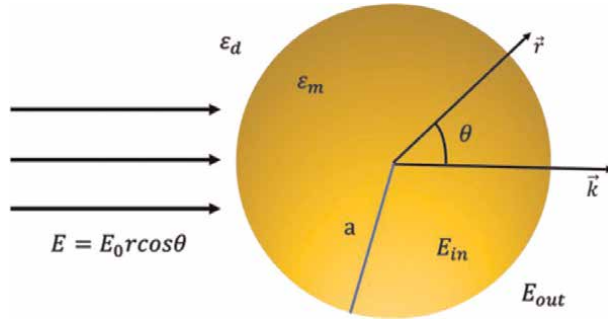


**Figure 1.** Schematic sketch of a metal nanosphere in an electric field [38].

(as shown in **Figure 1** [40]) is described by the Laplace equations for the scalar electric potential [38].

$$E_{in} = -\nabla\Phi_{in} \quad (1)$$

$$E_{out} = -\nabla\Phi_{out} \quad (2)$$

$$\nabla^2\phi_{in} = 0 \quad (r < a) \quad (3)$$

$$\nabla^2\phi_{out} = 0 \quad (r > a) \quad (4)$$

with the continuous boundary conditions

$$\phi_{in} = \phi_{out}, \quad \epsilon_m \frac{\partial\phi_{in}}{\partial r} = \epsilon_d \frac{\partial\phi_{out}}{\partial r} \quad (r = a) \quad (5)$$

$E_{in}$  and  $E_{out}$  indicate the electric fields inside and outside the metal particle with their electrical potential written as  $\phi_{in}(r, \theta)$  and  $\phi_{out}(r, \theta)$ .  $\epsilon_m$  and  $\epsilon_d$  are the dielectric functions of the metal sphere and the dielectric environment, respectively. If we consider that the electric field at infinite distance is not disturbed by the metal sphere, the solution of Eqs. (1)–(4) can be written as [38].

$$\phi_{in} = \frac{-3\epsilon_d}{\epsilon_m + 2\epsilon_d} E_0 r \cos\theta \quad (6)$$

$$\phi_{out} = -E_0 r \cos\theta + a^3 E_0 \frac{\epsilon_m - \epsilon_d}{\epsilon_m + 2\epsilon_d} \frac{\cos\theta}{r^2} \quad (7)$$

Eq. (7) indicates that the potential outside the sphere can be considered as an addition of the incident field  $-E_0 r \cos\theta$  and a dipole with its dipole moment defined according to Eq. (8) [38],

$$p = 4\pi a^3 \epsilon_0 \epsilon_m \frac{\epsilon_m - \epsilon_d}{\epsilon_m + 2\epsilon_d} E_0 \quad (8)$$

with its polarizability  $\alpha$  of [38]:

$$\alpha = 4\pi a^3 \frac{\epsilon_m - \epsilon_d}{\epsilon_m + 2\epsilon_d} \quad (9)$$

This is to say that we can consider a metal sphere, the dimension of which is much smaller than the wavelength of the incident light, as a simple dipole. Its polarizability is a function of the dielectric constant and size of the metal sphere.

Further derivation shows the cross sections for scattering and absorption are obtained from the scattered field radiated by this induced dipole interacting with the incident plane wave. They can be written as [38]:

$$C_{scattering} = \frac{k^4}{6\pi} |\alpha|^2 = \frac{8}{3} k^4 \pi a^6 \left| \frac{\epsilon_m - \epsilon_d}{\epsilon_m + 2\epsilon_d} \right|^2 \quad (10)$$

$$C_{absorption} = k \text{Im}\{\alpha\} = 4k\pi a^3 \text{Im}\left\{ \frac{\epsilon_m - \epsilon_d}{\epsilon_m + 2\epsilon_d} \right\} \quad (11)$$

where  $k$  is the wave vector of the incident light.

For a specific metal in a specific environment where  $\epsilon_d$  and  $\epsilon_m$  are defined and fixed, the absorption coefficient is proportional to the third power of the radius of the particle, while the scattering cross section is proportional to the sixth power of this radius. The efficiency of absorption dominates over the scattering efficiency when the particle size decreases.

Additionally, one can also notice a resonant enhancement for scattering and absorption when the condition  $\text{Re}(\epsilon_m + 2\epsilon_d) = 0$  is satisfied, which is called Fröhlich condition [30]. This resonance is due to resonant excitation of the dipole surface plasmon. With the Drude model of the dielectric function, the frequency of the dipole surface plasmon can be written as  $\omega_{sp} \approx \omega_p / \sqrt{3}$  with  $\omega_p$  corresponding to the plasma frequency of the bulk metal.

The theory mentioned above can only be applied to particles that are much smaller than the excitation wavelength so that we can consider the electromagnetic field uniformly distributed across the entire metal particle. For particles with dimensions comparable to the excitation wavelength, in which the electrical field can no longer be considered uniform across the particle, a modified long wavelength approximation (MLWA) based on perturbative corrections has to be used [47–49].

The localized surface plasmon resonances (LSPRs) of noble metal particles with sizes of  $>10$  nm were characterized well experimentally [50–53]. However, the characterization and understanding for sizes smaller than 10 nm is still poor and challenging from both experimental and theoretical points of view [54, 55]. This is mainly due to the fact that both quantum effects and surface interactions become important as the electrons interact more strongly with the surface including the spill-over of conduction electrons at the particle surface, which complicates geometrical analysis [56]; these effects cannot be described directly and solely by electrodynamics, and they require detailed calculations of the electronic structure for the actual atomic arrangements in the nanostructure of interest. In what concerns the experiments, the optical detection in the far field becomes difficult for small particles due to the size-dependent reduction in scattering intensity. In what concerns theory, time-dependent density functional theory-based methods are in general limited at present to particles with the sizes below 1–2 nm [57–59]. This mismatch between what can be achieved experimentally and what can be addressed theoretically make it difficult to benchmark both approaches.

## 2.2 Coupled elements: dimer systems

When we bring two or more single elements together, a new system is formed due to the interaction among those single elements and their light-matter interaction can

consequently be quite different. Here, we address a dimer system, which is composed of two metal spheres with a sufficiently small gap distance in the range of a few nanometers. These spheres are normally but not necessarily identical with respect to their size, geometry, and material.

A widely accepted and discussed theory stems from Nordlander [60], who gave an intuitive explanation to define the extinction cross section of dimer systems based on the gap distance between the nanoparticles. The dimer plasmons can be considered as a combination of bonding and antibonding states derived from the individual nanosphere plasmons. In this theory [61], the conduction electrons are considered as a charged and incompressible liquid sitting on top of rigid, positively charged ion cores. Ion cores are treated within the jellium approximation and the positive charge  $n_0$  is uniformly distributed within the particle boundaries [62]. The plasmon modes are considered as self-sustained deformations of the electron liquid. Only the surface charges are responsible for such deformation since the liquid is incompressible. Therefore, the surface charge for a single solid metal sphere can be written as [61]:

$$\sigma(\Omega, t) = n_0 e \sum_{l,m} \sqrt{\frac{l}{R^3}} S_{lm}(t) Y_{lm}(\Omega) \quad (12)$$

where  $Y_{lm}(\Omega)$  indicates the spherical harmonic of the solid angle  $\Omega$ ,  $R$  is the radius of sphere,  $S_{lm}$  represent the new degrees of freedom, and  $l$  is the angular momentum of a nanosphere. When the polar axis is chosen along the dimer axis, for a real representation that is adopted for the spherical harmonics, the interaction is diagonal in azimuthal quantum number  $m$ .

Therefore, the dynamics of the deformation is described by [61]:

$$L_s = \frac{n_0 m_e}{2} \sum \left[ \dot{S}_{lm}^2 - \omega_{S,l}^2 S_{lm}^2 \right] \quad (13)$$

where  $\omega_{S,l} = \omega_B \sqrt{\frac{l}{2l+1}}$  represents the solid sphere plasmon resonance and  $\omega_B = \sqrt{\frac{e^2 n_0}{m_e \epsilon_0}}$ , represents the bulk plasmon frequency,  $\dot{S}_{lm}$  represents the time derivative of the term  $S_{lm}$ . For the dimer system, when the distance between the centres of the two spheres is smaller than  $\lambda_B/4$ , retardation effects can be neglected and the dynamics of the plasmons is defined by the instantaneous Coulomb interaction between the surface charges as [61]:

$$V(D) = \int R_1^2 d\Omega_1 \int R_2^2 d\Omega_2 \frac{\sigma^1(\Omega_1) \sigma^2(\Omega_2)}{|\vec{r}_1 - \vec{r}_2|} \quad (14)$$

where  $D$  is the separation between the centres of the two spheres in a dimer system.

The left panel in **Figure 2a** shows the dimer plasmon energies as a function of dimer separation for plasmon polarizations along the dimer axis ( $m = 0$ ). At large separation, the interaction of plasmons on different nanoparticles is weak and the dimer plasmons are essentially bonding and antibonding combinations of plasmons of the same angular momentum  $l$  belonging to the nanoparticle.

When the separation is relatively large ( $\sim 35$  nm), the splitting of the bonding and antibonding dimer plasmons is symmetric. The splitting increases as their interaction increases. The bonding/antibonding configuration corresponds to the two dipole

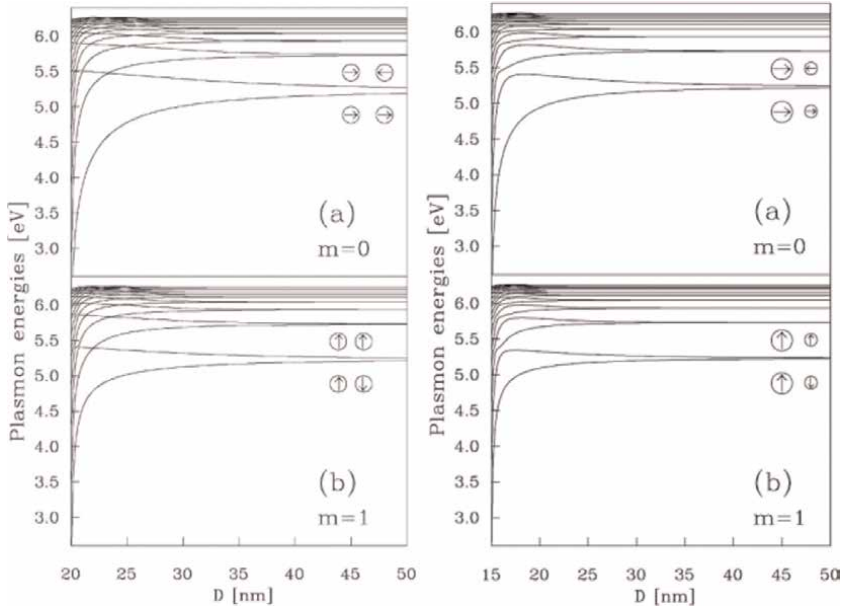


**Figure 2.** Calculated plasmon energies of a nanosphere dimer with identical sphere radii of 10 nm as a function of interparticle separation (left); calculated plasmon energies of a heterodimer as a function of interparticle separation (right) with two spheres that have different radii of 10 nm and 5 nm. Panels (a) is for the azimuthal quantum number  $m = 0$  and panels (b) for  $m = 1$ . The curves represent the bonding and antibonding dimer plasmons derived from the individual nanosphere plasmons with increasing angular momentum  $l$ . The arrows indicate the orientation of their dipole moments, see ref. [61].

moments moving in phase/out of phase (positive/negative parity of dipole moments or symmetric/asymmetric fields). For identical spheres, the net dipole moment of the negative parity plasmon (asymmetric field) is zero and they can hardly be excited by light, and they are therefore considered as dark plasmons, while the positive parity (symmetric field) plasmons are referred to as bright or luminous plasmons.

As the separation decreases, the splitting of  $l = 1$  plasmon becomes asymmetric. Since the lower energy plasmon branch shifts faster than the higher energy plasmon branch, the overall non-dipole-like red shift effect is caused by the interaction of the  $l = 1$  nanosphere plasmons with the higher  $l$  plasmons of the other nanosphere.

For the plasmons corresponding to  $m = \pm 1$  (polarization-oriented perpendicular to the dimer axis shown in **Figure 2** left panel (b)), the overall phenomena are similar. Note that the assignment for the bright/dark plasmons is reversed in this case because the perpendicular polarization coupling has opposite signs.

The right panel of **Figure 2** depicts the dimer plasmon for a heterodimer as a function of dimer separation. The behavior with the separation is different compared with results shown in the left panel of **Figure 2**. As the parity of the dimer is broken, the lines representing the dimer plasmon energies exhibit avoided crossings in the figure. All dimer plasmons with  $|m| \leq 1$  are bright.

As the separation decreases, the interactions get particularly strong when anti-bonding plasmons approach the bonding dimer plasmons of higher  $l$  manifolds, meaning that the higher  $l$  dimer plasmon also carries a finite dipole moment and becomes dipole active. Therefore, multiple peaks in the absorption spectra or a broad absorption region in the case of overlapping resonances are expected.

The result from the plasmon hybridization method is further compared with the finite difference time domain method (FDTD). And the results agree well with each other [63]. **Figure 3** from ref. [64] shows the scattering cross section of a nanosphere dimer system with radii of 40 nm and a separation distance varying from 0.5 to 200 nm compared with that of a monomer with a diameter of 80 nm. When the separation of the dimer is large, for example, 200 nm, the dimer system behaves the same as the monomer system, while decreasing the gap distance induces a shift toward higher energy and creating additional modes when the gap reaches 4 nm or even smaller distances.

Besides the above-mentioned hybridization method, another practical approach, which is used to describe coupled plasmon resonances in the so-called capacitive and conductive coupling regimes using an equivalent circuit model, was put forward by Benz et al. [65]. They claimed that such model can be used to calculate analytically the resonance wavelengths for different gap sizes, nanoparticle sizes, refractive indices, and linker conductivities.

To understand the dimer system further, different dimer systems are developed for fundamental studies. For example, Jeong et al. used an approach to fabricate plasmonic dimers in a very large scale with precise control of size, nanogap, material, and orientation [66]. They found that the optical response of each dimer is found to be identical with a highly uniform gap maintained across the array over centimeter distances. The existence of the transverse dipole mode and/or the longitudinal coupled resonance mode is highly dependent on the polarization of the incident light with respect to the dimer axis. A red shift can be observed with increasing gold nanoparticle size. Arbuz et al. recently studied the influence of the interparticle gap in dimers of gold nanoparticles on gold (Au), aluminum (Al), silver (Ag) films, and silicon (Si) wafers as substrates [67]. They claimed that the influence of the substrate vanishes when the dimer gap becomes larger than 2 nm. Nevertheless, the relation between the gap and the SERS intensity and enhancement factor is still under debate [68–71]. Also, Song et al. designed an experiment using an electromechanical method to tune the distance in the nm range between two Au nanoclusters as a strongly coupled plasmonic dimer, right before detrimental quantum effects set in. Different plasmon modes followed different trends as the bonding dipole (BDP) mode, a small blue shift

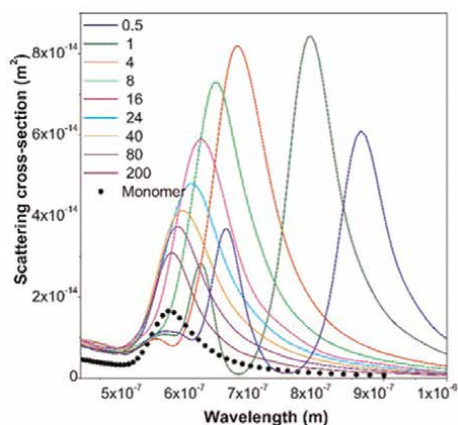


**Figure 3.**

*FDTD simulation results for the scattering cross section of a nanosphere dimer system with radii of 40 nm and a separation distance varying from 0.5 to 200 nm compared with that of a monomer [64].*

of the anti-bonding dipole (ADP) mode, and a negligible shift of anti-bonding vertical quadrupole (AVQP) mode with decreasing gap of the nanodisk dimer [72].

Dimer systems, as a basic metal nanostructure coupled system, provides a simple but very practical approximation for many application situations, especially in the two techniques, that is, SERS and TERS, that are discussed in the following sections.

### 2.3 Simulation on SERS and TERS

In the technical application of plasmonics, commonly used experimental configurations for SERS and TERS are shown in **Figure 4**. It is not only convenient but also reasonable to simplify the experimental configurations to simple spheres thus reducing a lot the computational cost in simulations. These schematic sketches of typical configurations include SERS in colloidal solution, SERS with a solid substrate, gap-mode SERS, TERS [73] and shell-isolated nanoparticle-enhanced Raman spectroscopy (SHINERS) [74–77].

To understand the impact of the geometry of plasmonic structures, simulations have an unbeatable advantage of freedom when designing the geometries. Besides straightforward experimental research, numerical simulations are gradually changing their role from a supporting approach to interpret the experimental results to a convenient and solid tool to investigate the mechanisms of plasmonic structures.

Various methods such as T-matrix [78–81], discrete dipole approximation (DDA) [82, 83], finite element method (FEM) [84, 85], and finite difference time domain (FDTD) [63, 64, 86] are used to address plasmonic systems. We can directly get the electric field distribution and use it for qualitative and even quantitative comparison with experiments. Classical theory based on solving Maxwell equations builds the backbone of many commonly used simulation tools while *ab initio* calculations may produce understanding beyond the knowledge obtained from classical theory. For a long time, we have tried to understand the mechanisms of light-matter interaction on metal nanoparticles. With the help of the fast development in the field of electronic and computer science, many computational methods were implemented to solve and

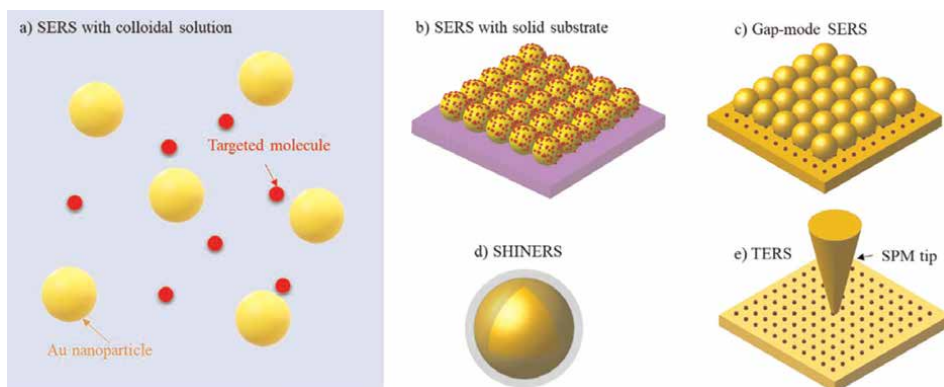


**Figure 4.** Schematic presentations of different configurations of plasmon enhanced Raman spectroscopy. a) a plasmonic colloidal solution as a substrate for SERS. b) A plasmonic solid substrate for SERS, comprising a glass or silicon support and plasmonic metal nanoparticles. c) Gap-mode SERS. d) Shell-isolated nanoparticle-enhanced Raman spectroscopy (SHINERS) uses nanoparticles coated with a layer of a dielectric material. e) TERS, the nanoparticles are replaced by a single metallic scanning probe microscope (SPM) tip [73].

visualize this problem. As solving the Maxwell equations is the core mission in this field, solvers for a particular design have been developed in the form of either integral or differential equations [87, 88].

**Table 1** [89] provides a comparison of the most used simulation tools for plasmonic structures.

Method	Computation Time for Au sphere with radius $< \lambda$	Advantages	Disadvantages
Mie Theory	<i>Rapid</i> —a few milliseconds per individual frequency	<ul style="list-style-type: none"> <li>• Rapid computation time.</li> <li>• Can also be used to compute the optical response of coated spheres.</li> </ul>	<ul style="list-style-type: none"> <li>• Applicable only to spherically symmetric particles.</li> <li>• Not possible to include a substrate interaction, therefore difficult to replicate many experiments.</li> </ul>
T-Matrix	<i>Rapid</i> —a few milliseconds—per individual frequency.	<ul style="list-style-type: none"> <li>• Rapid computation time.</li> <li>• Wide range of geometries supported.</li> <li>• Also possible to include a substrate interaction</li> </ul>	<ul style="list-style-type: none"> <li>• Computations are numerically unstable for elongated or flattened objects (the matrices are truncated during computation—rounding errors become significant and accumulate rapidly)</li> </ul>
DDA	<i>Moderate</i> —depends on number of dipoles, and separation. Typically 50s per individual frequency.	<ul style="list-style-type: none"> <li>• Can be used to evaluate any arbitrary-shaped particle by specifying a tabulated list of dipole locations</li> </ul>	<ul style="list-style-type: none"> <li>• Convergence criterion:  <math> n/ked  &lt; 1</math>  <math>n</math> = complex refractive index  <math>k</math> = wavevector  <math>d</math> = inter-dipole separation (Not possible to solve for high aspect ratio / elongated particles, or those having a large refractive index)</li> </ul>
FEM	<i>Lengthy</i> —typically 150 s per individual frequency when using an element length of 3 nm. A compromise is made between the computation time and element length.	<ul style="list-style-type: none"> <li>• Can be used to evaluate the scattered field distribution of any arbitrary-shaped particle.</li> <li>• The use of a non-regular tetrahedral adaptive mesh for the FEM simulation allows for a more accurate approximation of curved surfaces.</li> </ul>	<ul style="list-style-type: none"> <li>• Computation time is lengthy.</li> </ul>
FDTD	<i>Lengthy</i> —a broadband response is computed across a wide frequency range, typically taking $\approx 3$ hours to cover visible frequencies. A compromise made between the computation time and element length.	<ul style="list-style-type: none"> <li>• Can be used to evaluate scattering parameters from any arbitrary-shaped particle.</li> </ul>	<ul style="list-style-type: none"> <li>• Computation time is lengthy.</li> <li>• Permittivity values have to be specified over much wider frequency range than just the range of interest. The Drude-Lorentz model may not be an accurate representation of experimental data.</li> </ul>

**Table 1.** Comparison on computation time, advantages, and disadvantages of different computational techniques [89].

Among above-mentioned simulation methods, the finite element method (FEM) and the finite difference time domain (FDTD) method are the most commonly and widely used methods commercially available nowadays. In brief, FEM reduces the complex partial differential equations to simple algebraic equations. This method gives the approximate results at each discrete number of points over the domain. To solve the problem, it divides the whole problem into various numbers of discrete units generally termed as mesh elements. FEM can be applied to various physical problems such as structural analysis, fluid flow, electromagnetic potential, and mass transport [90]. FDTD, on the other hand, is usually suitable to solve transient change processes of a field under external excitation. If a pulsed excitation source is used, a single solution can yield a response over a wide-frequency band. Time domain methods have reliable accuracy and faster computational speed, and can truly reflect the nature of electromagnetic phenomena, especially in research areas requiring time domain measurements [91]. FDTD is more useful for nonlinear materials with offering a large range of wavelength-dependent dielectric constants and broadband simulations especially for the transient studies, while FEM benefits from unstructured gridding and is therefore more promising for higher-order curved elements with the advanced FEM codes [89, 92].

One of the most used simulation tools based on the FEM method is COMSOL Multiphysics [93]. This software includes various working packages for a variety of applications, among which the Wave Optics module is the one specifically used for plasmonic studies, because it enables to handle objects, the dimensions of which are comparable or smaller than the probing wavelength [94]. All modeling formulations are based on Maxwell's equations together with material laws for propagation in various media. The modeling capabilities are accessed *via* predefined physics interfaces, which allow the user to set up and solve the electromagnetic models in two- and three-dimensional spaces. The modeling of electromagnetic fields and waves can be performed in the frequency domain, time domain, eigenfrequency, and mode analysis. The modeling typically follows the sequence: definition of the geometry, selection of materials, selection of a suitable Wave Optics interface, definition of boundaries and initial conditions, definition of the finite element mesh, selection of a solver, and visualization of the results [94]. Most of the simulations presented in both SERS and TERS sections were performed with this tool.

### 2.3.1 SERS

In the typical SERS configuration shown in **Figure 4a**, computer simulations showed that spherical Au and Ag NPs as monomers cannot generate a strong localized electric field on their surface [95], and nevertheless, they carry on being most widely used options in SERS and TERS experiments, where high-quality signals can be obtained from different analytes, due to their easy and fast synthesis. Since a main task in SERS and TERS research is to increase the sensitivity of the plasmonic systems, other alternative geometric structures have been investigated, in which the aspect ratio of the spheroid structures is investigated: particles with prolate or oblate spheroid geometries [96]. A practical approximation in ref. [97] shows the possibility to use a Taylor expansion to numerically predict the extinction spectra of metallic spheroidal particles for a wide range of the geometric aspect ratios.

For configurations as shown in **Figure 4b** and **c**, classical electrodynamics provides a good description down to gap distances of the order of  $>1$  nm, after which quantum and non-local theory approaches have to be used [98–100]. The EM enhancement



continues until the distance between two metal surfaces becomes so small that electron spill-out and non-local effects become important, eventually leading to electronic tunneling and electrical shortcut [101]. Such phenomena are observed by simply bringing two or more spherical NPs close enough experimentally [102–104].

It is worth to mention that besides the spherical nanostructures in **Figure 4** other nanostructures, such as mesoporous gold particles [105], nanostars/flowers [106–113] or spiky structures/superstructures [114, 115], nanoshells [116], nanocubes [117–122], and hollow-structured particles [109, 112], have been considered. For those as SERS substrates, their edges work as hotspots concentrating the electromagnetic field of the probing light into small volumes. This enhances the local electromagnetic (EM) field near the edges of these metal nanostructures. The “hotspot” areas utilize the field enhancement properties of the metal nanostructures to amplify the usually weak Raman scattering signals.

Another way to boost the hotspots is to bring two or more particles in close vicinity. Therefore, many agglomerated structures are practically used to increase the SERS enhancement employing the interaction among the single monomers to fulfill the “dimer” condition, such as clusters [123], trimers [67, 124–128], tetramers [125, 129, 130], chains [131, 132], and arrays [133–137]. Detailed studies to understand such agglomerates were performed by several groups. Sergiienko et al. investigated the influence of NP agglomeration on the SERS signal [127]. The study was carried out on monomers, dimers, and trimers. In comparison with a single NP, the plasmonic absorption for dimers exhibits a new band at longer wavelength (red shift) due to the interparticle plasmonic coupling. Theoretically, the interparticle plasmonic coupling leads to more enhancement and red shifts the plasmonic absorption band with increasing degree of aggregation. When the nanoparticles in a chain are brought closer to each other (gaps decreasing from 2.5 to 0.5 nm), the maximum field enhancement at the gap becomes nearly 10 times larger and aggregation causes a large red shift of more than 200 nm. Overall, the SERS enhancement factor (EF) increases by 43% in average upon dimerization and 96% upon trimerization for both AuNPs and AgNPs. However, the maximum ratio of EFs for some dimers to the mean EF of monomers can be as high as 5.5 for AgNPs on gold substrates. For dimerization and trimerization of gold and silver NPs on silicon, the mean EF increases by 1–2 orders of magnitude relative to the mean EF of single NPs. Therefore, the hotspots in the interparticle gap between gold nanoparticles rather than hotspots between Au nanoparticles and substrate dominate the SERS enhancement for dimers and trimers on a silicon substrate. Raman-labeled noble metal nanoparticles on plasmonic metal films generate on average SERS enhancement of the same order of magnitude for both types of hotspot zones (i.e., NP/NP and NP/metal film). A summary of these results is presented in **Figure 5**. More details about this work can be found in ref. [124]

A SERS substrate can be composed of both monomer and dimer metal structures placed on metal/non-metal substrates. Arrays, as one of the important configurations, have been utilized in many fields [66, 138–140]. The fabrication of plasmonic arrays is also versatile including both top-down and bottom-up methods as described, for example, in ref. [138] and for instance, nanogap arrays using photolithography for nanogap arrays with swelling-induced nano-cracking [141], superimposition metal sputtering [135], and direct writing [142].

Among such methods, the so-called nanosphere lithography (NSL) using self-assembled nanospheres as a shadow mask for metal deposition is a typical cost-efficient and fast technique [143, 144]. NSL details are reviewed elsewhere [145]. Various metals can be used, such as silver, gold, copper, and aluminum. SEM images

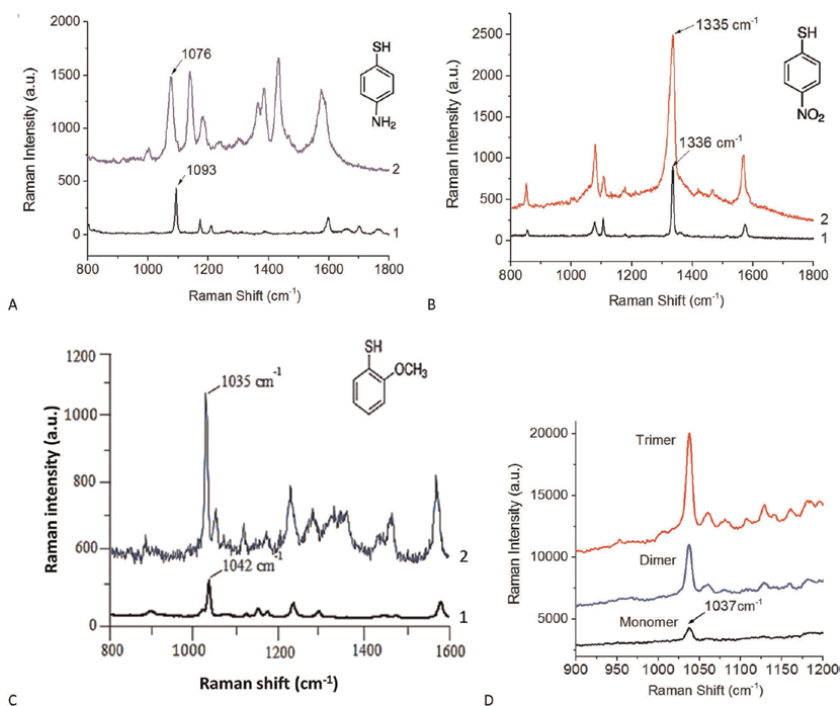


**Figure 5.** Raman and SERS spectra of analytes adsorbed on 60 nm Au NPs on an Au film: (A) 4-aminothiophenol, 1—Raman, 2—SERS, (B) 4-nitrobenzenethiol, 1—Raman, 2—SERS, (C) 2-methoxythiophenol, 1—Raman, 2—SERS, (D) SERS spectra of 2-methoxythiophenol (monomer, dimer, and trimer) [127].

of such typical structures are shown in **Figure 6**. Tuning the plasmon resonance frequency of such structure can be performed in the range from the near infrared to the blue spectral using different metals and by annealing them at different temperatures [146]. This tuning is simply based on the change of the shape of each metal nanotriangle (NT) from triangular to roundish for the case of Au and Ag. For Cu and

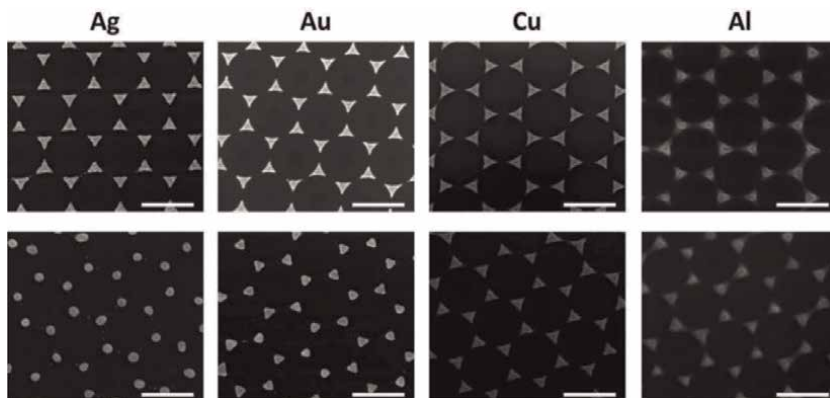


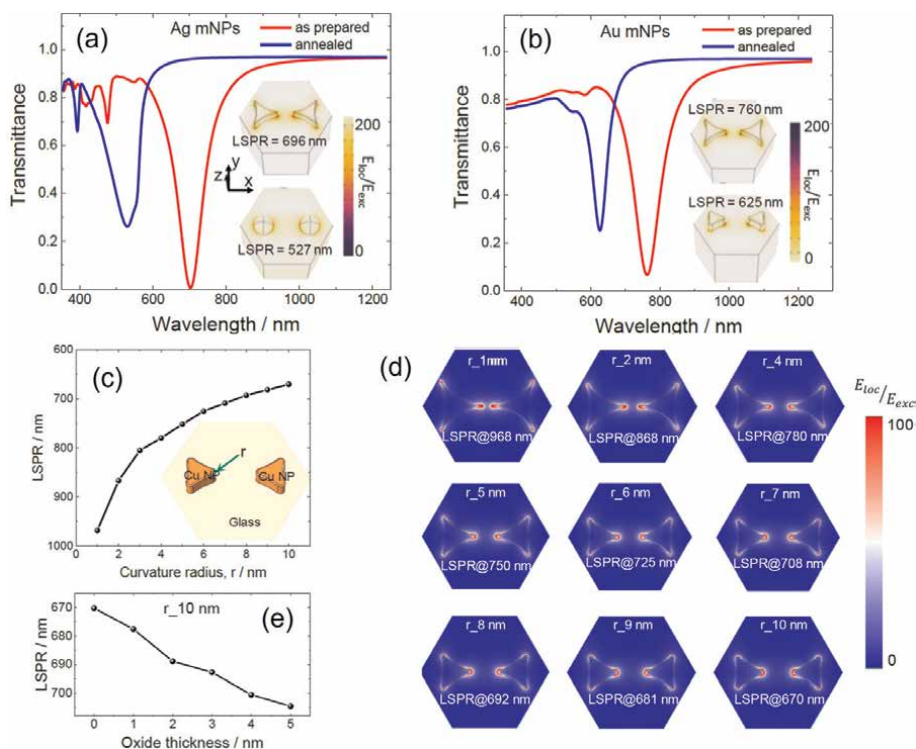
**Figure 6.** SEM images of the nanostructures prepared by nanosphere lithography. Top row shows the structures as deposited and the bottom row after annealing at 500°C. The scale bar is 500 nm in all images [146].

Al, the change in shape is not so dramatic as they form a dense oxide layer *via* annealing thus preventing further shape changes (see **Figure 6**).

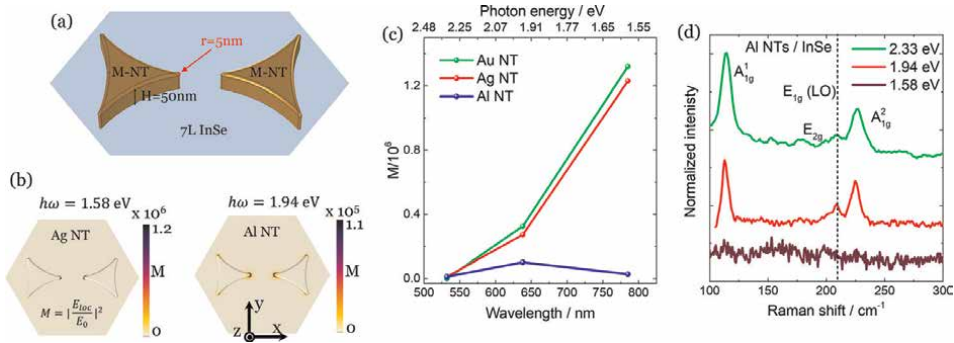
FEM simulations were performed using COMSOL 5.6 Wave Optic module [94]. The results are shown in **Figure 7**. There clearly is a blue shift of the resonant wavelength with increasing annealing temperature, that is, change of the shape for Ag, Au, and Cu arrays (**Figure 7a–c**), which is the main reason for the variation of the plasmonic resonance in this scenario. Additionally, the simulation for the Cu arrays is performed by adding a copper monoxide layer with the different thicknesses shown in **Figure 7c**. The results on the LSPR position support the hypothesis derived from the experimental results that annealing above 400°C produces thicker layers of copper oxide [146]. The electric field distribution (**Figure 7e**) reveals the position of the highest local enhancement for different copper oxide layer thicknesses.

The optical behavior of the metal NTs as a function of different annealing temperatures is a straightforward example of the flexibility in tuning the LSPR. Nanosphere lithography also allows other array structures to be fabricated, such as nanovoids [147] and “hedgehog-like” nanosphere arrays [148].

The metal nanotriangle structures have widely been used to study 2D materials, such as indium selenide (InSe) as shown in **Figure 8** [149]. One up to seven layers of InSe were deposited on arrays of plasmonic NTs composed of different metals. To



**Figure 7.** Simulated transmission spectra and the electric field enhancement distribution at the LSPR position using geometries corresponding to as prepared and annealed Ag NPs (a) and Au NPs (b). Simulated LSPR positions vs. geometry change in a Cu array by changing the radius of the edge of the Cu triangles shown in the inset as a sketch mimicking the change of the geometry at the lower annealing temperature shown in (c) and the electric field enhancement distribution for Cu arrays at LSPR conditions shown in (d); (e) simulated LSPR for further increase of the oxide thickness mimicking the situation as annealing temperature further increases [146].


**Figure 8.**

FEM simulation of plasmonic coupling between InSe and metal nanotriangles (MNTs). (a) Sketch of the model used in the FEM simulation of InSe/metal NTs. (b) Simulated electric field intensity  $M$  distribution at two different wavelengths for Ag and Al NTs. (c) Absolute value of calculated maximum  $M$  at three different excitations. A similar plasmonic behavior is expected for Ag and Au NTs on InSe for three selected wavelengths, while InSe with Al NTs shows a maximum at 1.94-eV excitation. (d) Raman spectra of 7 L InSe with Al NTs acquired under three different wavelengths [149].

study the enhancement behavior, simulations were performed using the same conditions as in the experiment. The enhancement factor,  $M$ , is defined as the square of the local electric field strength enhancement. We can see dramatic enhancement for gold and silver nanotriangles (NTs) with excitation energy of 1.58 eV and a relatively large enhancement at 1.94 eV.

### 2.3.2 TERS

TERS is another important experimental technique based on plasmonic enhancement. In a typical TERS configuration, there is a metal tip that is used for scanning a substrate usually decorated with the analytes, for example, molecules or nanostructures. If the substrate is a metal, then such a configuration is called gap-mode TERS. One of the critical targets in this technique is to maximize the TERS signal enhancement and achieve very good spatial resolution in the nanometer range, well below the diffraction limit of light. Here, gold and silver are the two preferred materials for the plasmonic tips. For both materials, their LSPRs locate in the near infrared to visible range, where laser wavelengths are available to match the LSPR. Therefore, most of the experimental and simulation studies are performed using these two materials. Additionally, Au is normally the first choice because it is more chemically stable when exposed to air, enabling its use for longer periods of time, while Ag tends to form sulfides when exposed to air deteriorating the TERS performance [150].

### 2.4 Tip effects

A “sharp” metallic tip promises good spatial resolution. Therefore, as the most critical component in TERS, the tip is considered as a sharp “corner” of a metal rod. In the macroscopic world, a spark would form at the end of a long metal rod due to lightning bolt during a thunderstorm, and similarly in the nano-world, this effect also plays a vital role and contributes to the TERS signal enhancement. This was first explained in 1980 by Gersten and Nitzan [151] and then in 1982 by Wokaun [152] using the formulation of depolarization factors.

Considering a metallic ellipsoid with the major axis  $a$  and minor axis  $b$  with  $a, b \ll \lambda$ , so that the electrostatic approximation can be utilized. A uniform electric field  $E_L$  is applied along the major axis, and this leads to a uniform polarization density within such an ellipsoid [152].

$$P = \frac{1}{4\pi} \frac{\epsilon_{\text{ellip}} - 1}{1 + (\epsilon_{\text{ellip}} - 1)A_a} E_L \quad (15)$$

Then, the field at the tip of the ellipsoid can be written as:

$$E_{\text{tip}} = \frac{(1 - A_a)(\epsilon_{\text{ellip}} - 1)}{1 + (\epsilon_{\text{ellip}} - 1)A_a} E_L + E_L \quad (16)$$

where  $\epsilon_{\text{ellip}}$  is the dielectric constant of the ellipsoid material and the  $A_a$  is the depolarization factor defined as:

$$A_a = \frac{ab^2}{2} \int_0^\infty \frac{ds}{(s + a^2)R} \quad (\alpha = a, b) \quad (17)$$

with  $R^2 = (s + a^2)(s + b^2)^2$ . For a sphere,  $A_a = \frac{1}{3}$  and for a prolate ellipsoid with ratio  $a : b = 3 : 1$ ,  $A_a = 0.1087$ . The prominent effect that the depolarization factor gives is the shift of the plasmon resonance frequency, that is, when the denominators in Eq. (15) and Eq. (16) approach zero at a specific wavelength [152].

Now, we consider the nanoparticle dipole moment  $\mu$  obtained by integrating Eq. (15) over the whole volume of the nanoparticle. This leads to  $\mu = 4\pi ab^2 P/3$  [152].

The field of the nanoparticle is determined by the simple dipolar field of  $\mu$  when at large distance. However, the situation changes when we look at the tip of the ellipsoid particle. A factor  $\gamma$  must be considered since the specific shape concentrates the field on the narrower parts of the structure. This phenomenon is called the lightning rod effect. We can then rewrite the Eq. (16) in a form of dipolar field  $E_{\text{dipolar}} = 2\mu/a^3$  and the new  $E_{\text{tip}}$  is written as [152].

$$E_{\text{tip}} = \gamma E_{\text{dipolar}} + E_L \quad \text{where } \gamma = \frac{3}{2} \left(\frac{a}{b}\right)^2 (1 - A_a) \quad (18)$$

We can see that for a sphere,  $\gamma = 1$  with  $a = b$  and therefore,  $A_a = \frac{1}{3}$ . For a prolate where  $a : b = 3 : 1$ ,  $\gamma = 12$ . In the more extreme situation with a needle-like ellipsoid, we have  $A_a \approx 0$  and  $\gamma \approx \frac{3}{2} \left(\frac{a}{b}\right)^2$ .

To calculate the total Raman enhancement, that is, an analyte molecule, for instance, is beneath the TERS tip, we consider the large Raman molecular moment that is induced by the intense local field at the ellipsoid and then the polarization of the ellipsoid induced by the molecular field. For simplicity, we can treat both the molecule and the ellipsoid as point dipoles. The molecular dipole field in turn polarizes the ellipsoid, giving an ellipsoid dipole at the Stokes frequency  $\omega_s$ . This added-up molecular dipole is larger than the usual Raman molecular dipole by a factor of [152].

$$f = \frac{4}{9} \frac{\epsilon(\omega_s) - 1}{[\epsilon(\omega_s) - 1]A_a + 1} \times \frac{\epsilon(\omega) - 1}{1 + [\epsilon(\omega) - 1]A_a} \left(\frac{b^2}{a^2}\right)^2 \quad (19)$$

The Raman intensity enhancement is then given by  $|f|^2$ . Note that the depolarization factor  $A_a$  can be approximately written as follows when  $a/b$  is very large [152].

$$A_a \sim \left(\frac{b}{a}\right)^2 \ln\left(\frac{a}{b}\right) \quad (20)$$

The lightning rod effect can be critical when simulating the electric field enhancement using geometrical simplifications. Therefore, for a tip geometry that is considered as a single sphere, the contribution to the signal enhancement due to the lightning rod effect is neglected.

The two most important aspects in TERS are the TERS enhancement factor (EF) and the spatial resolution. The TERS EF scales with  $\left(\frac{E_{loc}}{E_{inc}}\right)^4$ , where  $E_{loc}$  is the local electric field and  $E_{inc}$  is the incident electric field. The following classical theory provides a straightforward understanding [153]. To define the spatial resolution, the authors built a straightforward model for the TERS tip as shown in **Figure 9**. Here, the geometry of the tip can be approximated as a metal sphere, for which the solution was introduced in the previous section. The full-width at half maximum (FWHM) of the field distribution (mind that the real TERS spatial resolution is actually derived from the fourth power of the local electric field distribution) along the horizontal direction under the tip apex at a specific distance  $d$  from the tip apex [153]:

$$FWHM = 1.346(R + d) \quad (21)$$

The derived term indicates a supreme confined region of the local field, which is limited by the radius of the metal sphere or the curvature radius of a tip [154].

Simulations for an Ag tip with varying geometrical parameters were performed using COMSOL in ref. [155]. In this systematic simulation work, the simulated tip length, the tip radius, and the conical tip angle are varied [155]. As can be seen in **Figure 10**, there is a dramatic difference of the field enhancements between short and long tips, while a short, truncated tip can produce a better enhancement than a long one because of the excitation of the localized plasmon resonance. Regarding the tip radius, there is a significant improvement of the field enhancement observed when  $r$  decreases from 20 to 10 nm. Finally, the setting of the cone angle indeed influences the results but not as dramatic as the other two factors. Unfortunately, a direct proof of the spatial resolution derived in Eq. (20) cannot be found in the literature to our best knowledge.

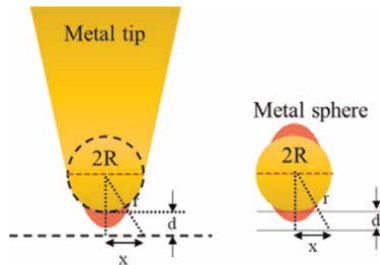


**Figure 9.** Sketch of the geometric structure and local field distribution of a metal tip and its approximation as a single sphere [153].

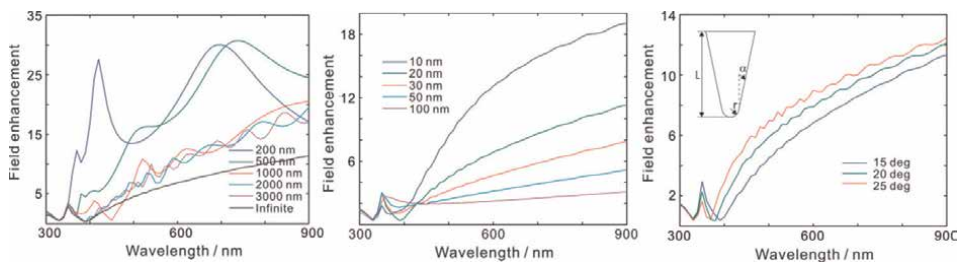


**Figure 10.** a) Local electric field enhancement spectra for conical tips with different tip lengths  $l$  with the tip radius  $r = 20$  nm and the tip cone angle  $\alpha = 15^\circ$ ; b) local electric field enhancement spectra at the tip apex for different tip radii, and the tip length is kept as infinite and tip angle =  $15^\circ$ ; c) local electric field enhancement spectra at the tip apex for different tip angles. The tip length is infinite and the tip radius  $r = 20$  nm. Inset indicates the simulated tip geometry [155].

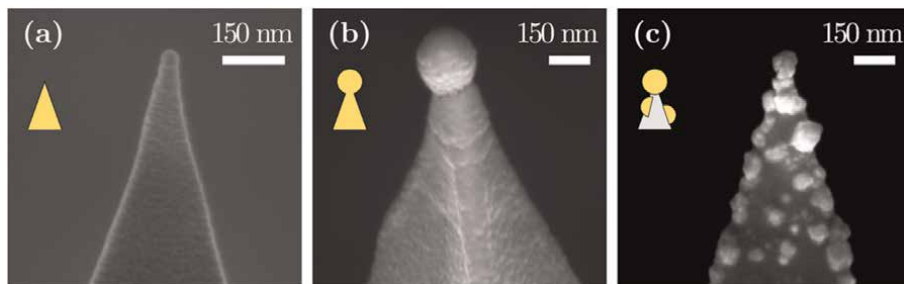
Due to the significance of the TERS tips, their fabrication became an important branch in the field of plasmonic [156, 157]. Different methods have been developed to produce metal TERS tips, such as electrochemical etching [158–160], electrodeposition [161, 162], and tip tailoring [163, 164]. Recently, Zhang developed an approach by concentrating the light *via* a waveguide and thus producing a low background hotspot at the tip apex [165].

Scanning electron microscope (SEM) images of commonly used tip geometries, namely of a) a sharp Au AFM tip, b) Au-coated spherical AFM tip and c) electrochemically deposited Au nanoparticle on a Pt AFM tip, are shown in **Figure 11** [166]. The related simulation work (shown in **Figure 12**) explained the experimental results.

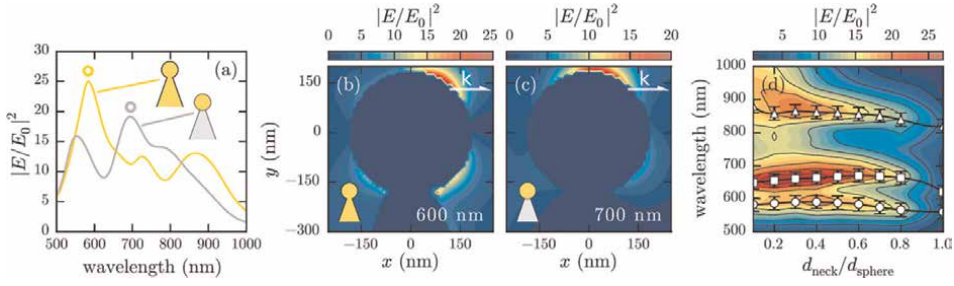
**Figures 11** and **12** show an example from tip fabrication to characterization and finally simulation. Here, the importance of the simulation is emphasized, and it not only helps to understand the optical response of the tip but can also help to design tips for specific resonance requirement. Thus, the simulation nowadays allows us from finding suitable experimental analytes to fulfilling instrument requirements and designing suitable experimental instruments for specific purposes.

## 2.5 Tip-substrate systems

Previously, it was demonstrated that a single metal tip alone can already enhance the electric field intensity in the vicinity of the tip apex due to its plasmonic resonance and the geometrical lightning rod effect. In a real TERS experiment, a metal substrate



**Figure 11.** SEM images of a) a sharp gold AFM tip; b) gold-coated spherical AFM tip, and c) electrochemically deposited gold nanoparticles on platinum AFM tip [166].


**Figure 12.**

a) Numerically simulated near-field spectra of spherical Au and AuNP-on-Pt tips with (b), (c) near-field maps of the main resonance as highlighted by circles in (a). Simulated tips have 300 nm spherical radii, 120 nm neck widths, 20° opening angles, and 1.88  $\mu\text{m}$  lengths to best match the typical experimental tip geometries and avoid truncation artifacts. Tips are illuminated by plane waves oriented along the tip axis. (d) Interpolated field enhancement map with superimposed resonant wavelengths, as the neck width varies from a spherical to a sharp tip. Tips have a 250 nm apex diameter, 1.88  $\mu\text{m}$  length, and 10° opening angle [166].

is usually present to further boost the signal. This type of configuration is called gap-mode TERS.

As shown in **Figure 13**, a gap-mode tip-substrate system can be considered as a dimer system composed of a metal sphere and its image dipole that is created in the metal film substrate [167]. Xu et al. gave a simple geometrical argument to estimate the local electric field in the gap of such dimer systems taking into consideration the drop in potential for the incident field  $E_{loc}$  [168].

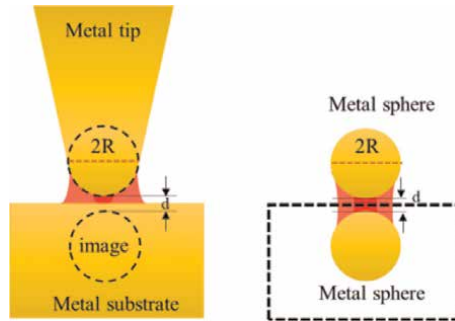
The drop in potential between the two spheres shown in **Figure 13** (dashed circles) can be expressed as  $\Delta V = |E_{loc}|d$ , while the potential difference between these two sites in the absence of two metal spheres can be expressed as [153]:

$$\Delta V = |E_{inc}|(2R + d) \quad (22)$$

Since the two spheres can be considered as equipotential bodies, we can write

$$\Delta V = |E_{inc}|(2R + d) = |E_{loc}|d \quad (23)$$

In a specific geometry, where the radius of the sphere  $R$  and distance right beneath the tip apex  $d$  are fixed, the lateral offset of electric field from the center can be written as


**Figure 13.**

Schematic presentation of metal tip-substrate structure and its approximation as a metal-sphere dimer [153].



$$|E_{loc}(x)| = \frac{\Delta V}{2R + d - 2\sqrt{R^2 - x^2}} \quad (24)$$

Therefore, the FWHM of the local field is given by  $FWHM_{E_{loc}} = 2\sqrt{Rd}$  [153]. Considering the TERS intensity, which is proportional to the fourth power of the local electric field [169], we get

$$|E_{loc}(x)|^4 = \frac{\Delta V^4}{(2R + d - 2\sqrt{R^2 - x^2})^4} \quad (25)$$

For a very small  $d$ , we can obtain the FWHM of the TERS intensity distribution as [170]:

$$FWHM_{TERS} = 2\sqrt{\left(\left(\sqrt[4]{2} - 1\right)Rd\right)} \approx 0.87\sqrt{Rd} \quad (26)$$

Many studies considered the easiest case of a substrate composed of a flat surface of a bulk material. The geometric parameters of the metal tip and the metal substrate with specific excitation wavelength using side illumination were evaluated numerically in ref. [169]. The study was performed using three-dimensional finite-difference time domain simulation (FDTD) and the effect of the presence of a substrate is demonstrated in **Figure 14**. Without a substrate, the electric field is enhanced by a factor  $M = 20$  (see **Figure 14**, left), while it reaches  $M = 189$  (see **Figure 14**, right) when there is a metal substrate.

Our own FEM simulation results on tip-substrate systems with various tip radii using the wave optics module in COMSOL 5.4 [93] are shown in **Figure 15**. To save the computational time, a two-dimensional model was built with a non-uniform mesh that guaranteed a very fine mesh grid element (less than 1 nm) in the region of the gap between the tip apex and the substrate [170].

To study the spectral dependence of each geometrical setting of various tip apex radii, a spectral sweep is performed from 500 nm to 800 nm. The results shown in

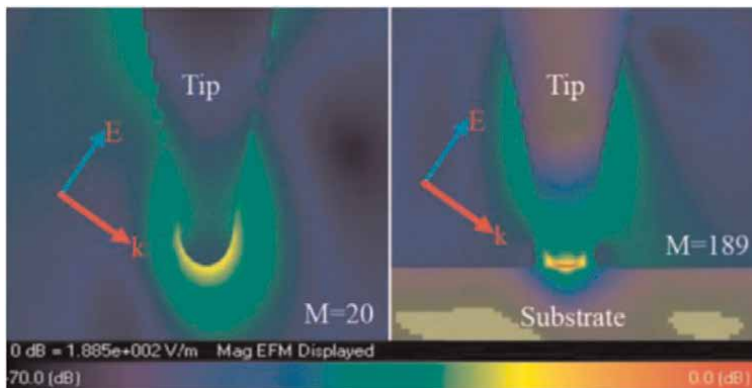


**Figure 14.** FDTD simulations of the electric field distribution for a single Au tip (a), and a gold tip held at distance  $d = 2$  nm from a gold substrate surface. The electric field  $E$  and wave vector  $k$  of the incoming light are displayed in the figures.  $M$  stands for the maximum enhancement [169].

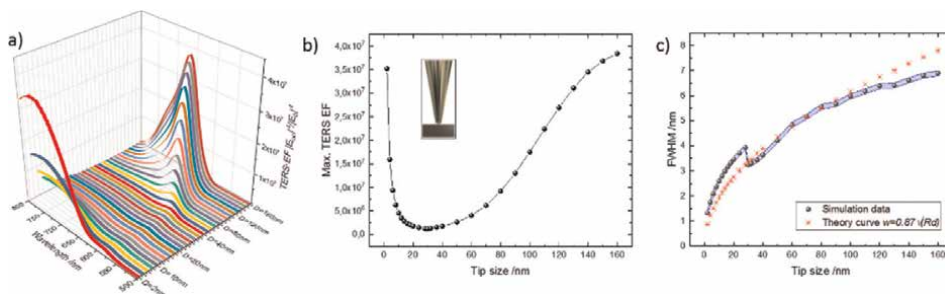


**Figure 15.** Simulation results of (a) the spectral dependence of the TERS EF as a function of tip diameter, (b) max. TERS EF, and (c) FWHM of the local TERS profile in the gap-mode TERS geometry as shown in the inset of **Figure 15b**. The simulated FWHM as a function of the tip diameter is compared with the FWHM profile derived from Eq. (26) (red asterisks in **Figure 15c**). The blue-shaded area presents the error bar of the FWHM [170].

**Figure 15** demonstrate a strong relation between the tip diameter and TERS enhancement factor with high spatial resolution, which is represented by the FWHM of the fourth power of the local field distribution beneath the tip apex. As the tip diameter increases from 30 nm to 160 nm, the increasing scattering cross section and the increasing radiative damping [171–173] both affect the enhancement factor, which increases and finally shows a saturation tendency.

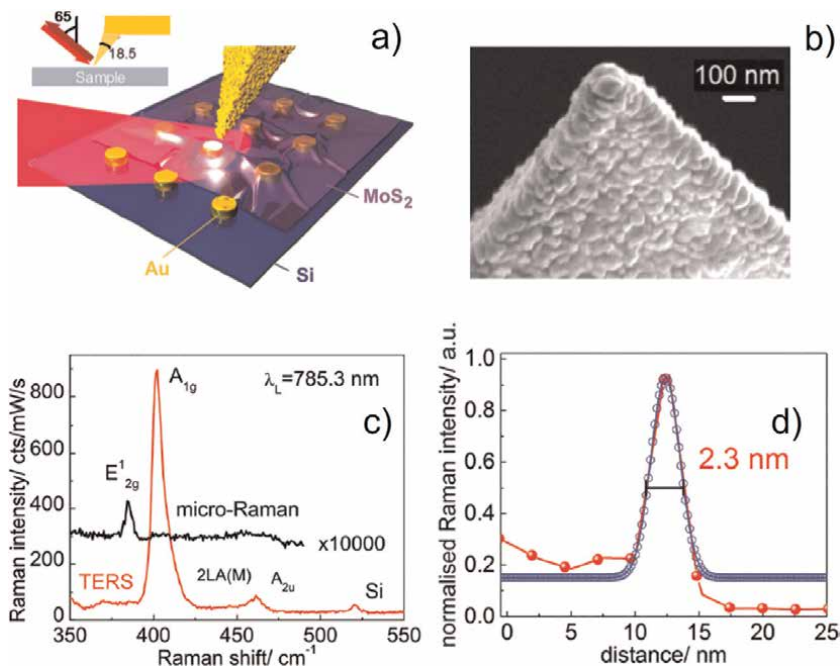


**Figure 16.** a) Scheme of the TERS experiment. b) A magnified SEM image of a TERS tip revealing the formation of Au nanoclusters at and around the tip. c) A representative TERS spectrum of a MoS<sub>2</sub> monolayer on an Au nanocluster array in comparison with the spectrum excited by 785.3 nm light; d) Gaussian fit of an intensity profile obtained for a scan across the rim of a nanodisk. The spatial resolution of the TERS image is equal to the full width at half maximum (FWHM) of the fit (2.3 nm). Reproduced from ref. [174] with permission from the Royal Society of Chemistry.

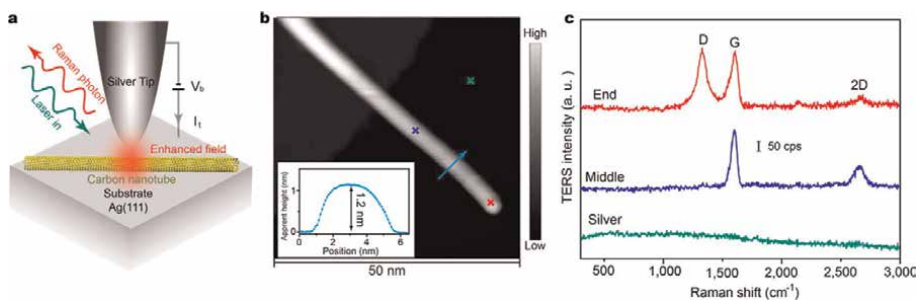


**Figure 17.** a) Schematic illustration of the STM-TERS experiments. b) STM topography of an isolated CNT on Ag (111) (1 V, 10 pA). Inset: Line profile of the CNT along the blue arrow line. c) Apparent height profile and TERS intensity profiles along the long end of a carbon nanotube [175].

Utilizing gap-mode TERS, Rahaman et al. performed TERS studies of MoS<sub>2</sub> layers on gold nanodisk arrays under the ambient conditions. They used a side illuminated AFM-TERS (**Figure 16a**) experimental configuration with a gold-coated Si AFM tip. The SEM image of the tip apex is shown in **Figure 16b**. The TERS enhancement factor was calculated using the A<sub>1g</sub> mode of MoS<sub>2</sub> and it reached  $5.6 \times 10^8$  (**Figure 16c**), while a spatial resolution of 2.3 nm was achieved (**Figure 16d**) [174].

STM-based TERS, on the other hand, can produce even better spatial resolution due to the sharpness of the STM tips and the controlled experimental environment. Liao used a STM-TERS system as sketched in **Figure 17a** on a carbon nanotube placed on an Ag (111) substrate. A STM topography image can be seen in **Figure 17b** [175]. They claimed a spatial resolution of 0.7 nm (**Figure 17c**) with a TERS EF of approximately  $10^8$ .

### 3. Conclusions

The geometry of plasmonic structures plays a key role and is an essential property of a plasmonic system. For SERS systems composed of metal nanoparticles without a supporting substrate or on a non-metal substrate, a single particle may not create significant enhancement, while their agglomeration demonstrates a much more enhanced signal both theoretically and experimentally. This is due to the existence of the hotspots that are created in small gap between the single elements. For a gap-mode SERS system, a good overall enhancement factor can be expected as the hotspots are created between the particle and the substrate, and/or between the plasmonic particles themselves. Finally, metal nanostructure arrays provide a versatile tool in the SERS catalog. Their optical resonance behavior can be tuned *via* changing their shapes using different approaches. For TERS systems, the lightning rod effect, which is induced by any geometric anisotropy, and the LSPR, which is influenced by the tip geometry and material, are the two most critical experimental and theoretical parameters, while the real experiment is usually performed in the so-called gap-mode TERS using metal substrates with metal tips. Despite the flexibility of the simulation tools addressing TERS experiments, the modeling of such experiments is still challenging due to the difficulties providing different and precise dimensions of active tips and

substrates. Nevertheless, the support of experimental results by the simulations or the planning of any SERS or TERS experiment using simulation tools is of major importance toward the understanding of the physics of plasmonic systems and in providing a better control over the measurement itself.

## **Acknowledgements**

This research was supported by the SMWK/ESF (RL ESF Hochschule und Forschung 2014-2020 mit Antragsnummer 100380093). We acknowledge financial support for the publication of this book by the State Digitization Program for Science and Culture of Saxony.

## **Conflict of interest**

The authors declare no conflict of interest.


## **Author details**

Lu He\*, Dietrich R.T. Zahn and Teresa I. Madeira  
Semiconductor Physics, Chemnitz University of Technology, Chemnitz, Germany

\*Address all correspondence to: [lu.he@physik.tu-chemnitz.de](mailto:lu.he@physik.tu-chemnitz.de)

## **IntechOpen**

---

© 2022 The Author(s). Licensee IntechOpen. This chapter is distributed under the terms of the Creative Commons Attribution License (<http://creativecommons.org/licenses/by/3.0>), which permits unrestricted use, distribution, and reproduction in any medium, provided the original work is properly cited. 

## References

- [1] Fleischmann M, Hendra PJ, McQuillan AJ. Raman spectra of pyridine adsorbed at a silver electrode. *Chemical Physics Letters*. 1974;**26**(2):163-166. DOI: 10.1016/0009-2614(74)85388-1
- [2] Albrecht MG, Creighton JA. Anomalous intense Raman spectra of pyridine at a silver electrode. *Journal of the American Chemical Society*. 1977;**99**(15): 5215-5217. DOI: 10.1021/ja00457a071
- [3] Jeanmaire DL, van Duyne RP. Surface Raman spectroelectrochemistry. *Journal of Electroanalytical Chemistry and Interfacial Electrochemistry*. 1977;**84**(1): 1-20. DOI: 10.1016/S0022-0728(77)80224-6
- [4] Wood TH, Zwemer DA, Shank CV, Rowe JE. The dependence of surface-enhanced Raman scattering on surface preparation: Evidence for an electromagnetic mechanism. *Chemical Physics Letters*. 1981;**82**(1):5-8. DOI: 10.1016/0009-2614(81)85095-6
- [5] Moskovits M. Surface roughness and the enhanced intensity of Raman scattering by molecules adsorbed on metals. *The Journal of Chemical Physics*. 1978;**69**(9): 4159-4161. DOI: 10.1063/1.437095
- [6] Creighton JA, Albrecht MG, Hester RE, Matthew J. The dependence of the intensity of Raman bands of pyridine at a silver electrode on the wavelength of excitation. *Chemical Physics Letters*. 1978;**55**(1):55-58. DOI: 10.1016/0009-2614(78)85131-8
- [7] Goad DGW, Moskovits M. Colloidal metal in aluminum-oxide. *Journal of Applied Physics*. 1978;**49**(5):2929-2934. DOI: 10.1063/1.325153
- [8] Phillip OLK. Optical properties of individual nano-sized gold particle pairs. In: *Mie-Scattering, Fluorescence, and Raman-Scattering*. Germany: TU Dresden
- [9] Kolwas K, Derkachova A. Impact of the Interband transitions in gold and silver on the dynamics of propagating and localized surface Plasmons. *Nanomaterials (Basel)*. 2020;**10**(7):1411. DOI: 10.3390/nano10071411
- [10] Shrivastav AM, Cvelbar U, Abdulhalim I. A comprehensive review on plasmonic-based biosensors used in viral diagnostics. *Communications Biology*. 2021;**4**(1):70. DOI: 10.1038/s42003-020-01615-8
- [11] Cortés E, Xie W, Cambiasso J, et al. Plasmonic hot electron transport drives nano-localized chemistry. *Nature Communications*. 2017;**8**:14880. DOI: 10.1038/ncomms14880
- [12] Flick J, Rivera N, Narang P. Strong light-matter coupling in quantum chemistry and quantum photonics. *Nano*. 2018;**7**(9):1479-1501. DOI: 10.1515/nanoph-2018-0067
- [13] Oksenberg E, Shlesinger I, Xomalis A, et al. Energy-resolved plasmonic chemistry in individual nanoreactors. *Nature Nanotechnology*. 2021;**16**(12):1378-1385. DOI: 10.1038/s41565-021-00973-6
- [14] Schürmann R, Nagel A, Juergensen S, et al. Microscopic understanding of reaction rates observed in Plasmon chemistry of nanoparticle-ligand systems. *The Journal of Physical Chemistry. C, Nanomaterials and Interfaces*. 2022;**126**(11):5333-5342. DOI: 10.1021/acs.jpcc.2c00278
- [15] Davis TJ, Gómez DE, Roberts A. Plasmonic circuits for manipulating

optical information. *Nano*. 2016;**6**(3): 543-559. DOI: 10.1515/nanoph-2016-0131

[16] Huang Y, Fang Y, Zhang Z, Zhu L, Sun M. Nanowire-supported plasmonic waveguide for remote excitation of surface-enhanced Raman scattering. *Light: Science & Applications*. 2014; **3**(8):e199-e199. DOI: 10.1038/lsa.2014.80

[17] Aalizadeh M, Khavasi A, Serebryannikov AE, Vandenbosch GAE, Ozbay E. A route to unusually broadband Plasmonic absorption spanning from visible to mid-infrared. *Plasmonics*. 2019;**14**(5):1269-1281. DOI: 10.1007/s11468-019-00916-x

[18] Tong J, Zhou W, Qu Y, Xu Z, Huang Z, Zhang DH. Surface plasmon induced direct detection of long wavelength photons. *Nature Communications*. 2017;**8**(1):1660. DOI: 10.1038/s41467-017-01828-2

[19] Liu A, Peng J, Li G. Characterizing penetration depths of multi-wavelength surface plasmon resonance sensor using silica beads. *Applied Physics Letters*. 2014;**104**(21):211103. DOI: 10.1063/1.4879830

[20] Ai B, Fan Z, Wong ZJ. Plasmonic-perovskite solar cells, light emitters, and sensors. *Microsystems & Nanoengineering*. 2022;**8**:5. DOI: 10.1038/s41378-021-00334-2

[21] Aubry A, Lei DY, Fernández-Domínguez AI, Sonnefraud Y, Maier SA, Pendry JB. Plasmonic light-harvesting devices over the whole visible spectrum. *Nano Letters*. 2010;**10**(7):2574-2579. DOI: 10.1021/nl101235d

[22] Mie G. Beiträge zur Optik trüber Medien, speziell kolloidaler Metallösungen. *Ann. Phys.* 1908;**330**(3):

377-445. DOI: 10.1002/andp.19083300302

[23] Gersten JI, Weitz DA, Gramila TJ, Genack AZ. Inelastic Mie scattering from rough metal surfaces: Theory and experiment. *Physical Review B*. 1980; **22**(10):4562-4571. DOI: 10.1103/PhysRevB.22.4562

[24] Gersten JI. Rayleigh, Mie, and Raman scattering by molecules adsorbed on rough surfaces. *The Journal of Chemical Physics*. 1980;**72**(10): 5780-5781. DOI: 10.1063/1.439003

[25] Tiggesbäumker K, Meiwes-Broer L. Blue shift of the Mie plasma frequency in Ag clusters and particles. *Physical Review A*. 1993;**48**(3):R1749-R1752. DOI: 10.1103/physreva.48.r1749

[26] Papoff F, Hourahine B. Geometrical Mie theory for resonances in nanoparticles of any shape. *Optics Express*. 2011;**19**(22):21432-21444. DOI: 10.1364/OE.19.021432

[27] You C, Nellikka AC, de Leon I, Magaña-Loaiza OS. Multiparticle quantum plasmonics. *Nano*. 2020;**9**(6): 1243-1269. DOI: 10.1515/nanoph-2019-0517

[28] Jamshidi Z, Asadi-Aghbolaghi N, Morad R, et al. Comparing the nature of quantum plasmonic excitations for closely spaced silver and gold dimers. *The Journal of Chemical Physics*. 2022;**156**(7):74102. DOI: 10.1063/5.0079258

[29] Xiang H, Zu J, Jiang H, Xu L, Lu G, Zhang X. Understanding quantum Plasmonic enhancement in Nanorod dimers from time-dependent orbital-free density functional theory. *Journal of Physical Chemistry C*. 2022;**126**(10): 5046-5054. DOI: 10.1021/acs.jpcc.2c00105

- [30] Maier SA. *Plasmonics: Fundamentals and Applications*. New York: Springer; 2007
- [31] Esteban R, Borisov AG, Nordlander P, Aizpurua J. Bridging quantum and classical plasmonics with a quantum-corrected model. *Nature Communications*. 2012;**3**:825. DOI: 10.1038/ncomms1806
- [32] Tame MS, McEneaney KR, Özdemir ŞK, Lee J, Maier SA, Kim MS. Quantum plasmonics. *Nature Physics*. 2013;**9**(6): 329-340. DOI: 10.1038/nphys2615
- [33] Varas A, García-González P, Feist J, García-Vidal FJ, Rubio A. Quantum plasmonics: From jellium models to ab initio calculations. *Nano*. 2016;**5**(3): 409-426. DOI: 10.1515/nanoph-2015-0141
- [34] Zhu W, Esteban R, Borisov AG, et al. Quantum mechanical effects in plasmonic structures with subnanometre gaps. *Nature Communications*. 2016;**7**: 11495. DOI: 10.1038/ncomms11495
- [35] Da X, Xiong X, Wu L, et al. Quantum plasmonics: New opportunity in fundamental and applied photonics. *Advances in Optics and Photonics*. 2018;**10**(4):703. DOI: 10.1364/AOP.10.000703
- [36] Fiederling K, Abasifard M, Richter M, Deckert V, Gräfe S, Kupfer S. The chemical effect goes resonant - a full quantum mechanical approach on TERS. *Nanoscale*. 2020;**12**(11):6346-6359. DOI: 10.1039/c9nr09814c
- [37] Lovász B, Sándor P, Kiss G-Z, et al. Nonadiabatic Nano-optical tunneling of photoelectrons in Plasmonic Near-fields. *Nano Letters*. 2022;**22**(6):2303-2308. DOI: 10.1021/acs.nanolett.1c04651
- [38] Bohren CF, Huffman DR. *Absorption and Scattering of Light by Small Particles*. New York, Chichester: Wiley; 1993 (1998[printing])
- [39] Jensen T, Kelly L, Lazarides A, Schatz GC. Electrodynamics of Noble metal nanoparticles and nanoparticle clusters. *Journal of Cluster Science*. 1999;**10**(2):295-317. DOI: 10.1023/A:1021977613319
- [40] Fan X, Zheng W, Singh DJ. Light scattering and surface plasmons on small spherical particles. *Light: Science & Applications*. 2014;**3**(6):e179-e179. DOI: 10.1038/lsa.2014.60
- [41] Coronado EA, Schatz GC. Surface plasmon broadening for arbitrary shape nanoparticles: A geometrical probability approach. *The Journal of Chemical Physics*. 2003;**119**(7):3926-3934. DOI: 10.1063/1.1587686
- [42] Kelly KL, Coronado E, Zhao LL, Schatz GC. The optical properties of metal nanoparticles: The influence of size, shape, and dielectric environment. *The Journal of Physical Chemistry. B*. 2003;**107**(3):668-677. DOI: 10.1021/jp026731y
- [43] Diaz HRR, Esquivel-Sirvent R, Noguez C. Plasmonic response of nested nanoparticles with arbitrary geometry. *Journal of Physical Chemistry C*. 2016;**120**(4):2349-2354. DOI: 10.1021/acs.jpcc.5b10109
- [44] Schnitzer O, Giannini V, Maier SA, Craster RV. Surface plasmon resonances of arbitrarily shaped nanometallic structures in the small-screening-length limit. *Proceedings. Mathematical, Physical, and Engineering Sciences*. 2016;**472**(2191):20160258. DOI: 10.1098/rspa.2016.0258
- [45] Kamandar Dezfouli M, Tserkezis C, Mortensen NA, Hughes S. Nonlocal quasinormal modes for arbitrarily

shaped three-dimensional plasmonic resonators. *Optica*. 2017;**4**(12):1503. DOI: 10.1364/OPTICA.4.001503

[46] Santiago EY, Besteiro LV, Kong X-T, Correa-Duarte MA, Wang Z, Govorov AO. Efficiency of hot-electron generation in Plasmonic nanocrystals with complex shapes: Surface-induced scattering, hot spots, and Interband transitions. *ACS Photonics*. 2020;**7**(10): 2807-2824. DOI: 10.1021/acsp Photonics.0c01065

[47] Chung HY, Guo GY, Chiang H-P, Tsai DP, Leung PT. Accurate description of the optical response of a multilayered spherical system in the long wavelength approximation. *Physical Review B*. 2010; **82**(16):165440. DOI: 10.1103/PhysRevB.82.165440

[48] Rasskazov IL, Zakomirnyi VI, Utyushev AD, Carney PS, Moroz A. Remarkable predictive power of the modified long wavelength approximation. *Journal of Physical Chemistry C*. 2021;**125**(3):1963-1971. DOI: 10.1021/acs.jpcc.0c09774

[49] Chung HY, Leung PT, Tsai DP. Modified long wavelength approximation for the optical response of a graded-index Plasmonic nanoparticle. *Plasmonics*. 2012;**7**(1): 13-18. DOI: 10.1007/s11468-011-9269-5

[50] Fornasiero D, Grieser F. Analysis of the visible absorption and SERS excitation spectra of silver sols. *The Journal of Chemical Physics*. 1987;**87**(5): 3213-3217. DOI: 10.1063/1.453009

[51] Kolwas K, Derkachova A. Plasmonic abilities of gold and silver spherical nanoantennas in terms of size dependent multipolar resonance frequencies and plasmon damping rates. *Opto-Electronics Review*. 2010;**18**(4):429-437. DOI: 10.2478/s11772-010-0043-6

[52] Lee Y-J, Schade NB, Sun L, et al. Ultrasoft, highly spherical monocrystalline gold particles for precision plasmonics. *ACS Nano*. 2013;**7**(12): 11064-11070. DOI: 10.1021/nn404765w

[53] Link S, El-Sayed MA. Spectral properties and relaxation dynamics of surface Plasmon electronic oscillations in gold and silver Nanodots and Nanorods. *The Journal of Physical Chemistry. B*. 1999;**103**(40):8410-8426. DOI: 10.1021/jp9917648

[54] Lermé J. Size evolution of the surface Plasmon resonance damping in silver nanoparticles: Confinement and dielectric effects. *Journal of Physical Chemistry C*. 2011;**115**(29):14098-14110. DOI: 10.1021/jp203481m

[55] Charlé K-P, König L, Nepijko S, Rabin I, Schulze W. The surface Plasmon resonance of free and embedded Ag-clusters in the size range  $1,5 \text{ nm} < D < 30 \text{ nm}$ . *Crystal Research and Technology*. 1998;**33**(7-8):1085-1096. DOI: 10.1002/(SICI)1521-4079(199810)33:7/8 <1085::AID-CRAT1085>3.0.CO; 2-A

[56] Kreibig U, Vollmer M. Theoretical considerations. In: Toennies JP, Gonsler U, Osgood RM, et al., editors. *Optical Properties of Metal Clusters*. Berlin, Heidelberg: Springer Berlin Heidelberg; 1995. pp. 13-201

[57] Dhara AK, Ghosh SK. Density-functional theory for time-dependent systems. *Physical Review A*. 1987;**35**:442

[58] Yabana B. Time-dependent local-density approximation in real time. *Physical Review B: Condensed Matter*. 1996;**54**(7):4484-4487. DOI: 10.1103/physrevb.54.4484

[59] Sholl DS, Steckel JA. In: Sholl JA, Steckel., editors. *Density Functional*



Theory: A Practical Introduction/  
David S. Hoboken, N.J.: Wiley; 2009

[60] Prodan E, Radloff C, Halas NJ, Nordlander P. A hybridization model for the plasmon response of complex nanostructures. *Science*. 2003; **302**(5644):419-422. DOI: 10.1126/science.1089171

[61] Nordlander P, Oubre C, Prodan E, Li K, Stockman MI. Plasmon hybridization in nanoparticle dimers. *Nano Letters*. 2004; **4**(5):899-903. DOI: 10.1021/nl049681c

[62] Prodan E, Nordlander P. Structural Tunability of the Plasmon resonances in metallic Nanoshells. *Nano Letters*. 2003; **3**(4):543-547. DOI: 10.1021/nl034030m

[63] Oubre C, Nordlander PJ. Finite difference time-domain studies of optical properties of nanoshell structures. In: *Proceedings SPIE 5221. Plasmonics: Metallic Nanostructures and Their Optical Properties*. 2003. DOI: 10.1117/12.511664. [28 October 2003]

[64] Mohsin ASM, Salim MB. Probing the Plasmon coupling, quantum yield, and effects of tip geometry of gold nanoparticle using analytical models and FDTD simulation. *IEEE Photonics Journal*. 2018; **10**(3):1-10. DOI: 10.1109/JPHOT.2018.2825435

[65] Benz F, Nijs B de, Tserkezis C, et al. Generalized circuit model for coupled plasmonic systems. *Optics Express* 2015; **23**(26):33255-33269 [DOI: 10.1364/OE.23.033255]

[66] Jeong H-H, Adams MC, Günther J-P, et al. Arrays of Plasmonic nanoparticle dimers with defined Nanogap spacers. *ACS Nano*. 2019; **13**(10):11453-11459. DOI: 10.1021/acsnano.9b04938

[67] Arbuz A, Sultangaziyev A, Rapikov A, Kunushpayeva Z, Bukasov R. How gap distance between gold nanoparticles in dimers and trimers on metallic and non-metallic SERS substrates can impact signal enhancement. *Nanoscale Advances*. 2021; **4**(1):268-280. DOI: 10.1039/D1NA00114K

[68] Jain PK, Huang W, El-Sayed MA. On the universal scaling behavior of the distance decay of Plasmon coupling in metal nanoparticle pairs: A Plasmon ruler equation. *Nano Letters*. 2007; **7**(7):2080-2088. DOI: 10.1021/nl071008a

[69] Aćimović SS, Kreuzer MP, González MU, Quidant R. Plasmon near-field coupling in metal dimers as a step toward single-molecule sensing. *ACS Nano*. 2009; **3**(5):1231-1237. DOI: 10.1021/nn900102j

[70] Funston AM, Novo C, Davis TJ, Mulvaney P. Plasmon coupling of gold nanorods at short distances and in different geometries. *Nano Letters*. 2009; **9**(4):1651-1658. DOI: 10.1021/nl900034v

[71] Masango SS, Hackler RA, Large N, et al. High-resolution distance dependence study of surface-enhanced Raman scattering enabled by atomic layer deposition. *Nano Letters*. 2016; **16**(7):4251-4259. DOI: 10.1021/acs.nanolett.6b01276

[72] Song J-H, Raza S, van de Groep J, et al. Nanoelectromechanical modulation of a strongly-coupled plasmonic dimer. *Nature Communications*. 2021; **12**(1):48. DOI: 10.1038/s41467-020-20273-2

[73] Wang X, Huang S-C, Hu S, Yan S, Ren B. Fundamental understanding and applications of plasmon-enhanced Raman spectroscopy. *Nature Reviews Physics*. 2020; **2**(5):253-271. DOI: 10.1038/s42254-020-0171-y

- [74] Kudelski A, Wojtysiak S. Silica-covered silver and gold Nanoresonators for Raman analysis of surfaces of various materials. *Journal of Physical Chemistry C*. 2012;**116**(30):16167-16174. DOI: 10.1021/jp304409x
- [75] Sivanesan A, Kozuch J, Ly HK, Kalaivani G, Fischer A, Weidinger IM. Tailored silica coated Ag nanoparticles for non-invasive surface enhanced Raman spectroscopy of biomolecular targets. *RSC Advances*. 2012;**2**(3): 805-808. DOI: 10.1039/C1RA00781E
- [76] Kołataj K, Krajczewski J, Kudelski A. Silver nanoparticles with many sharp apexes and edges as efficient Nanoresonators for Shell-isolated nanoparticle-enhanced Raman spectroscopy. *Journal of Physical Chemistry C*. 2017;**121**(22):12383-12391. DOI: 10.1021/acs.jpcc.7b02695
- [77] Barbillon G. Applications of Shell-isolated nanoparticle-enhanced Raman spectroscopy. *Photonics*. 2021;**8**(2):46. DOI: 10.3390/photonics8020046
- [78] Avakyan LA, Heinz M, Skidanenko AV, et al. Insight on agglomerates of gold nanoparticles in glass based on surface plasmon resonance spectrum: Study by multi-spheres T-matrix method. *Journal of Physics. Condensed Matter*. 2018;**30**(4): 45901. DOI: 10.1088/1361-648X/aa9fcc
- [79] Pawlak M, Bagiński M, Llombart P, et al. Tuneable helices of plasmonic nanoparticles using liquid crystal templates: Molecular dynamics investigation of an unusual odd-even effect in liquid crystalline dimers. *Chemical Communications (Camb)*. 2022;**58**(53):7364-7367. DOI: 10.1039/d2cc00560c
- [80] Nečada M, Törmä P. Multiple-scattering T-matrix simulations for nanophotonics: Symmetries and periodic lattices. *CiCP*. 2021;**30**(2):357-395. DOI: 10.4208/cicp.OA-2020-0136
- [81] Khlebtsov NG. T-matrix method in plasmonics: An overview. *Journal of Quantitative Spectroscopy and Radiative Transfer*. 2013;**123**:184-217. DOI: 10.1016/j.jqsrt.2012.12.027
- [82] Demchuk A, Bolesta I, Kushnir O, Kolych I. The computational studies of Plasmon interaction. *Nanoscale Research Letters*. 2017;**12**(1):273. DOI: 10.1186/s11671-017-2050-8
- [83] Yurkin MA, Hoekstra AG. The discrete dipole approximation: An overview and recent developments. *Journal of Quantitative Spectroscopy and Radiative Transfer*. 2007;**106**(1-3): 558-589. DOI: 10.1016/j.jqsrt.2007.01.034
- [84] Burger S, Zschiedrich L, Pomplun J, Schmidt F. Finite element method for accurate 3D simulation of plasmonic waveguides, *SPIE OPTO*, 2010, San Francisco, California, United States. 2010;**7604**:76040F. [DOI:10.1117/12.841995]
- [85] Downes A, Salter D, Elfick A. Simulations of tip-enhanced optical microscopy reveal atomic resolution. *Journal of Microscopy*. 2008;**229**(Pt 2): 184-188. DOI: 10.1111/j.1365-2818.2008.01884.x
- [86] Remcom. FDTD Method for Electromagnetic Simulation — Remcom. 2022. Available from: <https://www.remcom.com/electromagnetic-simulation-numerical-methods/fdtd-method-simulation-software> [Accessed: August 11, 2022]
- [87] Smajic J, Hafner C, Raguin L, Tavzarashvili K, Mishrikey M. Comparison of numerical methods for

the analysis of Plasmonic structures. *Journal of Computational and Theoretical Nanoscience*. 2009; **6**(3):763-774. DOI: 10.1166/jctn.2009.1107

[88] Liu Y-C, Chang K, Fwu J, Shih L. Performance comparison between FDTD and FEM for the simulation of plasmonic waveguide operating at optical communication frequency. 2013 USNC-URSI Radio Science Meeting (Joint with AP-S Symposium). 2013. pp. 184-184, DOI: 10.1109/USNC-URSI.2013.6715490

[89] Parsons J, Burrows CP, Sambles JR, Barnes WL. A comparison of techniques used to simulate the scattering of electromagnetic radiation by metallic nanostructures. *Journal of Modern Optics*. 2010;**57**(5):356-365. DOI: 10.1080/09500341003628702

[90] Rapp BE, editor. Chapter 32—Finite Element Method[J]. *Microfluidics: Modelling, Mechanics and Mathematics; Micro and Nano Technologies*. 2017:655-678

[91] Lesina AC, Vaccari A, Berini P, Ramunno L. On the convergence and accuracy of the FDTD method for nanoplasmonics. *Optics Express*. 2015; **23**(8):10481-10497. DOI: 10.1364/OE.23.010481

[92] Gonçalves MR. Plasmonic nanoparticles: Fabrication, simulation and experiments. *Journal of Physics D: Applied Physics*. 2014;**47**(21):213001. DOI: 10.1088/0022-3727/47/21/213001

[93] COMSOL Multiphysics. Available from: <https://www.comsol.com/>

[94] Wave Optics Module User's Guide, COMSOL Multiphysics® v. 5.6. COMSOL AB, Stockholm, Sweden. 2021

[95] Zhang Y, Walkenfort B, Yoon JH, Schlücker S, Xie W. Gold and silver nanoparticle monomers are non-SERS-active: A negative experimental study with silica-encapsulated Raman-reporter-coated metal colloids. *Physical Chemistry Chemical Physics*. 2015; **17**(33):21120-21126. DOI: 10.1039/c4cp05073h

[96] Majić MRA, Auguie B, Le Ru EC. Comparison of dynamic corrections to the quasistatic polarizability and optical properties of small spheroidal particles. *The Journal of Chemical Physics*. 2022; **156**(10):104110. DOI: 10.1063/5.0085687

[97] Majic M, Pratley L, Schebarchov D, Somerville WRC, Auguie B, Le Ru EC. Approximate T matrix and optical properties of spheroidal particles to third order with respect to size parameter. *Physical Review A*. 2019;**99**(1):013853. DOI: 10.1103/PhysRevA.99.013853

[98] Takeuchi T, Noda M, Yabana K. Operation of quantum Plasmonic Metasurfaces using electron transport through subnanometer gaps. *ACS Photonics*. 2019;**6**(10):2517-2522. DOI: 10.1021/acsp Photonics.9b00889

[99] Zuloaga J, Prodan E, Nordlander P. Quantum description of the plasmon resonances of a nanoparticle dimer. *Nano Letters*. 2009;**9**(2):887-891. DOI: 10.1021/nl803811g

[100] Barbry M, Koval P, Marchesin F, et al. Atomistic near-field nanoplasmonics: Reaching atomic-scale resolution in nanooptics. *Nano Letters*. 2015;**15**(5):3410-3419. DOI: 10.1021/acs.nanolett.5b00759

[101] Mao L, Li Z, Wu B, Xu H. Effects of quantum tunneling in metal nanogap on surface-enhanced Raman scattering. *Applied Physics Letters*. 2009;**94**(24):243102. DOI: 10.1063/1.3155157

- [102] Savage KJ, Hawkeye MM, Esteban R, Borisov AG, Aizpurua J, Baumberg JJ. Revealing the quantum regime in tunnelling plasmonics. *Nature*. 2012;**491**(7425):574-577. DOI: 10.1038/nature11653
- [103] Scholl JA, García-Etxarri A, Koh AL, Dionne JA. Observation of quantum tunneling between two plasmonic nanoparticles. *Nano Letters*. 2013;**13**(2): 564-569. DOI: 10.1021/nl304078v
- [104] Scholl JA, Garcia-Etxarri A, Aguirregabiria G, et al. Evolution of Plasmonic Metamolecule modes in the quantum tunneling regime. *ACS Nano*. 2016;**10**(1):1346-1354. DOI: 10.1021/acsnano.5b06738
- [105] Liu Z, Zhang F, Yang Z, et al. Gold mesoparticles with precisely controlled surface topographies for single-particle surface-enhanced Raman spectroscopy. *Journal of Materials Chemistry C*. 2013; **1**(35):5567. DOI: 10.1039/c3tc30824c
- [106] Minati L, Benetti F, Chiappini A, Speranza G. One-step synthesis of star-shaped gold nanoparticles. *Colloids and Surfaces A: Physicochemical and Engineering Aspects*. 2014;**441**:623-628. DOI: 10.1016/j.colsurfa.2013.10.025
- [107] Giannini V, Rodríguez-Oliveros R, Sánchez-Gil JA. Surface Plasmon resonances of metallic Nanostars/ Nanoflowers for surface-enhanced Raman scattering. *Plasmonics*. 2010; **5**(1):99-104. DOI: 10.1007/s11468-009-9121-3
- [108] Mazzucco S, Stéphan O, Colliex C, et al. Spatially resolved measurements of plasmonic eigenstates in complex-shaped, asymmetric nanoparticles: Gold nanostars. *European Physical Journal Applied Physics*. 2011;**54**(3):33512. DOI: 10.1051/epjap/2011100443
- [109] Garcia-Leis A, Torreggiani A, Garcia-Ramos JV, Sanchez-Cortes S. Hollow Au/Ag nanostars displaying broad plasmonic resonance and high surface-enhanced Raman sensitivity. *Nanoscale*. 2015;**7**(32):13629-13637. DOI: 10.1039/c5nr02819a
- [110] He S, Kang MWC, Khan FJ, Tan EKM, Reyes MA, Kah JCY. Optimizing gold nanostars as a colloid-based surface-enhanced Raman scattering (SERS) substrate. *Journal of Optics*. 2015;**17**(11):114013. DOI: 10.1088/2040-8978/17/11/114013
- [111] Kariuki VM, Hoffmeier JC, Yazgan I, Sadik OA. Seedless synthesis and SERS characterization of multi-branched gold nanoflowers using water soluble polymers. *Nanoscale*. 2017;**9**(24): 8330-8340. DOI: 10.1039/c7nr01233k
- [112] Tran V, Thiel C, Svejda JT, et al. Probing the SERS brightness of individual Au nanoparticles, hollow Au/Ag nanoshells, Au nanostars and Au core/Au satellite particles: Single-particle experiments and computer simulations. *Nanoscale*. 2018;**10**(46):21721-21731. DOI: 10.1039/c8nr06028b
- [113] Choo P, Arenas-Esteban D, Jung I, et al. Investigating reaction intermediates during the seedless growth of gold Nanostars using electron tomography. *ACS Nano*. 2022;**16**(3):4408-4414. DOI: 10.1021/acsnano.1c10669
- [114] Ahmed W, Demirtaş Ö, Öztürk İM, Bek A. Monolayer assembly of MultiSpiked gold nanoparticles for surface-enhanced Raman spectroscopy-based trace detection of dyes and explosives. *ACS Applied Nano Materials*. 2020;**3**(7):6766-6773. DOI: 10.1021/acsanm.0c01177
- [115] Gellner M, Steinigeweg D, Ichilmann S, et al. 3D self-assembled

plasmonic superstructures of gold nanospheres: Synthesis and characterization at the single-particle level. *Small*. 2011;7(24):3445-3451. DOI: 10.1002/smll.201102009

[116] Yang J-K, Kang H, Lee H, et al. Single-step and rapid growth of silver nanoshells as SERS-active nanostructures for label-free detection of pesticides. *ACS Applied Materials & Interfaces*. 2014;6(15):12541-12549. DOI: 10.1021/am502435x

[117] McLellan JM, Li Z-Y, Siekkinen AR, Xia Y. The SERS activity of a supported Ag nanocube strongly depends on its orientation relative to laser polarization. *Nano Letters*. 2007;7(4):1013-1017. DOI: 10.1021/nl070157q

[118] Near R, Hayden S, El-Sayed M. Extinction vs absorption: Which is the indicator of Plasmonic field strength for silver Nanocubes? *Journal of Physical Chemistry C*. 2012;116(43):23019-23026. DOI: 10.1021/jp309272b

[119] Rycenga M, Langille MR, Personick ML, Ozel T, Mirkin CA. Chemically isolating hot spots on concave nanocubes. *Nano Letters*. 2012;12(12):6218-6222. DOI: 10.1021/nl3032235

[120] Jeon HB, Tsalu PV, Ha JW. Shape effect on the refractive index sensitivity at localized surface Plasmon resonance inflection points of single gold Nanocubes with vertices. *Scientific Reports*. 2019;9(1):13635. DOI: 10.1038/s41598-019-50032-3

[121] Xu P, Lu W, Zhang J, Zhang L. Efficient hydrolysis of ammonia borane for hydrogen evolution catalyzed by Plasmonic Ag@Pd Core-Shell Nanocubes. *ACS Sustainable Chemistry & Engineering*. 2020;8(33):12366-12377. DOI: 10.1021/acssuschemeng.0c02276

[122] Dong J, Yang C, Wu H, et al. Two-dimensional self-assembly of Au@Ag Core-Shell Nanocubes with different permutations for ultrasensitive SERS measurements. *ACS Omega*. 2022;7(4):3312-3323. DOI: 10.1021/acsomega.1c05452

[123] Kneipp K, Haka AS, Kneipp H, et al. Surface-enhanced Raman spectroscopy in single living cells using gold nanoparticles. *Applied Spectroscopy*. 2002;56(2):150-154. DOI: 10.1366/0003702021954557

[124] Wustholz KL, Henry A-I, McMahon JM, et al. Structure-activity relationships in gold nanoparticle dimers and trimers for surface-enhanced Raman spectroscopy. *Journal of the American Chemical Society*. 2010;132(31):10903-10910. DOI: 10.1021/ja104174m

[125] Gao Y, Zhang R, Cheng J-C, Liaw J-W, Ma C. Optical properties of plasmonic dimer, trimer, tetramer and pentamer assemblies of gold nanoboxes. *Journal of Quantitative Spectroscopy and Radiative Transfer*. 2013;125:23-32. DOI: 10.1016/j.jqsrt.2013.04.014

[126] Zohar N, Chuntonov L, Haran G. The simplest plasmonic molecules: Metal nanoparticle dimers and trimers. *Journal of Photochemistry and Photobiology C: Photochemistry Reviews*. 2014;21:26-39. DOI: 10.1016/j.jphotochemrev.2014.10.002

[127] Sergiienko S, Moor K, Gudun K, Yelemessova Z, Bukasov R. Nanoparticle-nanoparticle vs. nanoparticle-substrate hot spot contributions to the SERS signal: Studying Raman labelled monomers, dimers and trimers. *Physical Chemistry Chemical Physics*. 2017;19(6):4478-4487. DOI: 10.1039/c6cp08254h

[128] Nagarajan A, Panchanathan AP, Chelliah P, Satoh H, Inokawa H. FDTD

study on evolution of trimer silver@silica Nanospheres to dimer for SERS characteristics. *Plasmonics*. 2022; **17**(2):647-652. DOI: 10.1007/s11468-021-01554-y

[129] VAF. 2013 7th International Congress on Advanced Electromagnetic Materials in Microwaves and Optics (METAMATERIALS 2013): Bordeaux, France, 16–21 September 2013. Piscataway, NJ: IEEE; 2013

[130] Jin Q, Wang L, Yan S, Wei H, Huang Y. Plasmonic nano-tweezer based on square nanoplate tetramers. *Applied Optics*. 2018;**57**(19):5328-5332. DOI: 10.1364/AO.57.005328

[131] Xi C, Marina PF, Xia H, Wang D. Directed self-assembly of gold nanoparticles into plasmonic chains. *Soft Matter*. 2015;**11**(23):4562-4571. DOI: 10.1039/c5sm00900f

[132] Pocock SR, Xiao X, Huidobro PA, Giannini V. Topological Plasmonic chain with retardation and radiative effects. *ACS Photonics*. 2018;**5**(6):2271-2279. DOI: 10.1021/acsp Photonics.8b00117

[133] Luo S, Mancini A, Wang F, Liu J, Maier SA, de Mello JC. High-throughput fabrication of triangular Nanogap arrays for surface-enhanced Raman spectroscopy. *ACS Nano*. 2022;**16**:7438-7447. DOI: 10.1021/acsnano.1c09930

[134] Zhang C, Chen S, Jiang Z, Shi Z, Wang J, Du L. Highly sensitive and reproducible SERS substrates based on ordered microp pyramid Array and silver nanoparticles. *ACS Applied Materials & Interfaces*. 2021;**13**(24):29222-29229. DOI: 10.1021/acsam.1c08712

[135] Lu Y-C, Chiang W-H, Liu C-Y, Chu JP, Ho H-C, Hsueh C-H. Wafer-scale SERS metallic nanotube arrays with

highly ordered periodicity. *Sensors and Actuators B: Chemical*. 2021;**329**:129132. DOI: 10.1016/j.snb.2020.129132

[136] Kim J, Lee JS, Kim J-W, et al. Fabrication of plasmonic arrays of nanodisks and nanotriangles by nanotip indentation lithography and their optical properties. *Nanoscale*. 2021; **13**(8):4475-4484. DOI: 10.1039/d0nr08398d

[137] Choi M, Kim S, Choi SH, Park H-H, Byun KM. Highly reliable SERS substrate based on plasmonic hybrid coupling between gold nanoislands and periodic nanopillar arrays. *Optics Express*. 2020; **28**(3):3598-3606. DOI: 10.1364/OE.386726

[138] Kasani S, Curtin K, Wu N. A review of 2D and 3D plasmonic nanostructure array patterns: Fabrication, light management and sensing applications. *Nano*. 2019;**8**(12):2065-2089. DOI: 10.1515/nanoph-2019-0158

[139] Anikin K, Rodyakina E, Veber S, Milekhin A, Latyshev A, Zahn DRT. Localized surface Plasmon resonance in gold nanocluster arrays on opaque substrates. *Plasmonics*. 2019;**14**(6):1527-1537. DOI: 10.1007/s11468-019-00949-2

[140] Brawley ZT, Bauman SJ, Darweesh AA, Debu DT, Tork Ladani F, Herzog JB. Plasmonic Au Array SERS substrate with optimized thin film oxide substrate layer. *Materials (Basel)*. 2018; **11**(6):942. DOI: 10.3390/ma11060942

[141] Zhao Q, Yang H, Nie B, Luo Y, Shao J, Li G. Wafer-scale and cost-effective manufacturing of controllable Nanogap arrays for highly sensitive SERS sensing. *ACS Applied Materials & Interfaces*. 2022;**14**(2):3580-3590. DOI: 10.1021/acsam.1c22465

- [142] Hu Y, Li L, Wang R, et al. High-speed parallel Plasmonic direct-writing nanolithography using Metasurface-based Plasmonic lens. *Engineering*. 2021; **7(11)**:1623-1630. DOI: 10.1016/j.eng.2020.08.019
- [143] Hulteen JC, van Duyne RP. Nanosphere lithography: A materials general fabrication process for periodic particle array surfaces. *Journal of Vacuum Science & Technology A: Vacuum, Surfaces, and Films*. 1995; **13(3)**:1553-1558. DOI: 10.1116/1.579726
- [144] Haynes CL, van Duyne RP. Nanosphere lithography: A versatile nanofabrication tool for studies of size-dependent nanoparticle optics. *The Journal of Physical Chemistry. B*. 2001; **105(24)**:5599-5611. DOI: 10.1021/jp010657m
- [145] Zhang C. *Nanosphere Lithography and its Application in Rapid and Economic Fabrication of Plasmonic Hydrogenated Amorphous Silicon Photovoltaic Devices*. MI, USA: Michigan Technological University; 2016
- [146] Rahaman M, Moras S, He L, Madeira TI, Zahn DRT. Fine-tuning of localized surface plasmon resonance of metal nanostructures from near-infrared to blue prepared by nanosphere lithography. *Journal of Applied Physics*. 2020; **128(23)**:233104. DOI: 10.1063/5.0027139
- [147] Kahraman M, Daggumati P, Kurtulus O, Seker E, Wachsmann-Hogiu S. Fabrication and characterization of flexible and tunable plasmonic nanostructures. *Scientific Reports*. 2013; **3**:3396. DOI: 10.1038/srep03396
- [148] Liu Y, Li X, Cheng J, et al. SERS devices with “hedgehog-like” nanosphere arrays for detection of trace pesticides. *Journal of Innovative Optical* Health Sciences. 2021; **14(04)**:2141005. DOI: 10.1142/S1793545821410054
- [149] Rahaman M, Aslam MA, He L, Madeira TI, Zahn DRT. Plasmonic hot electron induced layer dependent anomalous Fröhlich interaction in InSe. *Communications on Physics*. 2021; **4(1)**:172. DOI: 10.1038/s42005-021-00674-5
- [150] Cao Y, Sun M. Tip-enhanced Raman spectroscopy. *Reviews in Physics*. 2022; **8**:100067. DOI: 10.1016/j.revip.2022.100067
- [151] Gersten J, Nitzan A. Electromagnetic theory of enhanced Raman scattering by molecules adsorbed on rough surfaces. *The Journal of Chemical Physics*. 1980; **73(7)**:3023-3037. DOI: 10.1063/1.440560
- [152] Liao PF, Wokaun A. Lightning rod effect in surface enhanced Raman scattering. *The Journal of Chemical Physics*. 1982; **76(1)**:751-752. DOI: 10.1063/1.442690
- [153] Richard-Lacroix M, Zhang Y, Dong Z, Deckert V. Mastering high resolution tip-enhanced Raman spectroscopy: Towards a shift of perception. *Chemical Society Reviews*. 2017; **46(13)**:3922-3944. DOI: 10.1039/c7cs00203c
- [154] Trautmann S, Aizpurua J, Götze I, et al. A classical description of subnanometer resolution by atomic features in metallic structures. *Nanoscale*. 2017; **9(1)**:391-401. DOI: 10.1039/c6nr07560f
- [155] Zhang W, Cui X, Martin OJF. Local field enhancement of an infinite conical metal tip illuminated by a focused beam. *Journal of Raman Spectroscopy*. 2009; **40(10)**:1338-1342. DOI: 10.1002/jrs.2439

- [156] Huang T-X, Huang S-C, Li M-H, Zeng Z-C, Wang X, Ren B. Tip-enhanced Raman spectroscopy: Tip-related issues. *Analytical and Bioanalytical Chemistry*. 2015;**407**(27):8177-8195. DOI: 10.1007/s00216-015-8968-8
- [157] Fleischer M. Near-field scanning optical microscopy nanoprobe. *Nanotechnology Reviews*. 2012; **1**(4):313-338. DOI: 10.1515/ntrev-2012-0027
- [158] Yang B, Kazuma E, Yokota Y, Kim Y. Fabrication of sharp gold tips by three-electrode electrochemical etching with high controllability and reproducibility. *Journal of Physical Chemistry C*. 2018;**122**(29):16950-16955. DOI: 10.1021/acs.jpcc.8b04078
- [159] Foti A, Barreca F, Fazio E, et al. Low cost tips for tip-enhanced Raman spectroscopy fabricated by two-step electrochemical etching of 125  $\mu\text{m}$  diameter gold wires. *Beilstein Journal of Nanotechnology*. 2018;**9**:2718-2729. DOI: 10.3762/bjnano.9.254
- [160] Lopes M, Toury T, La Chapelle ML, de, Bonaccorso F, Gucciardi PG. Fast and reliable fabrication of gold tips with sub-50 nm radius of curvature for tip-enhanced Raman spectroscopy. *The Review of Scientific Instruments*. 2013; **84**(7):73702. DOI: 10.1063/1.4812365
- [161] Yang L-K, Huang T-X, Zeng Z-C, et al. Rational fabrication of a gold-coated AFM TERS tip by pulsed electrodeposition. *Nanoscale*. 2015;**7**(43):18225-18231. DOI: 10.1039/c5nr04263a
- [162] Huang T-X, Li C-W, Yang L-K, et al. Rational fabrication of silver-coated AFM TERS tips with a high enhancement and long lifetime. *Nanoscale*. 2018;**10**(9):4398-4405. DOI: 10.1039/c7nr08186c
- [163] Park C-G, Kim J-Y, Lee E-B, et al. Tip-enhanced Raman scattering with a nanoparticle-functionalized probe. *Bulletin of the Korean Chemical Society*. 2012;**33**(5):1748-1752. DOI: 10.5012/bkcs.2012.33.5.1748
- [164] Wang D, Zhang Z, Wang J, Ma K, Gao H, Wang X. Nanofocusing performance of plasmonic probes based on gradient permittivity materials. *Journal of Optics*. 2022;**24**(6):65003. DOI: 10.1088/2040-8986/ac69f6
- [165] Zhang K, Bao Y, Cao M, et al. Low-background tip-enhanced Raman spectroscopy enabled by a Plasmon thin-film waveguide probe. *Analytical Chemistry*. 2021;**93**(21):7699-7706. DOI: 10.1021/acs.analchem.1c00806
- [166] Sanders A, Bowman RW, Zhang L, et al. Understanding the plasmonics of nanostructured atomic force microscopy tips. *Applied Physics Letters*. 2016; **109**(15):153110. DOI: 10.1063/1.4964601
- [167] Pettinger B, Domke KF, Zhang D, Picardi G, Schuster R. Tip-enhanced Raman scattering: Influence of the tip-surface geometry on optical resonance and enhancement. *Surface Science*. 2009;**603**(10-12):1335-1341. DOI: 10.1016/j.susc.2008.08.033
- [168] Xu H, Bjerneld EJ, Aizpurua J, et al. Interparticle coupling effects in surface-enhanced Raman scattering. *Journal of Gastroenterology and Hepatology*. 2008; **23**(5):35-42. DOI: 10.1117/12.430771
- [169] Yang Z, Aizpurua J, Xu H. Electromagnetic field enhancement in TERS configurations. *Journal of Raman Spectroscopy*. 2009;**40**(10):1343-1348. DOI: 10.1002/jrs.2429
- [170] He L, Rahaman M, Madeira TI, Zahn DRT. Understanding the role of different substrate geometries for



achieving optimum tip-enhanced Raman scattering sensitivity. *Nanomaterials (Basel)*. 2021;**11**(2):376. DOI: 10.3390/nano11020376

[171] Politano A, Formoso V, Chiarello G. Dispersion and damping of gold surface Plasmon. *Plasmonics*. 2008;**3**(4): 165-170. DOI: 10.1007/s11468-008-9070-2

[172] Madoyan KK, Melikyan AH, Minassian HR. Radiation damping of surface Plasmons in a pair of nanoparticles and in nanoparticles near interfaces. *Journal of Physical Chemistry C*. 2012;**116**(31):16800-16805. DOI: 10.1021/jp305144u

[173] Kolwas K, Derkachova A. Damping rates of surface plasmons for particles of size from nano- to micrometers; reduction of the nonradiative decay. *Journal of Quantitative Spectroscopy and Radiative Transfer*. 2013;**114**:45-55. DOI: 10.1016/j.jqsrt.2012.08.007

[174] Milekhin AG, Rahaman M, Rodyakina EE, Latyshev AV, Dzhagan VM, Zahn DRT. Giant gap-plasmon tip-enhanced Raman scattering of MoS<sub>2</sub> monolayers on Au nanocluster arrays. *Nanoscale*. 2018;**10**(6):2755-2763. DOI: 10.1039/c7nr06640f

[175] Liao M, Jiang S, Hu C, et al. Tip-enhanced Raman spectroscopic imaging of individual carbon nanotubes with subnanometer resolution. *Nano Letters*. 2016;**16**(7):4040-4046. DOI: 10.1021/acs.nanolett.6b00533



# Types of Nonlinear Interactions between Plasmonic-Excitonic Hybrids

*Kaweri Gambhir and Agnikumar G. Vedeshwar*

## Abstract

The unique ability of plasmonic structures to concentrate and manipulate photonic signals in deep sub-wavelength domain provides new efficient pathways to generate, guide, modulate and detect light. Due to collective oscillations exhibited by the conducting electrons of metallic nanoparticles, their local fields can be greatly enhanced at the localized surface plasmon resonance (LSPR). Hence, they offer a versatile platform, where localized surface plasmons can be tuned over a broad range of wavelengths by controlling their shape, size and material properties. It has been realized that plasmonic excitations can strengthen nonlinear optical effects in three ways. First, the coupling between the incident beam of light and surface plasmons results in a strong local confinement of the electromagnetic fields, which in turn enhances the optical response. Second, the sensitivity of plasmonic excitations toward the dielectric properties of the metal and the surrounding medium forms the basis for label-free plasmonic sensors. Finally, the excitation and relaxation dynamics of plasmonic nanostructures responds to a timescale of femtoseconds regime, thus allowing ultrafast processing of the incident optical signals. This chapter aims to discuss all the aforementioned interactions of plasmons and their excitonic hybrids in detail and also represent a glimpse of their experimental realizations.

**Keywords:** plasmon, exciton, nonlinear interactions, resonant interactions, nonresonant interactions

## 1. Introduction

The basic requirement for the realization of ultrafast photonic switches, optical limiters and modulators is substantial third-order optical nonlinearity of materials at low light powers [1–3]. However, most of the natural materials possess insignificant nonlinearity in the low light regime [4]. Therefore, design and fabrication of nanoengineered hybrid materials with tunable absorption/emission spectra and considerable third-order optical nonlinearity are a topic of global research [3, 5–7].

It has been realized that plasmonic oscillations can enhance nonlinear optical (NLO) effects majorly in three ways.

First, the coupling between the incident beam and surface plasmons results in a strong local confinement of the electromagnetic fields which in turn enhances the

optical response [8, 9]. This phenomenon forms the basis of surface-enhanced Raman scattering (SERS), where plasmonic excitations arising from metal nanosurfaces are used to boost otherwise weak Raman process by several orders of magnitude [10, 11].

Second, the sensitivity of plasmonic excitations towards the dielectric properties of the metal and the surrounding medium forms the basis for label-free plasmonic sensors. Even the slightest alterations in the refractive index of the environment surrounding the metal surface leads to considerable modifications in the resonance of the plasmonic nanostructures [12, 13]. In nonlinear optical phenomena, this extraordinary sensitivity may be effectively used to control photon-photon interaction. Where, the control beam may be used to modify the dielectric properties of the medium, which in turn would change the plasmonic resonances of the propagating signal beam [14].

Finally, the excitation and relaxation dynamics of plasmonic nanostructures responds to a timescale of femtoseconds regime, thus allowing ultrafast processing of the incident optical signals [15, 16]. This property of plasmonic nanostructures may be conveniently exploited to attain an ultrahigh switching contrast in *All Optical Switching* applications.

Thus, the confinement of surface plasmons in the nanoscale regime not only provides a flexible means of tailoring the optical properties of plasmonic nanostructures but also allows hybridization of metal nanostructures with other molecules such as semiconductors, organic molecules, inorganic molecules [17, 18]. Exclusively, plasmonic-organic hybrids have gathered a lot of attention due to their flexible and versatile interaction mechanisms which can be further fine-tuned to achieve the desired photonic characteristics. Plasmon coupled organic molecules have led to substantial progress in high-throughput DNA detection [19, 20], bio-imaging [21], drug delivery [22], photovoltaic [23] and light-emitting diodes [24], surface-enhanced Raman spectroscopy [11], nanoscale lasers [25], ultrasensitive chemical and biological sensors [26].

## 2. Nonlinear light-matter interactions

The interaction of light with matter can be broadly classified in two categories (a) linear interaction (weak light regime) and (b) nonlinear interaction (intense light regime). When the intensity of the incident beam is so high that it is nearly equal to the internal electric field of the atom then the absorption coefficient and the real and imaginary part of the nonlinear refractive index ( $n$ ) and absorption coefficient ( $\beta$ ) of the material become a function of the incident intensity or electric field [27]. Such that, polarization of the materials tends to behave nonlinearly with the incident electric field (Eq. (1)).

$$P_i = \epsilon_0 \chi_{ijk}^{(1)} E_j + \epsilon_0 \chi_{ijk}^{(2)} E_j E_k + \epsilon_0 \chi_{ijk}^{(3)} E_j E_k E_l + \dots \quad (1)$$

where,  $\epsilon_0$  denotes permittivity of free space,  $P$  is electric polarization,  $\chi$  symbolizes electric susceptibility tensor,  $\epsilon_0 \chi_{ijk}^{(1)} E_j$  is the linear polarization,  $\epsilon_0 \chi_{ijk}^{(2)} E_j E_k$  depicts second order nonlinearity,  $\epsilon_0 \chi_{ijk}^{(3)} E_j E_k E_l$  is the third order nonlinearity and so on.

Hence, in comparison with the linear interaction, during nonlinear interaction superposition principle gets violated, light can alter its frequency as it passes through a

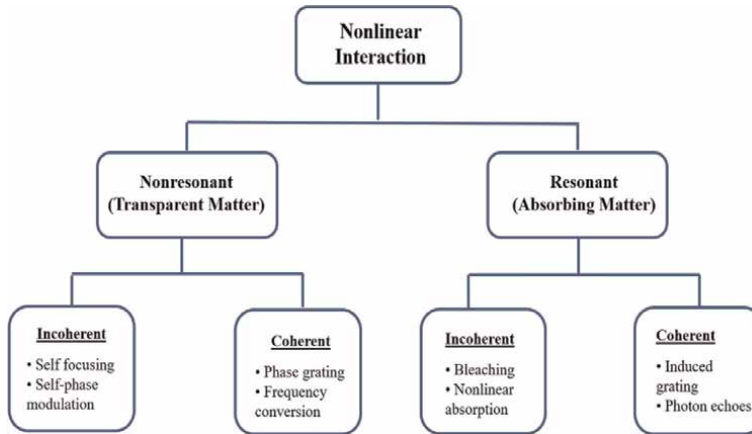


**Figure 1.**  
 Schematic representation of nonlinear interaction of light with matter [27].

NLO material and photons start interacting with each other within the confines of a NLO medium [27, 28]. The nonlinear interactions of light are further classified as resonant and nonresonant interactions (**Figure 1**).

The nonresonant or elastic interactions are the ones in which the incident light is not absorbed by the material (sample). Therefore, these interactions can be described using nonlinear polarization in terms of the Maxwell equations, whereas, in case of resonant interactions or coherent interactions emission/absorption of light inside the material takes place. The density matrix formalism is hence used to evaluate such interactions as discrete structure of the energy levels inside matter and their phase dependent occupation during the light wave period are important to be considered in these interactions [27, 28].

When high intensity light is incident on a medium, based on its inherent response scattering, refraction or absorption takes place. This in turn alters the transmittance of the medium as a function of the input light intensity and is termed as nonlinear light absorption or nonlinear light transmission. However, at very high intensities, the probability of the medium absorbing more than one photon before relaxing to the ground state becomes prominent.

A few phenomena that control nonlinear light transmission are listed below.

## 2.1 Saturable absorption

Saturable absorption (SA) is the mechanism in which the absorption of light is inversely proportional to light intensity. That is at sufficiently high intensities of the incident beam, if the rate of excitation of atoms is greater than their decay rate then the ground state gets depleted resulting in a saturable absorption. Further, this phenomenon critically depends on the absorption range of the material, its dynamic response and saturation intensity.

The steady state rate equation for saturable absorption is denoted by Eq. (2).

$$\frac{dN}{dt} = \frac{\sigma I}{h\nu} (N_g - N) - \frac{N}{\tau} \quad (2)$$

where,  $N$  is the number of excited state molecules,  $N_g$  is the undepleted ground state concentration,  $\sigma$  is termed as absorption cross section,  $h\nu$  is the photon energy, and  $\tau$  is the lifetime of the excited state population.

Assuming that the absorption coefficient and  $\alpha$  is proportional to the ground state population. Saturable absorption finds application in passive mode locking and Q-switching of lasers and optical signal processing [27, 28].

## 2.2 Two-photon absorption

When simultaneous absorption of two photons from an incident beam causes a transition of atoms/molecules of a material from ground state to a higher energy level, this phenomenon is termed as two-photon absorption (TPA). The intermediate level in this case is a virtual energy level therefore; two photons should be simultaneously absorbed for this process to occur. Also TPA is directly proportional to the square of the input fluence. The propagation of laser light through the system describing the TPA is given by Eq. (3).

$$\frac{dI}{dZ} = -\alpha I - \beta I^2 \quad (3)$$

where,  $\alpha$  is the linear absorption coefficient and  $\beta$  is the two-photon absorption coefficient and  $\sigma$  is the individual molecular two-photon absorption cross section, also

$$\sigma = \frac{\omega\beta h}{2\pi N} \quad (4)$$

where  $N$  is the number of the molecules in the system and  $\omega$  is the incident radiation frequency. It is the imaginary part of the third-order nonlinear susceptibility of the system that determines the strength of the two-photon absorption. The relation between the TPA coefficient and the third-order susceptibility of a centrosymmetric system for linearly polarized incident light is given as,

$$\beta = \frac{3\pi}{\epsilon_0 n^2 c \lambda} \text{Im} [\chi^3_{xxx}(-\omega; \omega, \omega, -\omega)] \quad (5)$$

here,  $c$  is the speed of light,  $\lambda$  is the wavelength of the incident beam and  $n$  is the linear refractive index [27].

## 2.3 Three-photon absorption

The transition of a ground state molecule to higher excited state by simultaneous absorption of three photons from the incident radiation is termed as three-photon absorption (3PA) [28]. It is a fifth-order nonlinear process, and the propagation equation for a medium having significant three-photon absorption is given as,

$$\frac{dI}{dZ} = -\alpha I - \gamma I^3 \quad (6)$$

where,  $\alpha$  is the linear absorption coefficient and  $\gamma$  is the 3PA coefficient. For acentrosymmetric system and linearly polarized light,  $\gamma$  is related to the imaginary part of the fifth-order susceptibility through the following equation,

$$\gamma = \frac{5\pi}{\epsilon_0^2 n^3 c^2 \lambda} \text{Im} [\chi_{xxxxx}^5(-\omega; \omega, \omega, \omega, -\omega, -\omega)] \quad (7)$$

## 2.4 Reverse saturable absorption

Reverse saturable absorption (RSA) is the property of materials where the absorption of light increases with increasing incident light intensity. It is basically a two-step, sequential single-photon absorption process where, the excited atoms/molecules make a subsequent transition to higher energy levels by absorbing another single photon [28]. For steady-state condition, the intensity change of the laser beam in the nonlinear medium along its propagation direction for RSA can be expressed as,

$$\frac{dI}{dz} = -\sigma_{12}(N_1 - N_2)I - \sigma_{23}N_2I \quad (8)$$

where,  $\sigma_{12}$  is the transition crosssection from the ground state to first excited state,  $N_1$  is the no. of molecules in the first excited state,  $N_2$  is the no. of molecules in the second excited state and  $\sigma_{23}$  is the transition crosssection from first excited state to second excited state.

## 3. Types of plasmon-exciton interaction

Based on the spectral overlap between the plasmonic modes and optical exciton of the organic molecules their mutual interaction mechanism is broadly classified into nonresonant and resonant interactions.

### 3.1 Nonresonant interaction

These types of interactions are further classified into refractive index-dependent interaction and plasmon enhanced fluorescence.

#### 3.1.1 Refractive index dependent

The type of interaction between plasmonic-organic hybrids where the electronic absorption band of the organic molecule and the plasmonic resonances are far away from each other and the refractive index of the organic molecule is nearly wavelength independent (**Figure 2A**). The adsorption of organic molecules merely increases the refractive index or the dielectric constant of the nanoenvironment surrounding metal nanocrystals. Therefore, as the induced polarization charges increase, a more pronounce screening of the Columbic restoring effect leading to a red shift in the resonance band of the plasmonic nanostructures [7, 29]. A prime example of such a plasmon molecule interaction is refractive index-based sensors where, the adsorption of such organic molecules enhances the refractive index of the environment around the plasmonic nanostructures [30].

#### 3.1.2 Plasmon enhanced fluorescence

The organic molecules which demonstrate both absorption and fluorescence emission, tend to drastically alter their fluorescence rate when hybridized with metal

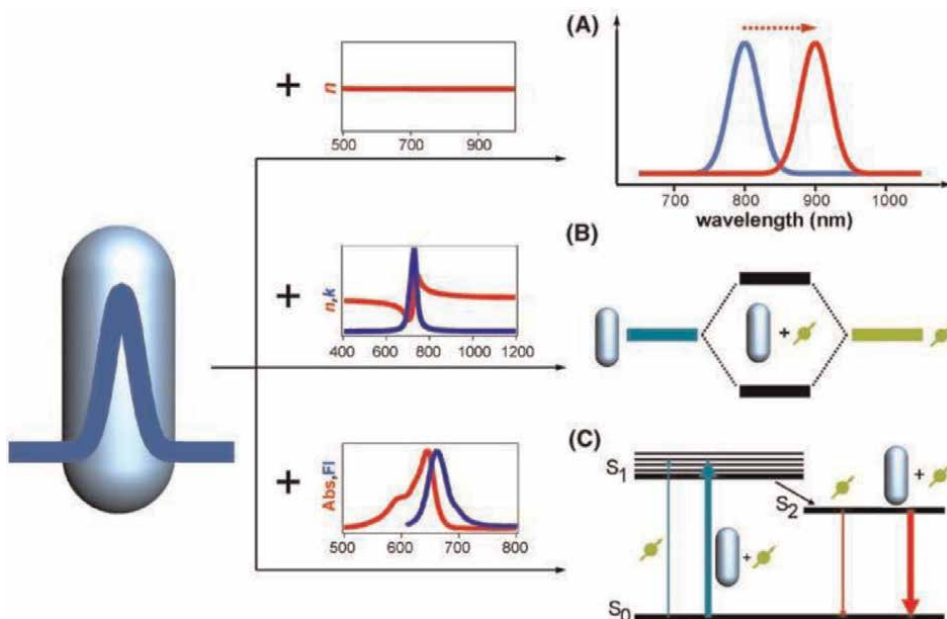


**Figure 2.** Schematic diagram illustrating three types of plasmon-molecule interactions. (A) Plasmon shift due to adsorption; (B) resonance coupling between metal nanocrystals and adsorbed molecules with strong absorption and (C) fluorescence enhancement when fluorophores are adjacent to metal nanocrystals [29].

nanostructures [29, 31]. Primarily, the enhancement in the fluorescence of the organic molecule may be due to an increase in the excitation rate of the electrons from ground state to the excited state which happens due to the strengthening of the local electric field in the vicinity of the metal nanosurfaces. On the contrary fluorescence enhancement may also be attributed to the increase in electronic radiative emission from the excited states to the ground state owing to aggregation of photonic states around the metal nanostructures [7, 32]. In both these phenomena, the distance between the fluorophore and the plasmonic structure plays a key role. Novotny et al. demonstrated that organic fluorophores when conjugated with metal nanoparticles displaying intense local field enhancements then the radiative decay rate dominates the nonradiative decay rate and fluorescence enhancement takes place which further reduces the average lifetime of the organic molecule [33]. Moreover, due to the coupling with the plasmon resonance, the emission direction as well as the spectral shape of fluorophores can also be modified [34–36]. All of these open up new approaches for manipulating light at the nanoscale.

### 3.2 Resonant interactions between plasmons and excitons

Resonant coupling takes place if the absorption band of the organic molecules and the LSPR frequency of the metal nanoparticles overlap with each other. Plasmons when resonantly excited, amplify the local electric multiple times in magnitude. In such a case the coupling between the plasmonic resonances and the degenerate energy levels of the organic molecule leads to hybridized molecular states [7, 29, 31]. Based on the perturbations in the wave functions of the plasmons and, the interaction between them can be classified into weak, strong and extreme coupling [1, 37, 38]. If the wave



functions remain unaltered it is called weak coupling, origination of new dispersion relations due to the formation of hybrid states is referred to as strong coupling regime whereas, in the extreme coupling the resonance exchange energy oscillates between the upper and lower energy levels leading to a split in the absorption band [1, 39].

Pockrand et al. and Glass et al. in 1980 first demonstrated the resonance coupling effect between plasmons and excitons both theoretically and experimentally [40, 41]. Later, it was realized that the ultraviolet and visible light could switch the resonant coupling between the dye molecules and excitons this led to efficient switching with power density  $\sim 6.0 \text{ mW/cm}^2$  and switching power  $0.72 \text{ nW/device}$  [42]. Since then, efforts to decipher interaction mechanisms between strongly coupled plasmons and excitons have gained a lot of interest amongst researchers. Wiederrecht et al. first reported literature on coherent coupling between a J-aggregated molecular dye and noble metallic nanospheres (**Figure 3**) [43].

They demonstrated that the interaction between plasmons and excitons is strongly dependent on the properties of the metal nanostructure. The J-aggregated dye when hybridized with Ag nanocrystals lead to an increased absorption whereas the absorption decreased when integrated with Au nanocrystals [43]. Further, Fofang et al. investigated wavelength-dependent coupling between the J-aggregates of dye 2,2'-dimethyl-8-phenyl-5,6,5',6'-dibenzothiacarbocyanine chloride. Their study claims that the plasmonic resonances can be tuned over a wide spectral range when strongly coupled with a metal nanostructure. In fact, the coupling energy diagram of 2,2'-dimethyl-8-phenyl-5,6,5',6'-dibenzothiacarbocyanine chloride and Au nanoshells hybrids depicted both asymmetric energy splitting and an anticrossing behavior [1]. The anticrossing behavior amongst resonantly coupled hybrids of Au nanorods and various other organic dyes have also been reported [44–47]. One of the major applications demonstrated by resonantly coupled plasmons and organic dyes is ultrasensitive detection of analytes. Where, resonant binding amongst Ag nanoparticles, camphor and cytochrome P450cam protein (CYP101) demonstrated a plasmon shift of up to 104 nm [48, 49]. Therefore, a complete understanding of the resonance coupling effects between plasmonic nanostructures and excitonic

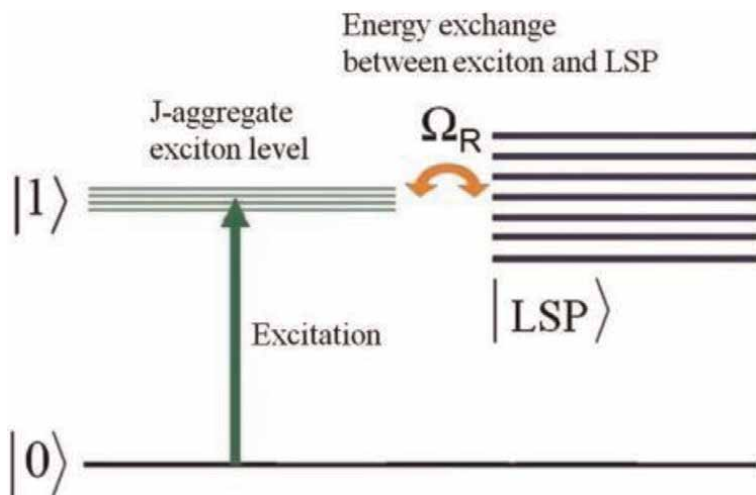


**Figure 3.**  
Schematic diagram of optical transitions in metal-J aggregate hybrid nanostructures.

molecules is of utmost importance for realizing active photonic devices such as optical switches, lasers and energy transfer-based sensors [50].

Since, these interactions between plasmons and excitons cannot be explained by the dielectric function therefore, it was realized that energy transfer plays a vital role in delineating the characteristics of the hybrid states.

### 3.2.1 Exciton-plasmon resonant energy transfer mechanisms

An optically excited excitonic molecule placed in the vicinity of a plasmonic nanostructure may result in an energy transfer *via* radiative or nonradiative channel.

Owing to the physical and chemical conditions the probabilistic resonant interactions between the plasmonic-organic hybrids can be due to Dexter energy transfer (DET), exciton plasmon resonance energy transfer (EPRET), Foster resonance energy transfer (FRET), nanometal surface energy transfer (NSET), metal enhanced fluorescence (MEF), enhancement of absorption cross section (lightening rod effect), enhanced photostability, and the increase of excitation rate [51].

The origin of metal enhanced fluorescence is understood in terms of the increase in optical density of states of the emitter when placed near a metal nanosurface, due to the local confinement of the incident electric field [52, 53]. This in accordance with Purcell effect which leads to an increase in the radiative decay rate of the organic molecule due to a decrease in the volume of the cavity [54].

Further, MEF is extremely sensitive to the orientation of the exciton and nanoparticle (**Figure 4**).

Both experimental and theoretical studies infer that it is the orientation of the exciton and plasmonic dipoles in MEF due to which the net luminance of the hybrid quenches or strengthens.

A radiation less energy transfer from excited state donor to ground state acceptor via long range dipole-dipole interactions is termed as FRET [55, 56].

The efficiency of this energy transfer critically depends on various factors such as the distance of separation between the acceptor and donor molecule, their spectral overlap and their emission quantum yield (QY) [57, 58]. **Figure 5** illustrates the Jablonski Diagram of this mechanism.

FRET plays an important role in the determination of sub-microscopic separations amongst interactive molecules [59, 60]. The dipole-dipole interaction between the

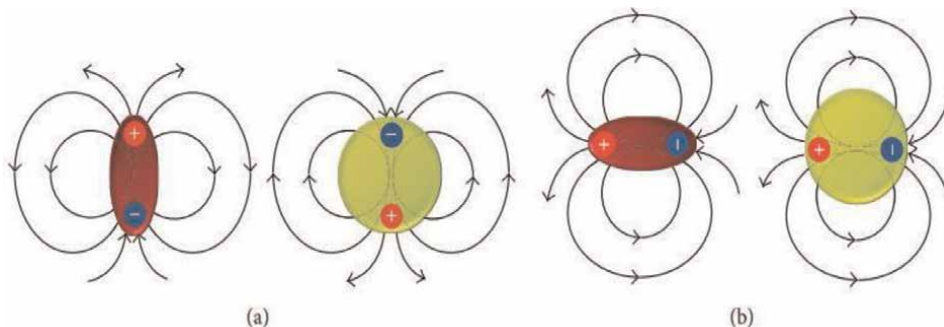


**Figure 4.** (a) Parallel (tangential) and (b) perpendicular (radial) orientation of chromophore dipole moment to the surface of spherical nanoparticles leading to the suppression or enhancement of the radiative decay rate of the exciton, respectively [51].

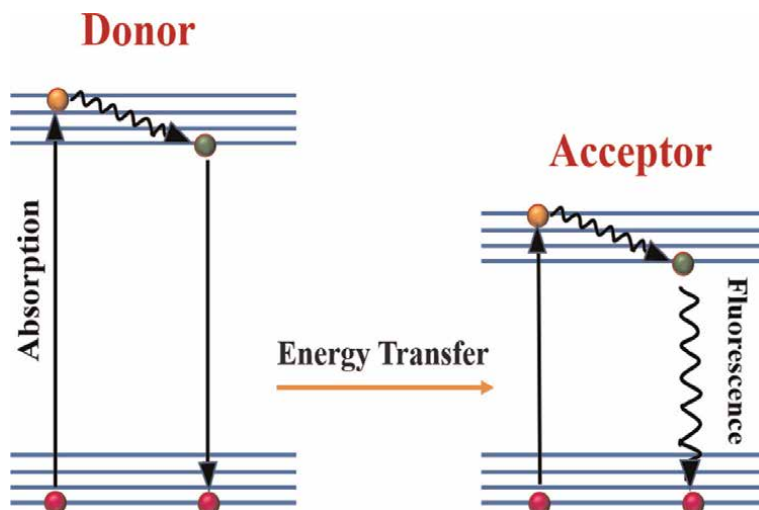


**Figure 5.**  
 Jablonski diagram illustrating FRET [59].

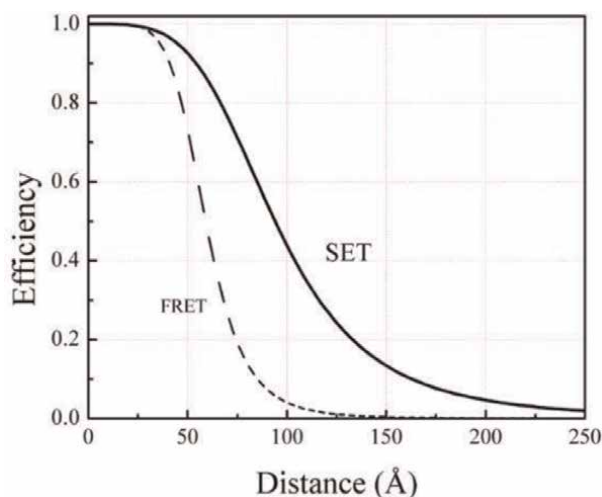


**Figure 6.**  
 Comparison of energy transfer efficiency between FRET and NSET [19].

excited donor molecule (D) and the ground state acceptor molecule (A) results in a nonradiative energy exchange between them in this occurrence. Because the energy transfer efficiency is inversely related to the sixth power of the distance between the donor and acceptor molecules, the length scale of nanoscopic FRET is limited to 8 nm beyond which it is too weak to be used [60]. Further, a long-range dipole-surface contact mechanism based on NSET has recently been developed, with energy transfer range twice that of FRET (**Figure 6**) [19, 29]. In metal nanoparticles, the rate of energy transfer from the oscillating dipole to the continuum of electron-hole pair excitations is inversely proportional to the fourth power of the donor to acceptor distance [61, 62].

In the linear regime, both FRET and NSET have been extensively recognized as an efficient tool for the determination of the distance between the sub-microscopic particles and in predicting the dynamics of a coupled hybrid [29, 63, 64].

EPRET, on the other hand, is a nonradiative dipole-dipole resonant interaction discovered by Forster. The various parameters on which EPRET critically depends are inter-particle distance between the donor and the acceptor, spectral overlap between the excitonic emission band and their plasmonic absorption band, relative orientation of the dipole moments of the organic molecule with respect to the plasmonic modes, strength of transition dipole moment, the morphology of plasmonic nanostructures and concentration and molar extinction coefficient of the plasmonic and organic molecules [51, 65]. A significant contrast between FRET and EPRET is in terms of relative orientation amongst dipoles of the donor and acceptor pair. FRET is forbidden when the dipoles are perpendicular to each other while it is maximum in case of parallel dipoles whereas, for EPRET, the probability of energy transfer is minimum when the relative orientation of the dipoles of the donor acceptor pair is perpendicular to each other, but it is never zero [51].

When the plasmon and exciton are placed very close to each other (5–10 nm) it is found that DET dominates the interaction. This type of energy transfer occurs due to hopping of electrons between the overlapping wave functions of the donor and acceptor molecule [66]. Photo-stability occurs when the short-lived excited states reduce the potential of photo-bleaching and other interactions that would otherwise destroy the chromophores' fluorescent nature, resulting in an increase in their photo-stability [51]. Furthermore, because more excited molecules are now pushed down to the ground state and ready to absorb and participate in the emission process, this impact raises the molecules excitation rate, resulting in an increase in the overall emission rate [67]. Another effect which is closely related is the lightning rod effect and it takes place when the absorption band of the chromophore overlaps with the plasmon band of the nanoparticle. In this phenomenon, the plasmon band of the nanoparticle acts as a receiver nanoantenna and confines the electromagnetic field, and this significantly strengthens the excitation rate of the chromophore and thus enhances the total emission rate [51].

#### **4. Experimental realizations**

With an aim to circumvent the material bottleneck limitations hindering the realization of an on chip all optical switch, our experimental work presents a detailed insight into the morphology directed third order NLO properties of four distinct gold nanoshapes and their hybrids with an organic fluorescent dye Eosin Yellow (EY). The ultrafast structural dynamics of the gold nanoshapes and their hybrids has been delineated in terms of their spectral and temporal modulations to deconvolute the excited state dynamics responsible for the coupling between the transient states of gold nanoshapes and various intermediate states of the Eosin Yellow photocycle. Finally, the work is concluded with a mechanistic interpretation of the observed phenomenon in terms of the energy transfer within the hybrids.

In our investigations, colloidal gold nanoshapes were synthesized using chemical reduction method (**Figure 7**) while, the DC sputtering technique has been employed for fabricating the gold nanoislands film [67, 68].

Apart from this, films of Eosin Yellow having different concentrations were spin coated on a glass substrate. The shape and lattice parameters of colloidal gold

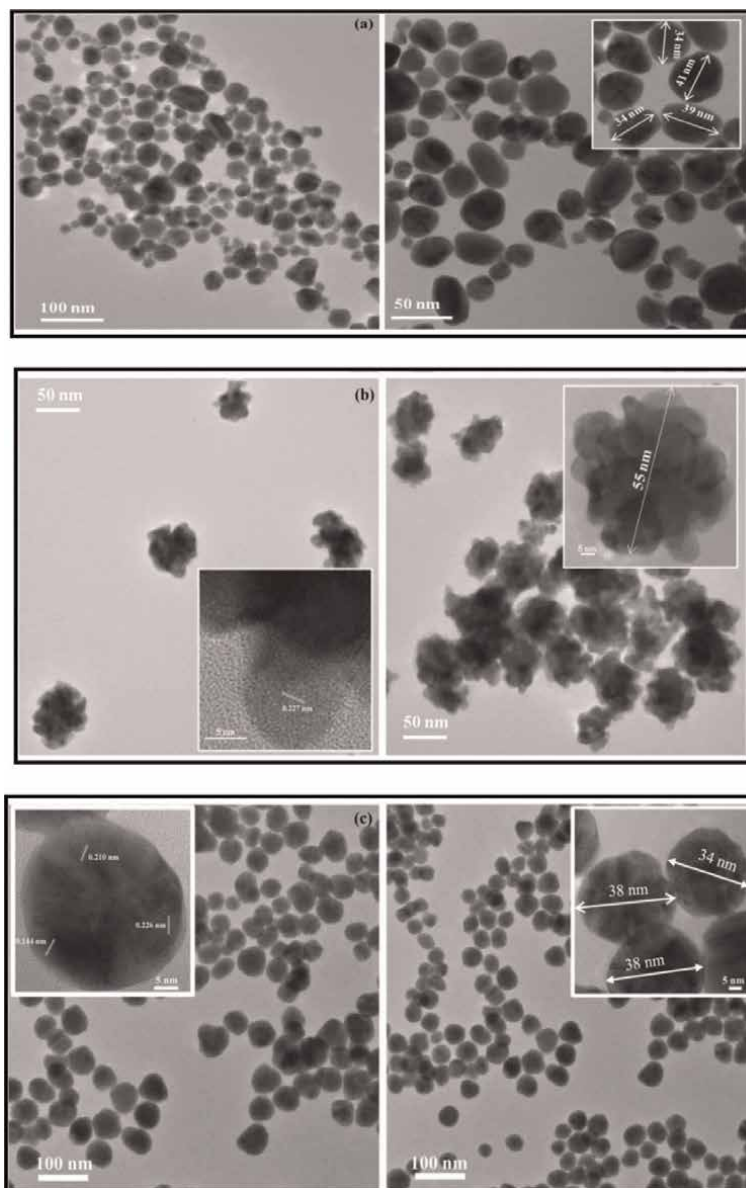


**Figure 7.** TEM micrographs (a) GNP (gold nanopebbles); (b) GNF (gold nanoflowers) and (c) GNS (gold nanospheres). While, the insets represent the HR-TEM image of the corresponding nanoparticles [67].

nanostructures were estimated using high resolution transmission electron microscopy (HRTEM) and X-ray diffraction (XRD) respectively. Atomic force microscopy (AFM), field-emission scanning electron Microscopy (FESEM) and near field scanning optical microscopy (NSOM) were employed to examine the morphology of the epitaxial gold film and its interaction with the organic counterpart respectively **Figures 8–10** [67, 68].

Further, various standard spectroscopic characterizations namely absorption spectroscopy (UV-Vis), surface enhanced Raman spectroscopy (SERS), third order

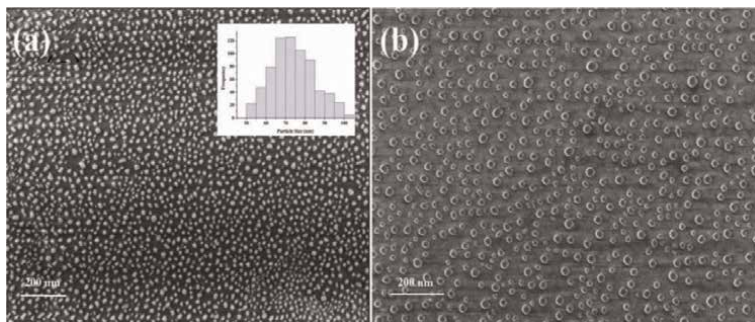


**Figure 8.** FESEM image of (a) gold Nanoislands film at high magnification (inset represents the particle size distribution) and (b) EY-gold nanoislands hybrid [68].

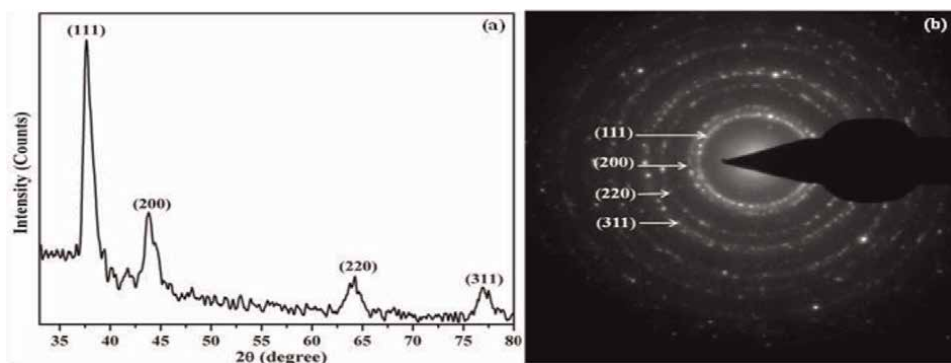


**Figure 9.** (a) Powder X-ray diffraction pattern and (b) selected area electron diffraction pattern of Au colloids demonstrating FCC structure [67].

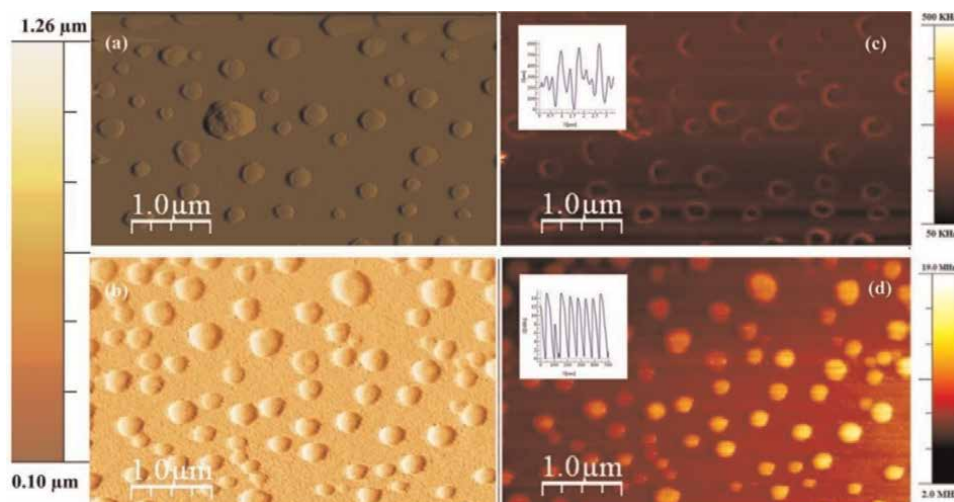


**Figure 10.** (a, b) AFM representation of bare Au-islands and EY-Au islands hybrid, respectively and (c, d) 2-D NSOM image of the raw gold nanoislands and EY-Gold nanoislands film, respectively (inset represents the intensity of field in terms of oscillation with maxima and minima in the  $x-z$  plane) [68].

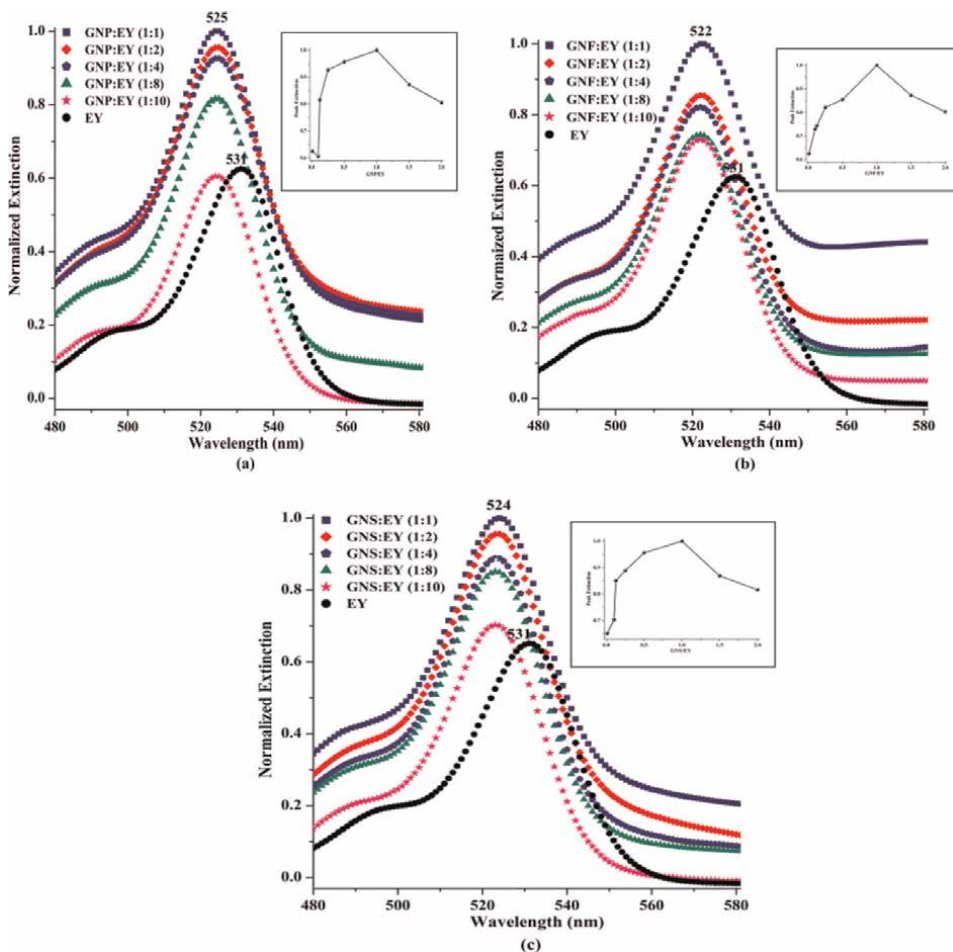


**Figure 11.** Normalized extinction spectra of free Eosin Yellow (EY) and its hybrid with (a) GNP; (b) GNF and (c) GNS. The insets represent peak extinction maxima (normalized w.r.t 1:1 (v/v) gold nanoparticles-EY ratio) of the hybrid structures [67].

nonlinear spectroscopy (Z-Scan), photoluminance spectroscopy (PL) and ultrafast time resolved pump probe spectroscopy (UTRPPS) have been used to unveil the steady state as well as the excited state dynamics of all four distinct gold nanoshapes and their hybrids with EY (**Figures 11–14**). For a detailed explanation regarding the synthesis, experimental setups employed and the experimental results the corresponding papers may be referred [67–69].

## 5. Conclusions of the experimental analysis

The linear absorbance, nonlinear absorption coefficient and nonlinear refractive index measurements of the four distinct plasmonic shapes, namely colloidal gold nanoflowers, colloidal gold nanopebbles colloidal gold nanospheres and gold nanoislands film confirmed that not only size but the geometry of the plasmonic structures plays a vital role in determining their linear as well as nonlinear optical

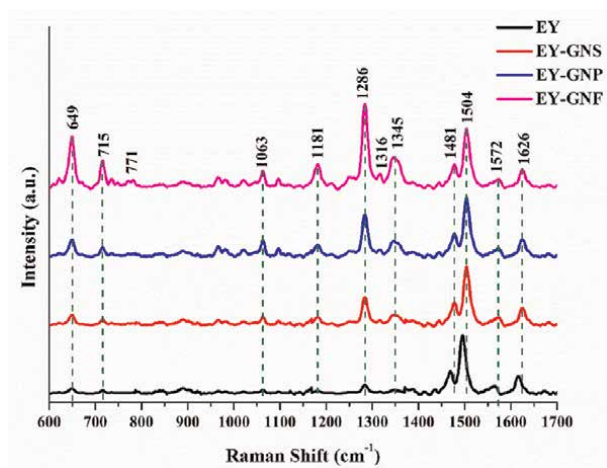


**Figure 12.** (a) Raman spectra of Eosin Yellow dye and its hybrids illustrating morphology directed SERS effect [68].

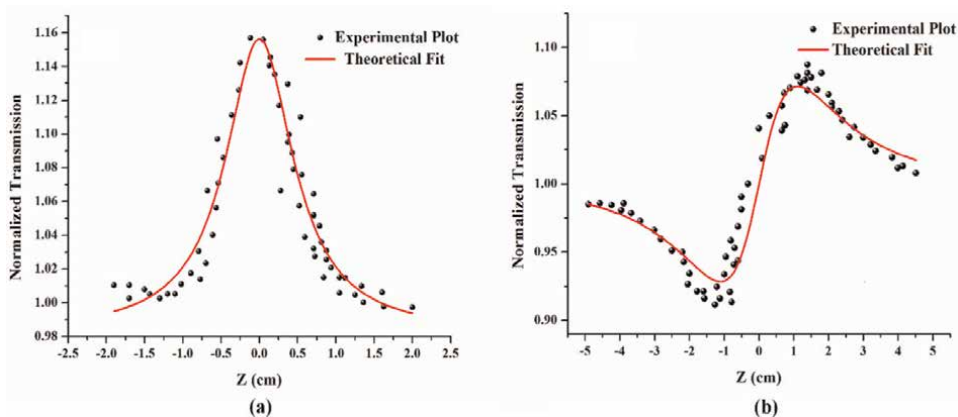


**Figure 13.** Z-scan representation of Eosin Yellow dye (a) open aperture and (b) closed aperture scan [67].

coefficients. A strong mutual interaction between the organic dye Eosin Yellow and plasmonic structures has been inferred from the Raman spectroscopic analysis. Further, the observed results deduce that the nanostructures with sharp edges, offering plenty of hotspots, may be competitive candidates for highly sensitive SERS probes. Nonlinear transmission measurements of colloidal plasmonic shapes, organic fluorophore EY and their colloidal plasmonic organic hybrids show that they possess excellent saturable absorption properties at 532 nm wavelength. Further, the Two Photon Absorption coefficients reported for colloidal plasmonic organic hybrids reveal that the enhancement induced by the plasmonic structures in the in the third order nonlinearity of the organic dye Eosin Yellow critically depends on the morphology of the plasmonic structures. Further, the results based on the spectral and temporal modulations of EY hybrids in solution and film demonstrated that the excitonic states of molecular hybrids tend to modify drastically due to strong coupling between molecular excitons and plasmons. The energy transfer mechanism delineated for all the four EY-gold nanoshapes hybrids depicts that Forster resonance energy transfer



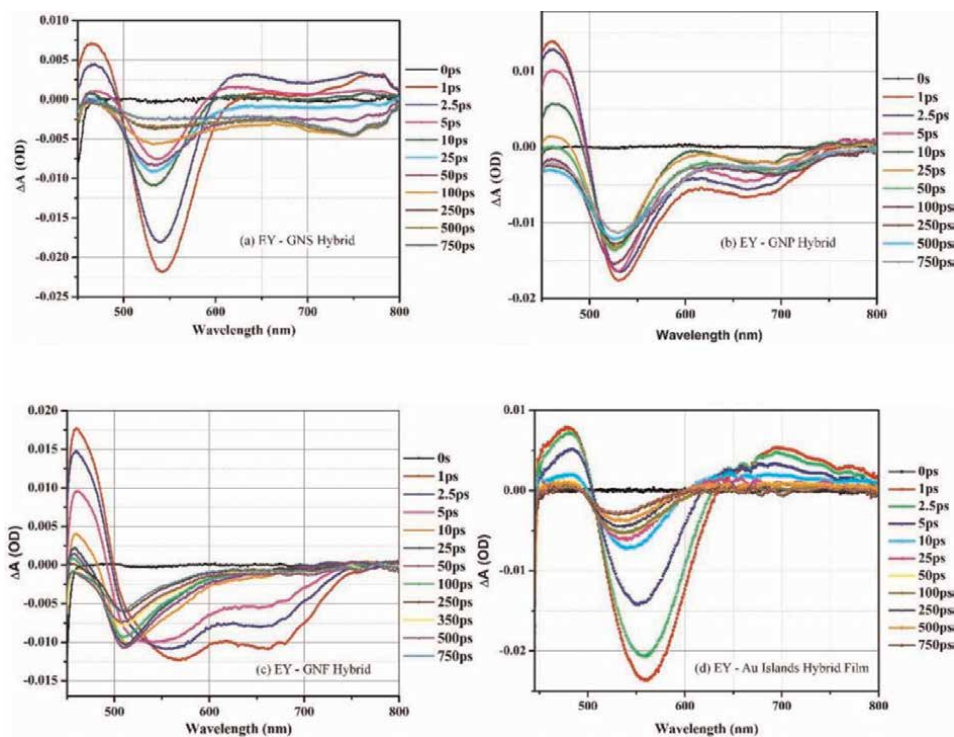


**Figure 14.** Transient absorption spectra at various time delays measured for EY when hybridized with (a) colloidal gold nanospheres; (b) colloidal gold nanopebbles; (c) colloidal gold nanoflowers and (d) nanoislands film pumped at visible wavelength (420 nm, power = 1.5 mW) [69].

(FRET) took place between EY-GNS, EY-GNP and EY-Au islands while nanometal surface energy transfer (NSET) existed between EY-GNF.

These findings may find importance in fabrication of energy transfer based active photonic devices.

## 6. Summary

The work reported herein, presents a significant enhancement in the third-order nonlinearity of a technologically promising organic dye Eosin yellow (EY) when hybridized with three distinct colloidal gold nanoshapes, namely, gold nanospheres (GNS), gold nanopebbles (GNP) and gold nanoflowers (GNF) and a gold nanoislands film (Au islands). Indeed, up to 400% increase in the NLO response of EY when hybridized with Au islands was demonstrated when excited with a 532 nm, 20 ps laser. Further, a 50% reduction in the response time been attained. Herein, the role of resonant interactions within the hybrids especially in terms of nonradiative energy in altering the steady state as well as excited state dynamics due to the spectral overlap between the extinction spectra of the gold nanoshapes and the emission spectra of the dye has been emphasized. Finally, a descriptive uncertainty budget for the precise measurement of the third order NLO coefficients has been documented.

Based on the hypothesis that the nonradiative energy transfer has the ability to significantly alter steady state as well as excited state dynamics of plasmonic organic

hybrids and a unique relationship exists between the efficiency of energy transfer and the enhancement in the third order NLO coefficients, this study may be safely extended to a wide range of energy transfer-based plasmonic-organic hybrids.

## **Acknowledgements**

The authors are thankful to the Department of Physics and Astrophysics, University of Delhi, Delhi 110007, India, for granting permission to publish this work. Kaweri Gambhir acknowledges financial support from Dr. D. S. Kothari Postdoctoral Research Fellowship, University Grant Commission, India, through Grant No. No. F.4-2/2006 (BSR)/PH/19-20/0097.


## **Author details**

Kaweri Gambhir\* and Agnikumar G. Vedeshwar  
Thin Film Laboratory, Department of Physics and Astrophysics, University of Delhi,  
Delhi, India

\*Address all correspondence to: kawerigambhir@gmail.com

## **IntechOpen**

---

© 2022 The Author(s). Licensee IntechOpen. This chapter is distributed under the terms of the Creative Commons Attribution License (<http://creativecommons.org/licenses/by/3.0>), which permits unrestricted use, distribution, and reproduction in any medium, provided the original work is properly cited. 

## References

- [1] Fofang NT, Grady NK, Fan Z, Govorov AO, Halas NJ. Plexciton dynamics: Exciton-plasmon coupling in a J-aggregate-Au nanoshell complex provides a mechanism for nonlinearity. *Nano Letters*. 2011;**11**(4):1556-1560
- [2] Shcherbakov MR, Vabishchevich PP, Shorokhov AS, Chong KE, Choi D-Y, Staude I, et al. Ultrafast all-optical switching with magnetic resonances in nonlinear dielectric nanostructures. *Nano Letters*. 2015;**15**(10):6985-6990
- [3] Gambhir K, Sharma P, Mehrotra R. Morphology-directed nanoscopic energy transfers in plasmonic-organic hybrids. *Journal of Applied Spectroscopy*. 2021; **88**(1):203-214
- [4] Chang DE, Vuletić V, Lukin MD. Quantum nonlinear optics—photon by photon. *Nature Photonics*. 2014;**8**(9): 685-694
- [5] Ding F, Wang Z, He S, Shalaev VM, Kildishev AV. Broadband high-efficiency half-wave plate: A supercell-based plasmonic metasurface approach. *ACS Nano*. 2015;**9**(4):4111-4119
- [6] Kucherenko M, Nalbandyan V. Absorption and spontaneous emission of light by molecules near metal nanoparticles in external magnetic field. *Physics Procedia*. 2015;**73**:136-142
- [7] Wilson AJ, Willets KA. Surface-enhanced Raman scattering imaging using noble metal nanoparticles. *Wiley Interdisciplinary Reviews: Nanomedicine and Nanobiotechnology*. 2013;**5**(2):180-189
- [8] Zayats AV, Smolyaninov II, Maradudin AA. Nano-optics of surface plasmon polaritons. *Physics Reports*. 2005;**408**(3-4):131-314
- [9] Novotny L, Van Hulst N. Antennas for light. *Nature Photonics*. 2011;**5**(2): 83-90
- [10] Li G, Zhang X, Zheng F, Liu J, Wu D. Emerging nanosensing technologies for the detection of  $\beta$ -agonists. *Food Chemistry*. 2020;**332**: 127431
- [11] Balčytis A, Nishijima Y, Krishnamoorthy S, Kuchmizhak A, Stoddart PR, Petruškevičius R, et al. From fundamental toward applied SERS: Shared principles and divergent approaches. *Advanced Optical Materials*. 2018;**6**(16):1800292
- [12] Hess O, Pendry JB, Maier SA, Oulton RF, Hamm JM, Tsakmakidis KL. Active nanoplasmonic metamaterials. *Nature Materials*. 2012;**11**(7):573-584
- [13] Amiri IS, Azzuhri SRB, Jalil MA, Hairi HM, Ali J, Bunruangses M, et al. Introduction to photonics: Principles and the most recent applications of microstructures. *Micromachines*. 2018; **9**(9):452
- [14] Kauranen M, Zayats AV. Nonlinear plasmonics. *Nature Photonics*. 2012; **6**(11):737-748
- [15] Stockman MI. Nanoplasmonics: Past, present, and glimpse into future. *Optics Express*. 2011;**19**(22): 22029-22106
- [16] Stockman MI, Kneipp K, Bozhevolnyi SI, Saha S, Dutta A, Ndukaife J, et al. Roadmap on plasmonics. *Journal of Optics*. 2018; **20**(4):043001
- [17] Sukharev M, Nitzan A. Optics of exciton-plasmon nanomaterials. *Journal*

- of Physics: Condensed Matter. 2017; **29**(44):443003
- [18] Li X, Zhou L, Hao Z, Wang QQ. Plasmon–exciton coupling in complex systems. *Advanced Optical Materials*. 2018;**6**(18):1800275
- [19] Breshike CJ, Riskowski RA, Strouse GF. Leaving Forster resonance energy transfer behind: Nanometal surface energy transfer predicts the size-enhanced energy coupling between a metal nanoparticle and an emitting dipole. *The Journal of Physical Chemistry C*. 2013;**117**(45): 23942-23949
- [20] Yildirim DU, Ghobadi A, Ozbay E. Nanosensors based on localized surface plasmon resonance. *Plasmonic Sensors and Their Applications*. 2021: 23-54
- [21] Ding S-J, Nan F, Liu X-L, Hao Z-H, Zhou L, Zeng J, et al. Plasmon-modulated excitation-dependent fluorescence from activated CTAB molecules strongly coupled to gold nanoparticles. *Scientific Reports*. 2017; **7**(1):1-9
- [22] Doane TL, Burda C. The unique role of nanoparticles in nanomedicine: Imaging, drug delivery and therapy. *Chemical Society Reviews*. 2012;**41**(7): 2885-2911
- [23] Nan F, Ding S-J, Ma L, Cheng Z-Q, Zhong Y-T, Zhang Y-F, et al. Plasmon resonance energy transfer and plexcitonic solar cell. *Nanoscale*. 2016; **8**(32):15071-15078
- [24] Okamoto K, Funato M, Kawakami Y, Tamada K. High-efficiency light emission by means of exciton–surface-plasmon coupling. *Journal of Photochemistry and Photobiology C: Photochemistry Reviews*. 2017;**32**:58-77
- [25] Baffou G, Quidant R. Thermo-plasmonics: Using metallic nanostructures as nano-sources of heat. *Laser & Photonics Reviews*. 2013;**7**(2): 171-187
- [26] Špačková B, Wrobel P, Bocková M, Homola J. Optical biosensors based on plasmonic nanostructures: A review. *Proceedings of the IEEE*. 2016;**104**(12): 2380-2408
- [27] Menzel R. *Photonics: Linear and Nonlinear Interactions of Laser Light and Matter*. Berlin, Heidelberg: Springer Science & Business Media; 2013. DOI: 10.1007/978-3-662-04521-3
- [28] Boyd RW. *Nonlinear Optics*. 4th ed. San Diego, CA: Academic Press; 2020. ISBN: 978-0-12-811002-7
- [29] Chen H, Ming T, Zhao L, Wang F, Sun L-D, Wang J, et al. Plasmon–molecule interactions. *Nano Today*. 2010;**5**(5):494-505
- [30] Grande M, Marani R, Portincasa F, Morea G, Petruzzelli V, D’Orazio A, et al. Asymmetric plasmonic grating for optical sensing of thin layers of organic materials. *Sensors and Actuators B: Chemical*. 2011;**160**(1):1056-1062
- [31] Kamat PV. *Photophysical, Photochemical and Photocatalytic Aspects of Metal Nanoparticles*. Washington, D.C: ACS Publications; 2002. pp. 7729-7744. DOI: 10.1021/jp0209289
- [32] Pradhan N, Das Adhikari S, Nag A, Sarma D. Luminescence, plasmonic, and magnetic properties of doped semiconductor nanocrystals. *Angewandte Chemie International Edition*. 2017;**56**(25):7038-7054
- [33] Novotny L, Hecht B. *Principles of Nano-Optics*. Cambridge, United

Kingdom: Cambridge University Press;  
2012. ISBN: 978-1-107-00546-4

[34] Lakowicz JR. Radiative decay engineering 3. Surface plasmon-coupled directional emission. *Analytical Biochemistry*. 2004;**324**(2):153-169

[35] Lakowicz JR, Ray K, Chowdhury M, Szmacki H, Fu Y, Zhang J, et al. Plasmon-controlled fluorescence: A new paradigm in fluorescence spectroscopy. *Analyst*. 2008;**133**(10):1308-1346

[36] Ringler M, Schwemer A, Wunderlich M, Nichtl A, Kürzinger K, Klar T, et al. Shaping emission spectra of fluorescent molecules with single plasmonic nanoresonators. *Physical Review Letters*. 2008;**100**(20):203002

[37] Maier SA, Atwater HA. Plasmonics: Localization and guiding of electromagnetic energy in metal/dielectric structures. *Journal of Applied Physics*. 2005;**98**(1):10

[38] Moerland RJ, Hakala TK, Martikainen J-P, Rekola HT, Väkeväinen AI, Törmä P. Strong Coupling between Organic Molecules and Plasmonic Nanostructures. New York: Springer; 2017. pp. 121-150. ISBN: 978-952-60-8160-1

[39] Wang H, Toma A, Wang H-Y, Bozzola A, Miele E, Haddadpour A, et al. The role of Rabi splitting tuning in the dynamics of strongly coupled J-aggregates and surface plasmon polaritons in nanohole arrays. *Nanoscale*. 2016;**8**(27):13445-13453

[40] Pockrand I, Swalen J, Gordon J, Philpott M. Exciton-surface plasmon interactions. *The Journal of Chemical Physics*. 1979;**70**(7):3401-3408

[41] Glass A, Liao PF, Bergman J, Olson D. Interaction of metal particles

with adsorbed dye molecules: Absorption and luminescence. *Optics Letters*. 1980;**5**(9):368-370

[42] Pala RA, Shimizu KT, Melosh NA, Brongersma ML. A nonvolatile plasmonic switch employing photochromic molecules. *Nano Letters*. 2008;**8**(5):1506-1510

[43] Wiederrecht GP, Wurtz GA, Hranisavljevic J. Coherent coupling of molecular excitons to electronic polarizations of noble metal nanoparticles. *Nano Letters*. 2004;**4**(11):2121-2125

[44] Wurtz GA, Evans PR, Hendren W, Atkinson R, Dickson W, Pollard RJ, et al. Molecular plasmonics with tunable exciton-plasmon coupling strength in J-aggregate hybridized Au nanorod assemblies. *Nano Letters*. 2007;**7**(5):1297-1303

[45] Chevrier K, Benoit J-M, Symonds C, Paparone J, Laverdant J, Bellessa J. Organic exciton in strong coupling with long-range surface plasmons and waveguided modes. *ACS Photonics*. 2018;**5**(1):80-84

[46] Stete F, Koopman W, Bargheer M. Signatures of strong coupling on nanoparticles: Revealing absorption anticrossing by tuning the dielectric environment. *ACS Photonics*. 2017;**4**(7):1669-1676

[47] Cao E, Lin W, Sun M, Liang W, Song Y. Exciton-plasmon coupling interactions: From principle to applications. *Nanophotonics*. 2018;**7**(1):145-167

[48] Haes AJ, Zou S, Zhao J, Schatz GC, Van Duyne RP. Localized surface plasmon resonance spectroscopy near molecular resonances. *Journal of the*

- American Chemical Society. 2006;  
**128**(33):10905-10914
- [49] Zhao J, Das A, Zhang X, Schatz GC, Sligar SG, Van Duyne RP. Resonance surface plasmon spectroscopy: Low molecular weight substrate binding to cytochrome P450. *Journal of the American Chemical Society*. 2006;  
**128**(34):11004-11005
- [50] Ibrahim I, Lim HN, Zawawi RM, Tajudin AA, Ng YH, Guo H, et al. A review on visible-light induced photoelectrochemical sensors based on CdS nanoparticles. *Journal of Materials Chemistry B*. 2018;**6**(28):4551-4568
- [51] El Kabbash M, Rahimi Rashed A, Sreekanth KV, De Luca A, Infusino M, Strangi G. Plasmon-exciton resonant energy transfer: Across scales hybrid systems. *Journal of Nanomaterials*. 2016;  
**2016**:1-21. DOI: 10.1155/2016/4819040
- [52] De Silva AP, Gunaratne HN, Gunnlaugsson T, Huxley AJ, McCoy CP, Rademacher JT, et al. Signaling recognition events with fluorescent sensors and switches. *Chemical Reviews*. 1997;**97**(5):1515-1566
- [53] Krajczewski J, Kołataj K, Kudelski A. Plasmonic nanoparticles in chemical analysis. *RSC Advances*. 2017;**7**(28): 17559-17576
- [54] Navarro JR, Lerouge F. From gold nanoparticles to luminescent nano-objects: Experimental aspects for better gold-chromophore interactions. *Nanophotonics*. 2017;**6**(1):71-92
- [55] Shi J, Tian F, Lyu J, Yang M. Nanoparticle based fluorescence resonance energy transfer (FRET) for biosensing applications. *Journal of Materials Chemistry B*. 2015;**3**(35): 6989-7005
- [56] Rakovich A, Nabiev I, Sukhanova A, Lesnyak V, Gaponik N, Rakovich YP, et al. Large enhancement of nonlinear optical response in a hybrid nanobiomaterial consisting of bacteriorhodopsin and cadmium telluride quantum dots. *ACS Nano*. 2013;  
**7**(3):2154-2160
- [57] Zhang J, Fu Y, Lakowicz JR. Enhanced Förster resonance energy transfer (FRET) on a single metal particle. *The Journal of Physical Chemistry C*. 2007;**111**(1):50-56
- [58] Obeng EM, Dullah EC, Danquah MK, Budiman C, Ongkudon CM. FRET spectroscopy—towards effective biomolecular probing. *Analytical Methods*. 2016;**8**(27): 5323-5337
- [59] Hussain SA. An introduction to fluorescence resonance energy transfer (FRET). arXiv preprint arXiv:09081815. 2009
- [60] Sen T, Patra A. Recent advances in energy transfer processes in gold-nanoparticle-based assemblies. *The Journal of Physical Chemistry C*. 2012;  
**116**(33):17307-17317
- [61] Ray PC, Fan Z, Crouch RA, Sinha SS, Pramanik A. Nanoscopic optical rulers beyond the FRET distance limit: Fundamentals and applications. *Chemical Society Reviews*. 2014;**43**(17): 6370-6404
- [62] Rakshit S, Moulik SP, Bhattacharya SC. Understanding the effect of size and shape of gold nanomaterials on nanometal surface energy transfer. *Journal of Colloid and Interface Science*. 2017;**491**:349-357
- [63] Sahoo H. Förster resonance energy transfer—A spectroscopic nanoruler: Principle and applications. *Journal of*

Photochemistry and Photobiology C:  
Photochemistry Reviews. 2011;**12**(1):  
20-30

[64] Gansen A, Felekyan S,  
Kühnemuth R, Lehmann K, Tóth K,  
Seidel CA, et al. High precision FRET  
studies reveal reversible transitions in  
nucleosomes between microseconds and  
minutes. *Nature Communications*. 2018;  
**9**(1):1-13

[65] Rashed AR, De Luca A, Dhama R,  
Hosseinzadeh A, Infusino M, El  
Kabbash M, et al. Battling absorptive  
losses by plasmon–exciton coupling in  
multimeric nanostructures. *RSC  
Advances*. 2015;**5**(66):53245-53254

[66] Zu F, Yan F, Bai Z, Xu J, Wang Y,  
Huang Y, et al. The quenching of the  
fluorescence of carbon dots: A review on  
mechanisms and applications.  
*Microchimica Acta*. 2017;**184**(7):  
1899-1914

[67] Gambhir K, Ray B, Mehrotra R,  
Sharma P. Morphology dependent two  
photon absorption in plasmonic  
structures and plasmonic–organic  
hybrids. *Optics & Laser Technology*.  
2017;**90**:201-210

[68] Gambhir K, Sharma P, Sharma A,  
Husale S, Mehrotra R. Plasmon  
augmented two photon absorption in a  
strongly coupled nano-molecular hybrid.  
*Dyes and Pigments*. 2018;**155**:313-322

[69] Gambhir K, Sharma P, Sharma C,  
Kumar M, Mehrotra R. Morphology  
induced plasmonic–excitonic interaction  
revealed by pump-probe spectroscopy.  
*Optics & Laser Technology*. 2019;**119**:  
105674





## Chapter 3

# Infrared Nano-Focusing by a Novel Plasmonic Bundt Optenna

*Ehab Awad*

### Abstract

Infrared optical detection devices such as photodetectors, solar cells, cameras, and microbolometers are becoming smaller in size with a tiny active area in the range of a few micrometers or even nanometers. That comes at the expense of a smaller aperture area of the device, and in turn inefficient collection of infrared energy. Therefore, infrared plasmonic optical antennas are becoming essential to efficiently collect optical energy from free space and concentrate it down to the device's tiny area. However, it is desirable to develop plasmonic antennas with a broad bandwidth, polarization insensitivity, wide field-of-view, and reasonable plasmonic losses. That ensures collection of most incident infrared radiation and enhancement of power absorption efficiency. In this chapter, some types of plasmonic antennas are explored with an emphasis on innovative type of optical antenna called Bundt Optenna. We investigate Bundt Optenna design and optimization. This antenna has a novel shape that looks like a Bundt baking pan and it is made of gold. Several Bundt unit cells can be arranged in a periodic array that is placed on top of a thin-film infrared absorbing layer. The Bundt Optenna utilizes surface plasmons to squeeze both electric and magnetic fields of infrared radiation down to a 50 nm wide area, thus enhancing absorption efficiency within an underneath thin-film layer. The Optenna demonstrates polarization insensitivity and ultra-broad bandwidth with a large fractional bandwidth within the near, short-wave, and mid-wave infrared bands. It also shows a remarkable enhanced power absorption efficiency and a wide field-of-view.

**Keywords:** nanophotonics, optical antenna, surface plasmonics, infrared detection, infrared absorption enhancement

### 1. Introduction

Infrared detectors have many types, which can be classified based on their applications and physical response to infrared radiation. Some of them are sensitive to temperature changes due to the thermal effects of infrared radiation, others absorb infrared photons and generate free carriers. Examples of infrared detectors are microbolometers, pyroelectric detectors, cameras, photodetectors, and solar cells [1].

Infrared detectors are becoming ultra-compact in size with tiny active areas in the range of a few micrometers or nanometers. That enhances as well as yields novel

detection characteristics and properties [2]. The tiny size has several advantages. It allows for efficient cooling of the detector, thus reducing thermal noise and allowing good performance at high temperatures. It reduces device capacitance and thus allows for ultrafast optical switching and manipulation of high bitrates data. Also, it permits the collection of almost all photogenerated carriers due to their short path to electrodes, and thus high quantum efficiency. In cameras and sensors, tiny size means aggregating a lot of small-size pixels in a small area, and thus high spatial resolution imaging and the possibility of ultra-dense integration.

Downsizing the detection devices area comes at the expense of the smaller aperture area, and in turn inefficient collection of infrared radiation energy. The solution to such a problem is to utilize infrared plasmonic optical antennas in front of the detectors. The optical antennas can collect optical energy efficiently from free space to focus it on small size devices [3–8]. The plasmonic focusing of electric fields into sub-wavelength nano hot spots increases the atoms absorption cross-section areas within detection material (e.g. thin-film) and in turn the materials absorption coefficient [8–19].

The optical antenna design should have some characteristics for getting the best performance. In other words, it should have a special shape, different stages, and optimum dimensions. The shape should be selected to have a large aperture that collects infrared energy from all over the free space and focuses it down to a sub-wavelength nanoscale area. One aspect of that is to minimize the back-reflections of optical energy at the antenna input. That can be done by matching the antenna input optical impedance to that of free-space, in addition to optical impedances among different stages of the antenna. That of course imposes a lot of constraints on antenna dimensions. Talking about optical impedance, we mean the wave nature of light that allows us to treat light as an electromagnetic wave with ultra-high frequency traveling in a medium with impedance.

The antenna should also have a special shape that allows it to be polarization-insensitive. In that way, it can collect infrared energy from different incident polarizations, which is useful, especially for solar cells and energy harvesting applications. However, it is worth mentioning that in some other applications like infrared cameras, for example, polarization-dependent (i.e. polarimetric) detection can be useful to distinguish between different features in a scene [20].

In addition, the plasmonic antenna should have an overall small size to minimize ohmic power losses associated with surface plasmon polaritons (SPP) traveling waves on antenna metal surfaces [21]. Moreover, the optical antenna should have a broad bandwidth. Thus, it can collect as much energy as possible within a specific wavelength band, and in turn, its average response over such particular bandwidth is maximized. Also, the optical antenna should have a wide field of view to collect as much radiation as possible from all angles of view.

It is worth mentioning that optical antennas are not solely useful in infrared detection applications. Optical nanoantennas can be also useful in detection applications within the visible range. For example, it can be used in energy harvesting and solar cells [22–24].

In the following sections, some examples of optical infrared antennas will be presented. In Section 2, a brief overview of some optical antenna examples will be discussed. In Section 3, a novel design of a plasmonic Bundt optical antenna will be presented and discussed. In Section 4, the performance of the Bundt optical antenna will be evaluated. Finally, a conclusion section will summarize the important points discussed in this chapter.

## 2. Examples of optical infrared antennas

There are various types of optical antennas that have been known so far. To name some, a half-wave dipole optical antenna can concentrate infrared onto nanometer germanium photodiode. This optical antenna is polarization sensitive. It covers a bandwidth of 1.34 to 1.48  $\mu\text{m}$  and it shows a factor of 20 enhancement in detector response [8]. Another example is a silicon plasmonic horn that has periodic grooves on its surface. It has a short length and gives a maximum coupling efficiency of 27% within the wavelength range of 1538 to 1562 nm [9]. A silver nano-array of coaxial rings shows extraordinary transmission with almost a factor of 4 enhancement in transmitted optical intensity [10]. A hybrid silicon-gold nano-particles optical antenna is also demonstrated with multipole resonance. It covers all the visible wavelength range and can enhance optical absorption by a factor of 2.5 [11]. A plasmonic spiral ring grating could be coupled to a vertical nano-optical antenna to enhance optical field intensity by up to 7 orders of magnitude. The simulated collection efficiency can reach up to 68% [12]. A dielectric silicon nanoantenna is demonstrated with an ultra-low optical power loss and heating conversion. It covers the near-infrared band and can enhance surface fluorescence by about 3 orders of magnitude [13]. A trench thin metal polarization-insensitive antenna is demonstrated. It is polarization insensitive with high responsivity at tele-communication infrared wavelengths [14]. A nanoantenna sandwiched between two graphene monolayers photo-detector is demonstrated. It covers both visible and infrared bands with 8 times enhancement in detection response and up to 20% internal quantum efficiency [15].

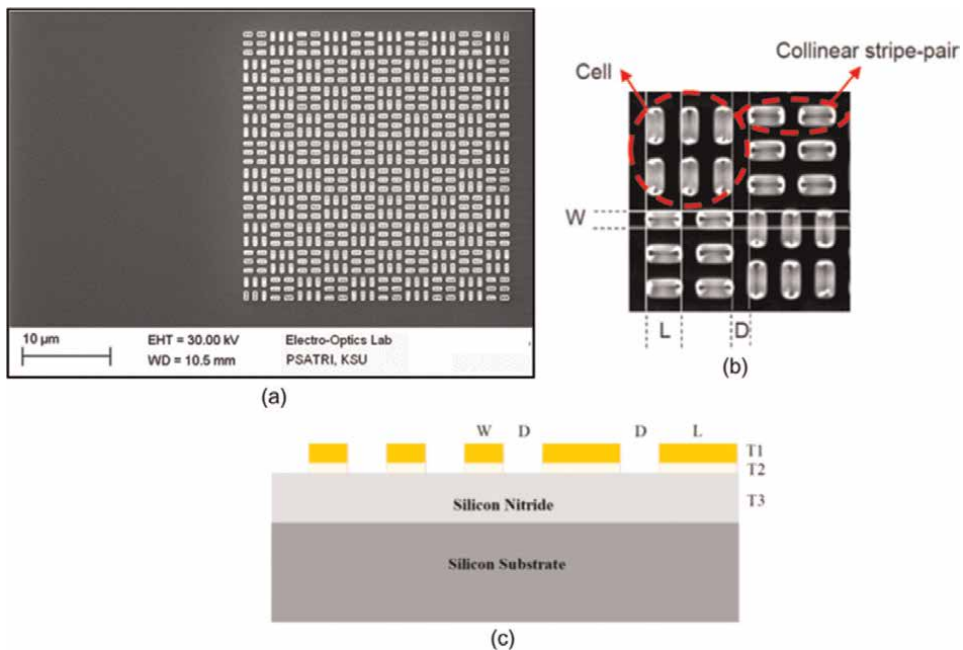


**Figure 1.** The checkerboard optical antenna detection device. (a) the SEM image of the fabricated checkerboard device sample ( $30 \times 30 \mu\text{m}^2$ ). (b) Magnified SEM image of four cross-oriented unit cells,  $L = 1049 \text{ nm}$ ,  $D = 530 \text{ nm}$ ,  $W = 510 \text{ nm}$ . (c) a schematic cross-section in detection device,  $L = 1000 \text{ nm}$ ,  $W = 500 \text{ nm}$ ,  $D = 500 \text{ nm}$ ,  $T_1$  (gold) =  $50 \text{ nm}$ ,  $T_2$  (titanium) =  $10 \text{ nm}$ ,  $T_3$  ( $\text{Si}_3\text{N}_4$ ) =  $400 \text{ nm}$  [16].

In the following subsections, structures of some types of optical antennas are explored and examined in detail.

## 2.1 Checkerboard optical antenna

The gold checkerboard antenna consists of nanoscale dipole antennas [16, 17]. **Figure 1a** and **b** show scanning electron microscope (SEM) images of such checkerboard structure. It consists of subwavelength gold stripes arranged in cross-oriented unit cells. The stripes are separated by subwavelength gaps. Each stripe acts like a dipole antenna that can receive long infrared radiation (8-12  $\mu\text{m}$ ). The gold stripes interact with incident light electromagnetic waves resulting in collective electrons oscillations (plasmons) in direction of light polarization (i.e. forming dipoles). The oscillating electrons accumulate at the stripes' edges resulting in a very high electric field with spatial nano-resolution [21]. These localized surface plasmons are coupled together within the gaps among stripes, thus creating what is called hot spots. These hot spots have very high concentrated infrared optical intensities. Thus, it can increase the optical absorption within the underneath absorbing layer of silicon

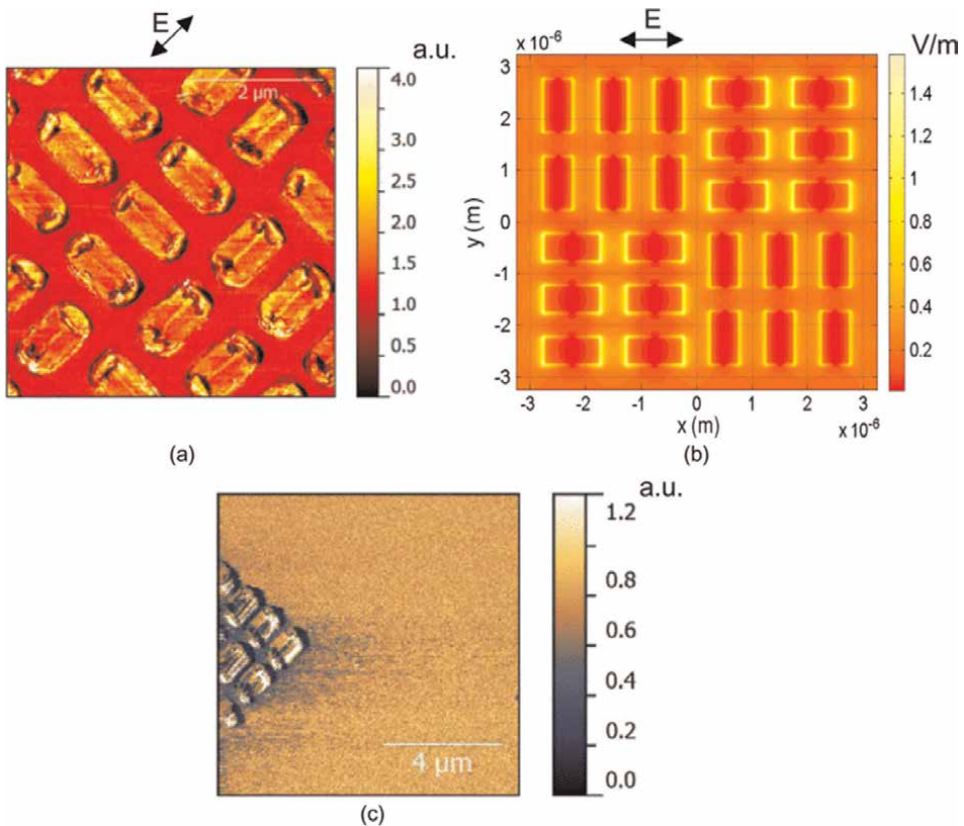


**Figure 2.** (a) The SNOM image of the scattered electric field ( $E$ ), in arbitrary units, from the checkerboard sample (rotated) at a  $10.19 \mu\text{m}$  wavelength. (b) the FDTD simulation of scattered electric field magnitude under the same SNOM measurement conditions in part (a). (c) a comparison of the SNOM scattered electric field magnitudes with/without checkerboard on the same sample at  $10.6 \mu\text{m}$  wavelength [16].

nitride ( $\text{Si}_3\text{N}_4$ ) and in turn the detection efficiency. The detection device layers structure is shown in **Figure 1c**.

**Figure 2a** and **c** show images of scattered electric fields from the checkerboard antenna taken by scanning near-field optical microscope (SNOM) at a wavelength of  $10.19\ \mu\text{m}$ . **Figure 2b** shows a corresponding image to that of **Figure 2a**, simulated using a three-dimensional finite-difference time-domain (FDTD) method. As seen in **Figure 2c**, there is a dark area underneath the checkerboard structure. This darkness indicates enhanced absorption within the silicon nitride thin-film layer.

The tested checkerboard antenna shows broadband and polarization-independent average absorption enhancement of 63.2% over the wavelength range  $8\text{--}12\ \mu\text{m}$ . Also, it shows a maximum absorption enhancement of 107% at  $8\ \mu\text{m}$  wavelength and a minimum enhancement of 24.8% at  $12\ \mu\text{m}$  wavelength.

## 2.2 Dipole nanoantenna coupled to plasmonic slot waveguide

Another example of optical antennas is the dipole coupled to a plasmonic slot waveguide [18]. The dipole antenna is made of gold and has a bottom and side reflectors that can increase its coupling efficiency up to 26% at a wavelength of  $1550\ \text{nm}$ . The coupling efficiency is defined as the ratio of power delivered to the waveguide to incident power on the dipole antenna. In this configuration the dipole antenna is irradiated by a vertical optical fiber terminated by a focusing lens, see **Figure 3a**.

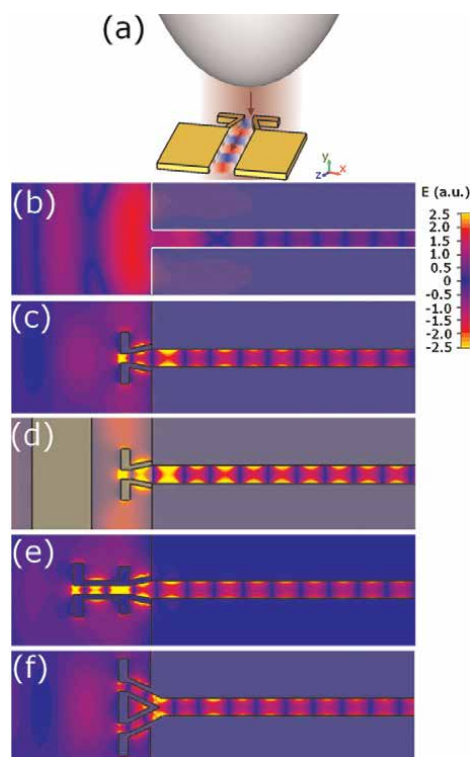


**Figure 3.** (a) Antenna working in vertical coupling configuration. The beam from the fiber excites slot plasmons. Instant images of the simulated electric field ( $E$ ) in arbitrary units at  $\lambda = 1.55\ \mu\text{m}$  when coupling to (b) waveguide only, (c) single antenna, (d) antenna with side and bottom reflectors, (e) serial, and (f) parallel antenna array. The color scale is equal for (b) through (f). Reprinted with permission from [ref 18] © the Optical Society.

The antenna collects fiber radiation and launches it inside an impedance-matched slot waveguide. The dipole antenna length is adjusted to be an integer number of half-wavelengths. Also, the side and bottom reflectors are positioned such that it forms a maximum of standing wave reflections at the antenna position. **Figure 3** shows different configurations of the tested system together with images of simulated electric fields. As seen, the coupled electric field magnitudes increase from **Figure 3a–d** here the coupling efficiency becomes maximum. The system is also tested with serial and parallel dipole arrays as shown in **Figure 3e** and **f**, respectively. However, these two configurations give the same performance as a single dipole antenna with side and bottom reflectors.

This dipole nanoantenna shows 185 times enhancement in coupling efficiency when compared to a bare waveguide. It can be utilized as an interface coupler between an optical fiber and a plasmonic slot waveguide.

### 2.3 Horn optical nanoantenna

An additional example of optical antennas is a two-dimensional plasmonic horn nanoantenna made of silver. This antenna is impedance matched to a plasmonic slot feeding transmission line [19]. It has a broad bandwidth (1260–1675 nm) for applications in wireless on-chip communications. It is investigated by FDTD simulations as shown in **Figure 4**. In **Figure 4a, d** and **g**, the horn length and its flare angle should be

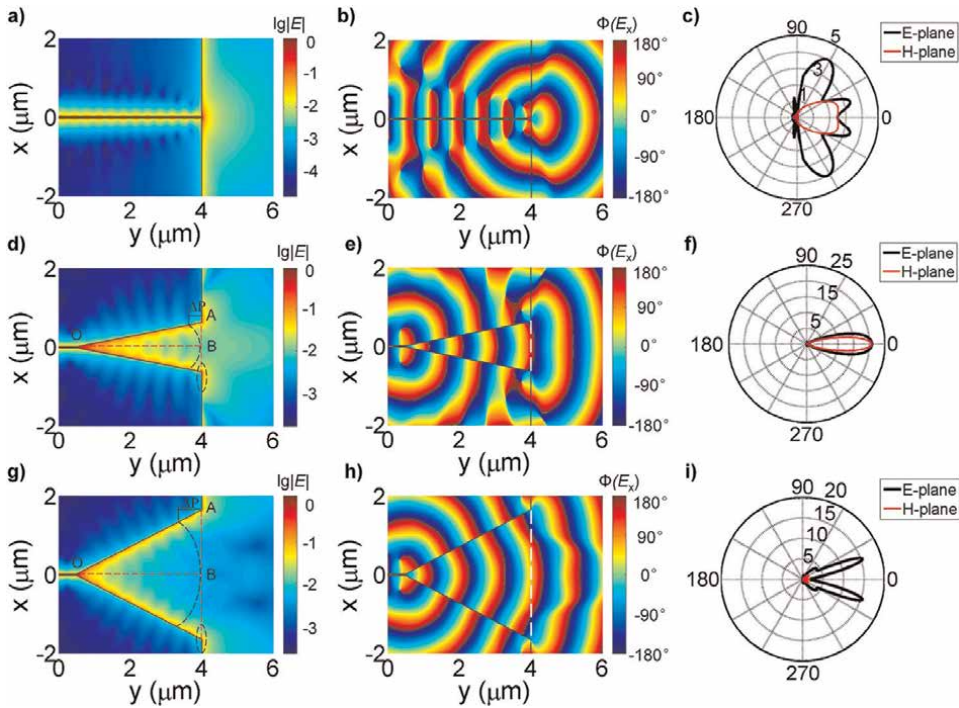


**Figure 4.** Near-field profiles and far-field radiation patterns of a bare waveguide and horn nanoantennas with different flare angles. (a–c) Bare waveguide case. The amplitude (a), phase (b) of electric field distribution, and radiation pattern (c) of a bare waveguide. (d–f) a horn nanoantenna with a length ( $L_a$ ) of  $3.5 \mu\text{m}$  and flare angle ( $\theta$ ) of  $10^\circ$ . The amplitude (d), phase (e) of electric field distribution, and radiation pattern (f). (g–i) a horn nanoantenna with  $L_a = 3.5 \mu\text{m}$  and  $\theta = 25^\circ$ . The amplitude (g), phase (h) of electric field distribution, and radiation pattern (i) [19].

carefully designed to minimize back reflections at the horn input. The corresponding wavefront phase distributions are shown in **Figure 4b, e, and h**. In **Figure 4c, f, and i**, the far-field radiation patterns are shown for each case. The best design is found to be the case in **Figure 4d–f**, where the back-reflected field magnitude is minimized, the phase front looks like a plane-wave, and thus it is matched to that of free-space radiation, in addition, the radiation pattern is highly directional. This optical antenna can give a superior performance with almost 100-fold enhancement in power transfer when compared to conventional dipole nanoantennas.

It is worth mentioning that an optical antenna design should take into consideration some points that allow it to have better performance characteristics when compared to the previous designs. For example, it should have a special shape with a large aperture to collect infrared energy from all free-space and focuses it on a nanoscale area. Also, back-reflections of antenna optical energy should be minimized by matching antenna input optical impedance to that of free-space. That of course imposes a lot of design constraints on the optical antenna dimensions. It is also better to have a polarization-insensitive antenna to collect all infrared energy at different polarizations. In addition, a plasmonic optical antenna should be small enough to minimize the surface plasmon polaritons' ohmic power losses. It is also desirable to have a broadband antenna optical response. Moreover, an optical antenna should have a wide field of view to collect optical energy from all over free-space angles.

In the following sections, we will explore in detail a novel optical antenna called Bundt Optenna that realizes these design constraints and thus possess several advantages.

### 3. Bundt plasmonic antenna

Now we are going to examine a novel optical antenna design that is called Bundt Optenna [25, 26]. Here, the optical antenna is abbreviated as “Optenna” and has a unique shape that looks like a Bundt baking pan. The Bundt Optenna has been featured by scientific media as promising for nanoscale infrared detection devices such as solar cells, telecommunications photodetectors, shortwave cameras, and mid-wave microbolometers [27]. In addition, it can keep plasmonic losses to a minimum while focusing infrared radiation to nanoscale size, thus doing the trick [28].

This Bundt Optenna has many desirable advantages. It has an ultra-broadband optical response covering the near, shortwave, and mid-wave infrared bands with high fractional bandwidth up to 42%. It is polarization insensitive with a wide field of view. It can squeeze both electric and magnetic fields down to 50 nm spot area to enhance optical absorption efficiency within a thin-film detection layer. The power absorption enhancement can reach up to 8 orders of magnitude (i.e. 80 dB). Moreover, it has a compact size with potential applications in energy harvesting, optical communications, and biomedical technology.

**Figure 5** shows a schematic diagram of the Bundt Optenna structure with different cross-sections. It has a gold concentric structure that is filled with air as a dielectric material. The Optenna is built on top of a semiconductor thin-film detection layer above a thick bulk substrate. **Figure 5a** shows a two-dimensional periodic array of the Bundt unit-cells with a periodic separation of “L”. A vertical cross-section in a single unit cell is shown in **Figure 5b**. It shows three stages. The first stage consists of a

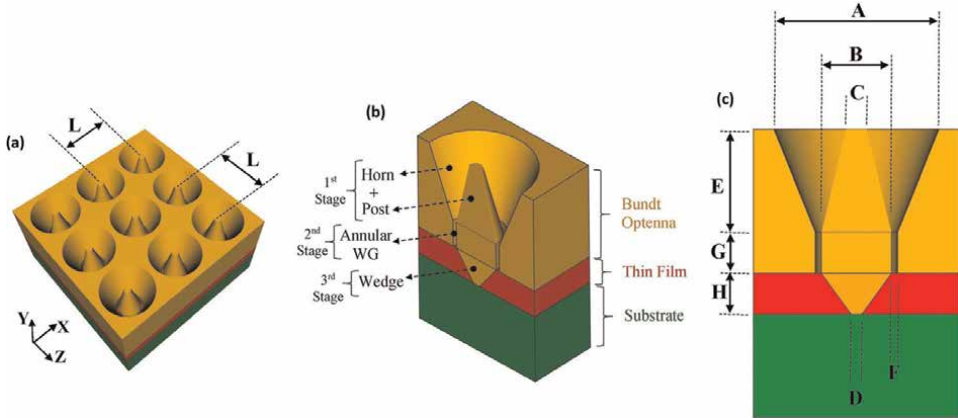


**Figure 5.** The schematic diagram of the proposed infrared detection device with Bundt Optenna. (a) a perspective view of 2D periodic Bundt array, (b) a vertical cross-section of unit-cell indicating different stages and the underneath semiconductor layers, (c) a vertical cross-section of unit-cell indicating different dimensions [25].

coaxial (concentric) conical horn and a middle post. The conical concentric shape allows the Optenna to easily impedance match surrounding free-space, and collect most of the incident radiation due to its relatively large input aperture. In addition, this shape allows for polarization-insensitive operation because of its symmetry around the central axis. The second stage is an annular gold waveguide that matches the optical impedance between the first stage and the third stage. The third stage is a conical gold wedge extending through the thin-film detection layer. It allows the excited SPP to penetrate deep inside the absorbing layer thus increasing the overall absorption area inside the thin-film. **Figure 5c** labels different dimensions on the cross-section of a single unit cell.

The incident free-space infrared radiation is collected by the Bundt array's large aperture. The coaxial horn and post with air-filling dielectric act like a metal-insulator-metal (MIM) waveguide that has a conical flare. This waveguide is end-fire excited by incident free-space radiation and generates SPP on the antenna gold surfaces forming a  $TE_{11}$  mode [29] that propagates along the MIM waveguide. Both the plasmonic electric and magnetic fields are squeezed gradually during propagation until they reach a sub-wavelength nano wide ( $F = 50$  nm) annular area at the first stage output. This area can be found by the following equation:

$$\text{Area} = \pi \times \left[ \left( \frac{B}{2} + F \right)^2 \right] - \left( \frac{B}{2} \right)^2 \quad (1)$$

The "A", "B", "C", and "E" are the dimensions of Bundt's first stage. They are optimized to allow optical-impedance matching between free-space and Bundt coaxial horn. This means the optical back-reflections are minimized, and in turn forward propagating transmitted signals are maximized. An annular waveguide with a width "F" and length "G" that is filled with air is used as an intermediate second stage. Which matches the optical impedance between the antenna's first stage and third stage (absorbing thin-film). The annular waveguide is an extension of the flared coaxial horn with  $TE_{11}$  propagating squeezed mode. The annular waveguide has multiple reflections between its input and output like a Fabry-Perot resonator. Therefore,



the waveguide length “G” is chosen to make the round-trip phase-shift ( $\Delta\varphi$ ) equal to “ $m\pi$ ”. This condition can be written as:

$$\Delta\varphi = 2 \times G \times K + \delta\varphi = m \times \pi \quad (2)$$

The “ $\delta\varphi$ ” is the reflections phase-shift at waveguide input and output, “k” is the propagation constant, and “m” is an integer number. This condition results in constructive interference at waveguide output, and destructive interference of back-reflected waves at waveguide input.

The third stage of the Bundt Optenna is a conical gold wedge of length “H”, besides the Bundt base on top of the thin-film layer. The third stage acts like a flared MIM waveguide that is excited by the SPP out of the annular waveguide. This SPP spreads inside the absorbing thin-film layer. Therefore, the third stage allows excited SPP to penetrate and spread deep inside the thin-film, thus increasing the overall absorption area of the absorbing layer.

The Bundt Optenna array was designed and simulated over different infrared bands. That includes near-infrared (NIR), short-wave infrared (SWIR), and mid-wave infrared (MWIR) wavelengths bands. The dimensions of different Bundt stages are optimized during numerical simulations to get the best optical impedance matching. That means minimizing back reflections and maximizing transmission to obtain an almost flat response. We obtain four designs of the Bundt Optenna. Each design has specific dimensions. **Table 1** summarizes the dimensions of each design. It is found that there are some rules which should be satisfied in all these designs. The coaxial horn length “E” should be greater than the maximum wavelength of each design range. That is to ensure having one electric-field cycle along the horn length. Also, the inner perimeter of the annular waveguide (i.e.  $\pi \times B$ ) should be greater or equal to the maximum wavelength of the corresponding range. That ensures the magnetic field one period around the waveguide perimeter is not smaller than the maximum wavelength of TE<sub>11</sub> mode. To minimize ohmic loss of SPP, the “E” dimension and ( $\pi \times B$ ) are selected to be equal to the maximum wavelength. The dimension “A” is chosen to maintain a symmetric coaxial horn. The dimensions “C”, “D”, “G”, and “L” are chosen by numerical iterations to minimize back-reflections. The largest Bundt unit-cell 3.25x3.25x6.8  $\mu\text{m}^3$  is for the MWIR design. While the largest unit-cell aspect ratio 3.6:1 is for the NIR design. The Bundt has an overall compact size with a reasonable aspect ratio. The Optenna designs “1”, “2”, “3”, and “4” are useful in applications such as solar cells, optical communications photodetectors, SWIR sensors/ cameras, and MWIR thermal detection/ imaging with microbolometers, respectively.

Band	Range ( $\mu\text{m}$ )	Design	A	B	C	D	E	G	L
NIR	0.74–1	1	0.6	0.32	0.05	0.125	1	0.5	0.625
SWIR	1–2	2	1.4	0.7	0.05	0.25	2	1	1.425
		3	2	1	0.1	0.35	3	0.5	2.025
MWIR	3–5	4	3.2	1.6	0.2	0.55	5	1	3.25

*The assigned dimensions’ are already indicated in Figure 1, and they are measured in “ $\mu\text{m}$ ”. The dimensions  $H = 0.7 \mu\text{m}$  and  $F = 50 \text{ nm}$  are fixed for all the designs [25].*

**Table 1.**  
 The four designs of Bundt Optenna that can cover the three infrared bands.

#### 4. Bundt plasmonic Optenna performance

The Bundt Optenna performance is evaluated using three-dimensional FDTD. The thin-film layer is selected to be silicon nitride as an example, with a silicon substrate. **Figure 6** shows the normalized magnitudes of the electric (magnetic) fields of one unit cell. The wavelength is selected here to be  $2.3 \mu\text{m}$  with TM linear polarization along the x-direction. **Figure 6a** shows a vertical cross-section of a unit-cell (X-Y plane) at  $Z = 0$ . As shown, the SPP electric-fields inside the concentric horn are concentrated around the post as it has a small apex angle. The highest electric-field intensity is found to be within the  $50 \text{ nm}$  wide annular waveguide. Inside the thin-film layer, the high-intensity field propagates and spreads with more SPP concentration around the wedge and Bundt base. This high-intensity field is absorbed and exponentially attenuated within the thin-film layer. It almost vanishes within the underneath silicon substrate. The back-reflected electric-field is very small. A supplementary Video 1 (<https://bit.ly/3t8Bundt>) illustrates the electric-field propagating at  $2.3 \mu\text{m}$  wavelength inside the Bundt Optenna.

**Figure 6b–d** illustrate the electric-field at cross-sections X-Z at Bundt annular waveguide input and output, respectively. They show the  $\text{TE}_{11}$  squeezing down to  $50 \text{ nm}$  wide annular area at the thin-film layer. **Figure 6–b** shows the  $\text{TE}_{11}$  mode normalized electric-field at concentric horn input. **Figure 6c** shows the squeezed  $\text{TE}_{11}$  plasmonic electric-field at the annular waveguide input. The maximum normalized electric-field is 8 at the annular waveguide. Which is almost eight times enhancement in the field strength (i.e. 18 dB). **Figure 6e** illustrates the squeezed magnetic  $\text{TE}_{11}$

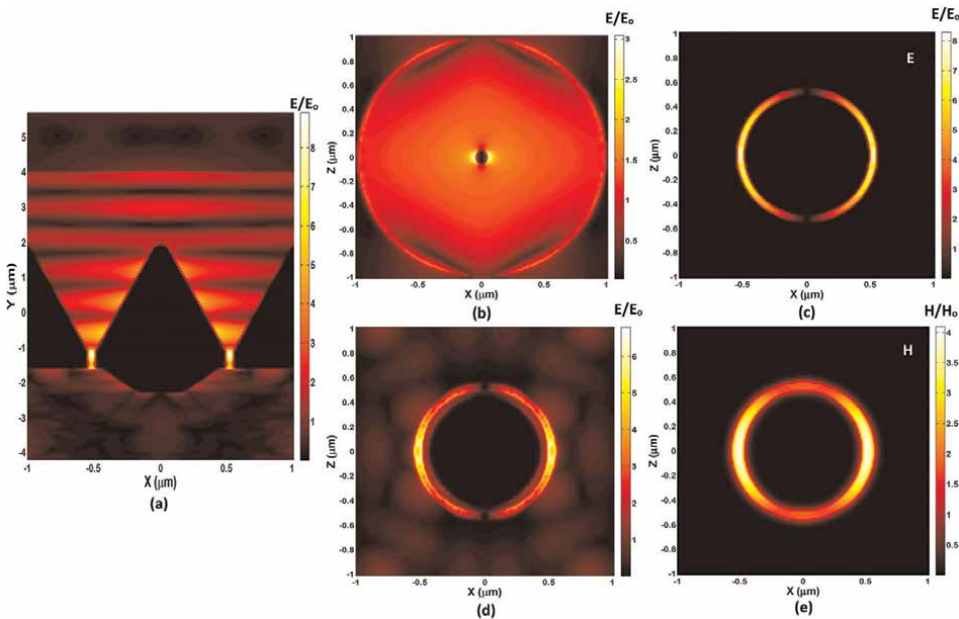


**Figure 6.** The three-dimensional FDTD simulations fields (normalized) within a unit-cell of infrared detection device at a wavelength of  $2.3 \mu\text{m}$ , and TM incident polarization. The normalized electric-field magnitude ( $E/E_0$ ): (a) a vertical cross-section in a unit-cell, (b) a horizontal cross-section at the input of concentric horn, (c) a horizontal cross-section at the input of annular waveguide, (d) a horizontal cross-section just outside the annular waveguide (i.e. at the entrance of the thin-film layer). The normalized magnetic-field magnitude ( $H/H_0$ ): (e) a horizontal cross-section at the input of the annular waveguide [25].

plasmonic -field magnitude at the annular waveguide input. It has a maximum of 4, which indicates  $\cong 12$  dB improvement in the field strength. **Figure 6d** shows the nano-focused electric-field at the entrance of the thin-film layer, where the electric-field strength starts to attenuate by optical absorption.

**Figure 7** illustrates the coupling ratio (CR) of TM-polarization in each Bundt Optenna stage versus wavelength. Figures (a), (b), (c), and (d) correspond to designs “1”, “2”, “3”, and “4”, respectively. The CR is defined as the ratio of transmitted power at each stage to input power. The CR into stage “1” is considerably high for all designs. However, it does not reach zero dB due to small back-reflections into free-space. The back-reflections are estimated to be less than  $-7$  dB. The CR within the third stage shows a high collection efficiency of the Optenna. The CR of the second and third stages is less than the first stage due to SPP ohmic power loss on gold surfaces. The 3 dB bandwidth (BW) of Bundt Optenna is measured at Optenna third stage because it is the transferred power by the optenna to thin-film layer. The small ripples on curves are due to the Fabry-Perot effect at different interfaces of Optenna stages. **Table 2** shows the bandwidth for each Bundt design together with its center-wavelength ( $\lambda_o$ ) and calculated optical fractional bandwidth (O-FBW). The O-FBW is the ratio of bandwidth to center-wavelength (i.e.  $BW/\lambda_o$ ). The table shows a broadband optical response with a high optical fractional bandwidth  $\cong 35\%$  up to  $42\%$ .

It is worth noting the following issues regarding the Bundt Optenna performance. The field squeezing results in a dramatic reduction in its cross-section area, which

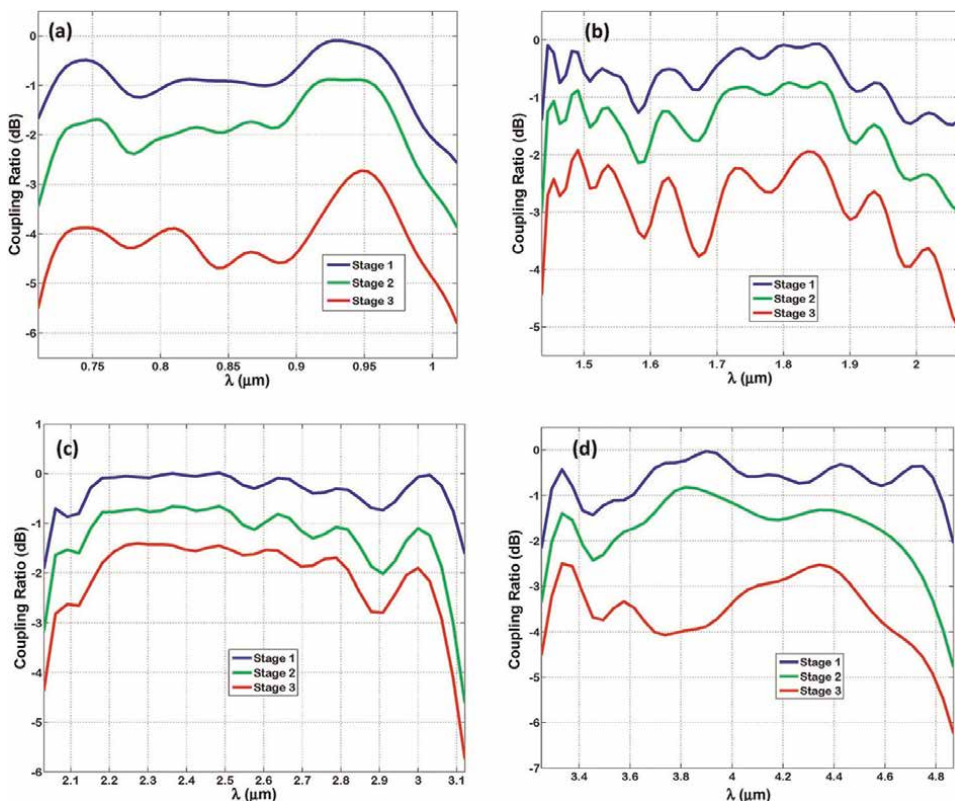


**Figure 7.** The coupling ratio estimated in decibels of TM-polarized infrared radiation at successive stages of Bundt Optenna: (a) design “1”, (b) design “2”, (c) design “3”, (d) design “4” [25].

Band	Design	Wavelength ( $\mu\text{m}$ )	BW ( $\mu\text{m}$ )	$\lambda_o$ ( $\mu\text{m}$ )	O-FBW (%)
NIR	1	0.71–1.01	0.3	0.86	34.9
SWIR	2	1.43–2.06	0.63	1.75	36
	3	2.03–3.12	1.1	2.58	42.6
MWIR	4	3.25–4.86	1.61	4.06	39.7

In addition to the percentages of optical fractional bandwidth (O-FBW) [25].

**Table 2.**

The wavelength range, bandwidth (BW), and center-wavelength ( $\lambda_o$ ) of different Bundt designs, measured in micrometer ( $\mu\text{m}$ ).

means a high gain in optical intensity despite power attenuation by SPP ohmic losses. The intensity is defined as the optical power divided by area. The nano-focused fields' intensity increases the effective absorption cross-section area of material atoms, and thus the materials absorption coefficient. Therefore, the thin-film absorption efficiency is expected to increase because of Bundt's high intensity that reaches, for example, 12.4 dB at the wavelength of 3.3  $\mu\text{m}$ . The average ohmic losses on gold surfaces due to SPP are found to be almost -3 dB, which is considered reasonable. The different Bundt designs are found to be polarization insensitive over different tested bands. That is due to the two-dimensional symmetry of the Bundt structure. Therefore, the Bundt optical response is always the same for all types of incident polarizations. That is advantageous as Optenna can collect most of the incident radiation power regardless of its polarization. Moreover, the Bundt field of view is measured by varying radiation incidence angles while monitoring the output intensity. For all the designs, the maximum incidence angle is found to be  $\cong 40^\circ$ , indicating a Bundt Optenna field-of-view  $\cong 2 \times 40^\circ \cong 80^\circ$ .

**Figure 8** illustrates the absorption enhancement factor (EF) inside the thin-film layer. It is defined as the ratio between thin-film absorbed power in the case with and without Bundt Optenna. It is measured in linear scale and decibels as well. The absorption EF is high and reaches a maximum of  $\cong 8.5$ , 29, 80, and 15 dB for designs "1", "2", "3", and "4", respectively. The smallest EF is  $\cong 2$  dB at the band edges. The high EF of designs "2" and "3" are because of the very small attenuation coefficients of a silicon nitride material. Thus, the power absorption EF becomes significant due to Optenna. It can reach as high as  $\cong 80$  dB at a wavelength of  $\cong 2.2 \mu\text{m}$ . The ripples on some curves are because of the Fabry-Perot effect due to residual multiple reflections among Optenna different stages. The enhanced absorption efficiency of the thin film layer is mainly due to the improved material absorption coefficient as the incident optical field intensities become much higher.

## 5. Conclusions

In this chapter, we have explored some types of plasmonic optical antennas that can focus optical infrared radiation to very small spot areas beyond the light diffraction limit. These antennas are essential for infrared optical detection devices that have tiny active areas in the range of a few micrometers or even nanometers. In addition, we have focused on one innovative type of optical antenna called Bundt Optenna. We investigated its design and optimization. The Bundt Optenna bandwidth covers the near-infrared, short-wave, and mid-wave infrared bands. The Bundt has a wide

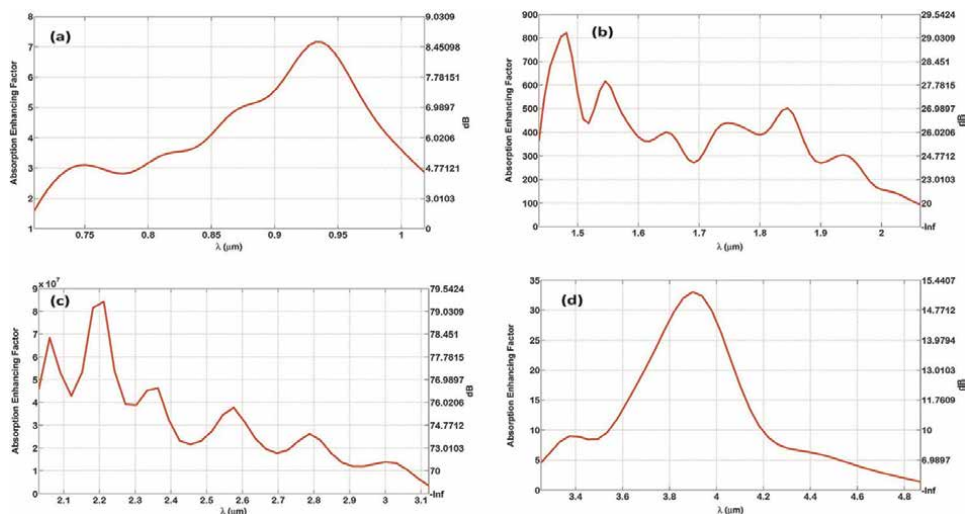


**Figure 8.** The Bundt Optenna absorption enhancement factor inside the thin-film layer indicated in linear scale on the left axis, and in decibels on the right axis: (a) design “1”, (b) design “2”, (c) design “3”, (d) design “4” [25].

field-of-view equal to 80°. It has an ultra-broadband optical response and fractional bandwidth of up to 42%. It can nano-focus electric and magnetic fields to a 50 nm-wide area, and thus enhance the optical absorption efficiency of the thin-film detection layer. The fields’ intensity gain can reach up to 12.4 dB. The power absorption enhancement can be 8 orders of magnitude (i.e. 80 dB). The average ohmic power loss in Bundt Optenna is as low as −3 dB. The Optenna is polarization-insensitive and has a relatively compact size. The Bundt Optenna can be used in different nanoscale detection devices such as photodetectors, solar cells, cameras, and microbolometers, with potential applications in optical communications, imaging, energy harvesting, optical sensors, and biomedical technology.

## Video materials

Video 1 available from <https://bit.ly/3t8Bundt>

## Author details

Ehab Awad  
 Electrical Engineering Department, College of Engineering, King Saud University,  
 Riyadh, Saudi Arabia

\*Address all correspondence to: [esawad@ieee.org](mailto:esawad@ieee.org)

## IntechOpen

© 2022 The Author(s). Licensee IntechOpen. This chapter is distributed under the terms of the Creative Commons Attribution License (<http://creativecommons.org/licenses/by/3.0>), which permits unrestricted use, distribution, and reproduction in any medium, provided the original work is properly cited.

## References

- [1] Rogalski A. Infrared detectors: Status and trends. *Progress in Quantum Electronics*. 2003;27(2):59-210
- [2] Jaksic Z. *Micro and Nanophotonics for Semiconductor Infrared Detectors: Towards an Ultimate Uncooled Device*. Berlin Heidelberg: Academic minds Springer-Verlag; 2014
- [3] Schuller JA, Barnard ES, Cai W, Jun YC, White JS, Brongersma ML. Plasmonics for extreme light concentration and manipulation. *Nature Materials*. 2010;9(3):193-204
- [4] Bharadwaj P, Deutsch B, Novotny L. Optical antennas. *Advances in Optics and Photonics*. 2009;1(3):438-483
- [5] Atwater HA, Polman A. Plasmonics for improved photovoltaic devices. *Nature Materials*. 2010;9(2):205-213
- [6] Novotny L, van Hulst N. Antennas for light. *Nature Photonics*. 2011;5(2):83-90
- [7] Bonakdar A, Mohsenim H. Impact of optical antennas on active optoelectronic devices. *Nanoscale*. 2014;6(19):10961-10974
- [8] Tang L, Kocabas SE, Latif S, Okyay AK, Ly-Gagnon D-S, Saraswat KC, et al. Nanometre-scale germanium photodetector enhanced by a near-infrared dipole antenna. *Nature Photonics*. 2008;2(4):226-229
- [9] Thomas R, Ikonik Z, Kelsall RW. Silicon-based plasmonic coupler. *Optics Express*. 2012;20(19):21520-21531
- [10] Orbons SM, Roberts A, Jamieson DN, Haftel MI, Schlockermann C, Freeman D, et al. Extraordinary optical transmission with coaxial apertures. *Applied Physics Letters*. 2007;90(25):251107
- [11] Kucherik A, Kutrovskaya S, Osipov A, Gerke M, Chestnov I, Arakelian S, et al. Nano-antennas based on silicon-gold nanostructures. *Scientific Reports*. 2019;9(1):338
- [12] Liu B, Wang D, Shi C, Crozier KB, Yang T. Vertical optical antennas integrated with spiral ring gratings for large local electric field enhancement and directional radiation. *Optics Express*. 2011;19(11):10049-10056
- [13] Caldarola M, Albella P, Cortes E, Rahmani M, Roschuk T, Grinblat G, et al. Nano-plasmonic nanoantennas for surface enhanced spectroscopies with ultra-low heat conversion. *Nature Communications*. 2015;6:7915
- [14] Lin KT, Chen HL, Lai YS, Yu CC. Silicon-based broadband antenna for high responsivity and polarization-insensitive photodetection at telecommunication wavelengths. *Nature Communications*. 2014;5:3288
- [15] Fang Z, Liu Z, Wang Y, Ajayan PM, Nordlander P, Halas NJ. Graphene-antenna sandwich photodetector. *Nano Letters*. 2012;12(7):3808-3813
- [16] Awad E, Abdel-Rahman M, Zia MF. Checkerboard nanoplasmonic gold structure for long-wave infrared absorption enhancement. *IEEE Photonics Journal*. 2014;6(4):1-7
- [17] Awad E., Abdul-Rahman M. Optical plasmonic absorber for long-wave infrared radiation. US patent 9128230-B1 2015; United States patent and trademark office

- [18] Andryieuski A, Malureanu R, Biagi G, Holmgaard T, Lavrinenko A. Compact dipole nanoantenna coupler to plasmonic slot waveguide. *Optics Letters*. 2012;**37**(6):1124-1126
- [19] Yang Y, Li Q, Qiu M. Broadband nanophotonic wireless links and networks using on-chip integrated plasmonic antennas. *Scientific Reports*. 2016;**6**:19490
- [20] Awad E, Abdel-Rahman M. Nano-plasmonic chirped metal-strips polarimeter for dual-band infrared detection. *Electronics Letters*. 2017; **53**(2):95-96
- [21] Maier SA. *Plasmonics: Fundamentals and Applications*. New York, USA: Springer-Verlag; 2007
- [22] Obayya S et al. Optical nano-antennas for energy harvesting. In: *Renewable and Alternative Energy: Concepts, Methodologies, Tools, and applications*. Information Resources Management Association. Pennsylvania, United States of America: IGI Global; 2017 chapter 2
- [23] El-Toukhy YM et al. Tapered Plasmonic Nanoantennas For Energy Harvesting Applications. London, United Kingdom: InTechOpen; 2017 chapter 13
- [24] Hussein M et al. Recent Trends in Plasmonic Nanowire Solar Cells. London, United Kingdom: InTechOpen; 2017 chapter 10
- [25] Awad E. Nano-plasmonic Bundt Optenna for broadband polarization-insensitive and enhanced infrared detection. *Scientific Reports*. 2019;**9**(1): 12197
- [26] Awad E. Plasmonic Infrared Optical antenna. US patent 10768363-B1 2020, United States patent and trademark office
- [27] Overton G. Optical Antennas: Bundt-pan-shaped optenna demonstrates 80 dB infrared concentration. *Laser Focus World Magazine (Photonics Technologies & Solutions for Technical Professionals Worldwide)*. 2019;**55**(10):19-20
- [28] Wills S. The Twists and Turns of Plasmonic Antenna Design. *Optics and Photonics News (OPN) magazine*, OSA publication. 2019;**51**(11):14
- [29] Pozar DM. *Microwave Engineering*. 4th ed. New Jersey, United States of America: John Wiley & Sons Inc.; 2012





---

Section 2

Plasmonic Nanostructures for  
Biosensors and Diagnostics

---



# Application of Plasmonic Nanostructures in Molecular Diagnostics and Biosensor Technology: Challenges and Current Developments

*Sanele Nyembe, Andile Mkhohlakali, Bambesiwe May and Nikiwe Mhlanga*

## Abstract

The recent global pandemic caused by Covid-19 enforced the urgent need for accessible, reliable, and accurate point-of-care rapid diagnostics based on plasmonic nanostructures. This is because fast and reliable testing was the key driver in curbing the spread of Covid-19. The traditional methods of diagnostics and biosensors often require expensive infrastructure and highly qualified and trained personnel, which limits their accessibility. These limitations perpetuated the impact of Covid-19 in most countries because of the lack of easily accessible point-of-care rapid diagnostic kits. This review revealed that portable and reliable point-of-care diagnostic kits are very crucial in reaching large populations, especially in underdeveloped and developing countries. This gives perspective to novel point-of-care applications. Furthermore, water quality is a very crucial part of food safety, especially in developing countries faced with water contamination. In this chapter, we explored the various challenges and recent developments in the use of plasmonic nanostructures for application in molecular diagnostics and biosensing for the detection of infectious diseases and common environmental pathogens.

**Keywords:** plasmon, molecular diagnostic, surface plasmon resonance (SPR), nanostructures, infectious diseases, water pathogens, machine learning, SERS

## 1. Introduction

Traditional gold-standard diagnostic techniques combined with advances in nucleic acid-based assays, enzyme-linked immunoassays, and rapid diagnostic assays are widely used for the detection of diseases. Despite the advances presented by these techniques several hurdles such as false positives/negatives, expensive infrastructure or equipment, non-specificity, complicated sample preparation, and assay result

analysis limit their use. This is evidenced by the continued world health organization cases reported from low-resource regions. The need for affordable, specific, simple, user-friendly, rapid, and sensitive, diagnostics remains.

Plasmonic-based diagnostics or biosensors offer an attractive solution in the detection and management of diseases. They can achieve enhanced sensitivity, rapidity, real-time and label-free detection of pathogenic biomarkers [1, 2]. The plasmonic phenomenon yields various techniques: Surface Plasmon Resonance (SPR), Localized Surface Plasmon Resonance (LSPR), colorimetric Plasmonic assays, Surface-Enhanced Raman spectroscopy (SERS) and its variants. Benefiting the diagnostic fraternity, Plasmonic-based assays are merited with a multiplexing potential and smartphone integration [1]. The Plasmonic based sensing platform extends to environmental sensing. Water contamination due to pathogens and biological molecules such as Covid-19 benefits from Plasmonic sensors. In addition to detection, the plasmonic sensors can quantify the pathogens in the drinking waters to inform water treatment measures to be taken.

SPR biosensing is based on the excitation of the free electrons by a polarized light on a metal film which onsets the electrons' collective oscillation [1–3]. A plasmonic surface is immobilized with biomarker receptors, which bind the analyte and induce a change in the local refractive index. The change is perceived through changes in the incident light used for the excitation of the free electrons to the SPR state [1]. This principle has resulted in paradigms for different diseases: malaria [4–6], tuberculosis [7–9], HIV [10, 11], and Covid-19 [12].

The LSPR is based on the confined oscillation of electrons at the metallic surface and the localized SPR distinguishes LSPR from the propagating SPR biosensor. Interaction of the receptor with an analyte in LSPR biosensing induces changes that prompt a wavelength shift in the excitation spectrum. The LSPR-based sensors are excellent for both the detection and quantification of biomolecules/diseases [1, 3]. The potential for LSPR biosensing has been tested on Covid-19 [13], glucose [14], and cancer cells [15].

Colorimetric Plasmonic assays are driven by LSPR of metallic nanostructures such as gold (Au) and silver (Ag) that yield enhanced magnetic fields in the visible/NIR range. This phenomenon yields color changes observed by the naked eye. The color changes merit colorimetric plasmonic assays for point-of-care testing [1, 16].

SERS principle uses the plasmonic effect of the metallic substrates to enhance weak traditional Raman signals. Raman spectroscopy is a fingerprinting tool that is used to study characteristic peaks of molecules. However, its sensitivity is compromised for some molecules especially biomolecules limiting its use in diagnostics. SERS alleviates the low signal challenge by amplifying the weaker signals and availing the technique for biosensing. It is used as either label-free for Raman active analytes or labeled for non-Raman active molecules. Zhou et al. developed an AgNPs based sensor for the detection of bacteria from drinking water. The SERS substrate, AgNPs coats on the cell wall of the bacteria and enhances the Raman signal of the analyte by 30-folds compared to a non-coating AgNPs colloids. The chapter examines the potential for plasmonic-based assays in the detection of diseases and common water pathogens. It compares literature and prototypes in the field and future expectations.

## **2. Plasmonic nanostructures in biosensing**

Biosensors are significant in a variety of scientific domains, including clinical diagnostics, medical diagnostics, illicit drug detection, food quality and safety, and

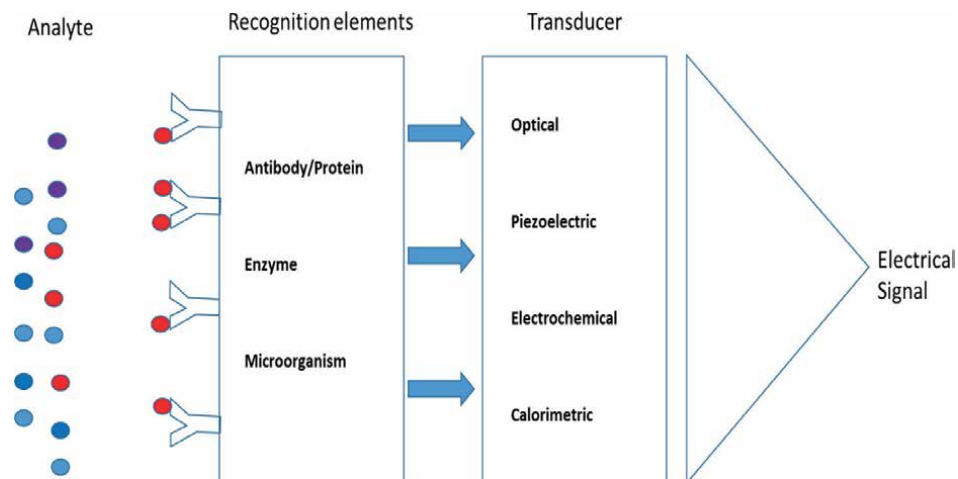


**Figure 1.**  
*General schematic for biosensor as adopted from literature [19].*

environmental evaluation [17]. Biosensor is an analytical device, which consists of two basic components: the recognition unit employed to capture the specific target and the transducer that converts the biomolecule interaction into an electrical, chemical, or optical signal. The types of biosensor depend on the types of output signal measured and quantified in real-time [18]. As depicted in **Figure 1**, the identification of stimulus is released after the interaction of the sensing surface with the analyte and converts it into a detectable signal.

## 2.1 Types of biosensors

Biosensors can be classified according to the output as shown in **Figure 2**. In addition, all these types share a common working principle. Furthermore, electrochemical biosensors are sub-classified into impedimetric, voltammetric, potentiometric, and amperometric. Among these, bio-sensing types, electrochemical sensor is considered as conventional sensor and has been under an extensive search for years. It has attracted interest in several fields such as health, food, and agriculture [3]. However, plasmonic biosensing possesses many advantages over traditional (electrochemical) sensors due to their (i) label-free detection, (ii) real-time, (iii) short response time, and (iv) simple sample preparation.

## 2.2 Plasmonic bio-sensing mechanism and sensing principle

### 2.2.1 Surface plasmon resonance (SPR)

Surface plasmon resonance (SPR) biosensor (**Figure 3**) is one of the important tools for examining the kinetics of biomolecular interaction with the surface and they offer a unique real-time and label-free measurements, non-invasive nature with high detection sensitivity [21]. SPR is a frequently used optical technique for tracking changes in a sensor layer's refractive index (RI) after interaction with a target molecule [3]. SPR has been widely used in various detection of biological and chemical analytes, for environmental and agricultural monitoring [22]. It is a metal-based film

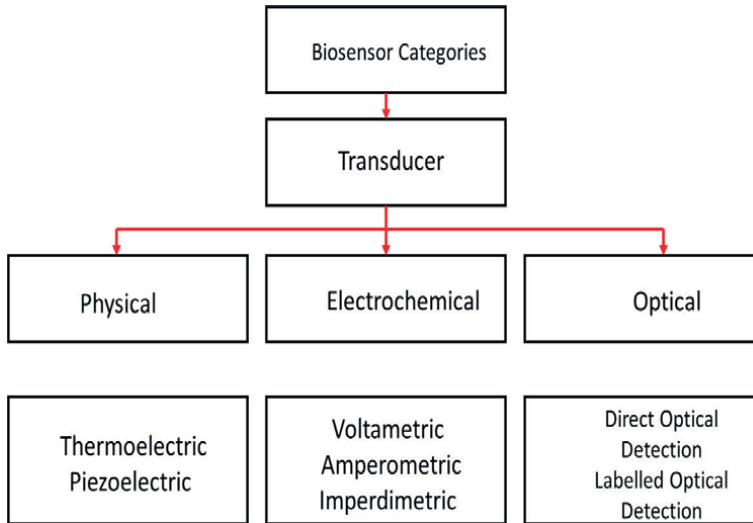


**Figure 2.** Types of biosensor based on their transducer identity [18].

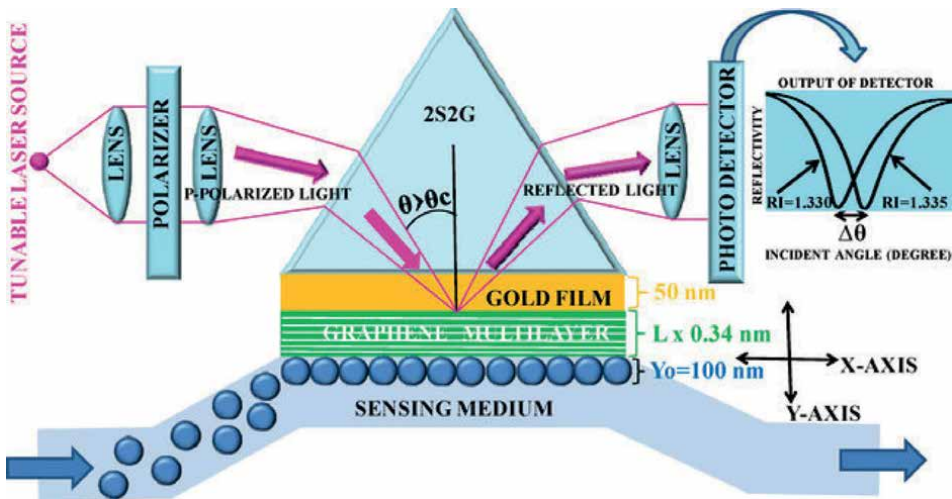


**Figure 3.** Schematic of SPR biosensor experimental set up (a) [20], adopted from literature [10] copyrights, SPR (a) and LSPR (b) sensing mechanism (c).

sensor, made of gold (Au), which is used to characterize biomolecular interactions [23]. SPR systems are based on an optical phenomena pioneered by Wood in the 1980s, which is a gold standard method. The most successful plasmonic up to date, based on optical label-free sensing technology. Wang et al. used hepatitis B surface (HBs) antigen as the target molecule and gold nanorods (AuNRs) to realize LSPR for an HBV sensor [3]. Ever since, there has been ongoing research on developments of label-free, real-time, and ultra-sensitive SPR for the sensing of small and large biomolecules which is based on monitoring of refractive index (RI) changes in the surrounding environment (surface chip sensor) caused by biomolecular interaction around sensing area [24]. These technologies have been widely used in drug screening

and in other biomedical disciplines. Bai and co-workers presented an SPR-based biosensor for the detection of the avian influenza virus (AIV) H5N1. Employing a chosen aptamer as the recognition element [3].

**Figure 3(a)** and **(b)** depicts the SPR sensing mechanism, it can be observed as electromagnetic surface waves that are solution of Max equation. SPR occurs at the interface of the bulk materials with positive dielectric constant and of a negative dielectric constant of the metals (precious metals: Au, Ag) [25]. The electron clouds propagate horizontal (x-y) plane to hundreds of micrometers along the metal-dielectric interface and their lateral extensions and eventually decay exponentially away into both sides of the interface in z-axis [3].

In contrast to SPR, LSPR sensing mechanism (**Figure 3(c)**), the electromagnetic waves are confined and no-propagating surface plasmon at the surface of an isolated metallic nanostructure. As the curve metallic surface of nanoparticle, the interaction between electromagnetic waves applies the restoring force to oscillating electron cloud and amplifies the electromagnetic resonance (EM) field of the metal interface due to resonance. In addition, the light-matter interaction is where LSPR originates [26]. When it comes to plasmonic nanostructures, surface plasmons are restricted to a narrow area near the nanostructures and sensitive to RI changes.

The EM field enhancement can scrutinized and quantified on the metallic surface may be explained using Mie Theory (Eq. (1)), which is frequently used for electromagnetic simulations.

Mie theory;

$$\partial = 4\pi r^3 \frac{\epsilon - \epsilon_m}{\epsilon + 2\epsilon_m} \quad (1)$$

where R and  $\partial$  is a permeability and the radius of the metal nanoparticles. The EM field is sensitive to the changes of RI of the dielectric layer, which has a potential to be used as sensing layer for SPR based sensor realization. Kretschmann and Reather pioneered the creation of SPR-based sensors in 1968 by introducing the traditional prism-based structure, while Liedberg et al. reported the first experimental demonstration of exploiting the phenomenon for sensing. Plenty of companies to manufacture point-of-care (POCs) facilities have utilized these technologies (SPR) sensor mechanism.

### 2.2.2 Localized surface plasmon resonance biosensors (LSPR)

The bioanalytical community has been interested in localized surface plasmon resonance (LSPR) phenomenon. LSPR has many of the same benefits as traditional propagating SPR, but with a few key differences. In comparison to SPR, LSPR has the following benefits: a high aspect ratio that allows for a larger interaction surface area for immobilizing the sensing elements; a miniature probe to produce compact devices; and broad applicability and compatibility with several phenomena, including fluorescence, Raman, and IR spectroscopy. In LSPR, the interaction of the electromagnetic waves and sub-wave metal NPs gives a rise to non-propagating oscillations of the collected electron conducted cloud against metal positive core, this phenomenon is localized surface Plasmon [27]. LSPR operates with the same merits as traditional propagating SPR, however with additional crucial advantages. One of the examples, they are more suitable to microchip integration, faster response time and have much better spatial resolution [28]. Moreover, LSPR has high aspect ratio, thus allowing more interaction surface area for immobilizing the sensing elements to

obtain compact devices and wide stability, compatibility, and applicability towards phenomenon such fluorescence, and Raman and IR spectroscopy to name the few. Researchers have devoted efforts in contribution to the development of noble metal-based LSPR on a planer surface [28]. However, so far, the development of LSPR is restricted at the laboratory scale due to the fundamental limits of noble metals such as their high price and their high production cost [26].

### *2.2.3 Plasmonic nanostructures in biosensing*

Nanostructures offer a wide range of potential uses in biosensors because of their distinctive size-tuneable and shape-dependent physicochemical features. The field of optical biosensors enters a new age with the incorporation of nanostructures and useful biological molecules (such as antibodies, nucleic acids, and peptides) [22]. Loideau et al. have reported the Ag and Ag@Au NPs based LSPR for application in naked-eye biosensing, utilizing color change from cyan to green [28]. In the last two decades, Plasmon resonance in gold nanoparticles (Au NPs) has been the subject of intense research efforts. However, the inflated cost for precious metal such as Ag and Au has been a great concern.

Recently, due to the inflated cost, production cost of noble metals, researchers have paid a considerable attention to the development of non-noble metal and semiconductor materials. As potential replacements for plasmonic noble metals, low-cost and resource-rich non-noble metal plasmonic materials have drawn significant interest [29]. The commonly used non-noble plasmonic material reports are copper-based, Aluminum, semiconductor, and graphene-based LSPR. Non-noble metal like bismuth (Bi) have similar plasmonic properties as precious metal. Chen et al. have reported the synthesis of non-noble (Bi/BiVO<sub>4</sub>) as photoanode sensing materials for application in detection of H<sub>2</sub>O<sub>2</sub> [30]. Zhu et al. reported sponge-like surface-enhanced scattering (SERS) substrate in which reduced graphene oxide used to wrap the Ag nanotube for detection of dithiocarbomates pesticide [31]. Among the support surface for LSPR, glass substrates have been the most popular and been attracted considerable attention for LSPR sensor platform. The LSRP sensing mechanism has been recently been utilized in sensing the eloba virus by Tsang et al. and the nanoparticle have been able to sense the virus at lowest LOD level. While and Li et al. reported the detection of SARS-COV-2 (COVID-19) [29].

### *2.2.4 Bottom-up fabrication methods developments of plasmonic biosensors*

Among the fabrication approaches for plasmon biosensors, bottom-up approach has attracted prodigious interest due to control over the structure, shape, and size as compared to top-down approach. Top-down approach uses lithographic etching, which is associated with undesirable structures. The unique and extremely sensitive nanostructures of SPR and LSPR properties, together with generality of fabrication method used obviate the undesirable optical and structural effect associated lithographical prepared nanostructures for sensing applications. The size and shape of the nanostructures are of great interest, due to their huge influences in fine-tuning the sensitivity due to an enhanced interaction surface area and electric properties compared to the bulk material counterparts. A novel way to get around the constraints of a traditional SPR biosensor's detection limit, sensitivity, selectivity, and throughput provided by recent developments in nanofabrication techniques and nanoparticle syntheses.



Before every step in plasmonic nanostructures developments is the fabrication approach. The fabrication method influences the physical and chemical identity/nature of plasmonic materials, which is the size, and structural morphology to name few. These properties turn to determine the plasmonic biosensor activity. Nanotechnology and nanostructures have shown a great interest in contributing towards the nanoplasmonic materials, which entails biosensing and biological application, through manipulating the sensitivity [32]. Nanostructures as the driving force of nanotechnology, hold the futuristic technological developments of portable devices, and drive the next technology generation such as the fourth industrial revolution (4IR) and machine learning [33, 34].

The recent progress in the fabrication of advanced smart nanostructures find a widely application in the environmental and biological disciplines. In addition, the effort to fabricate nanoplasmonic biosensors based on LSPR mostly noble metal (Au or Ag), to reduce cost, expensive equipment, and these materials exhibited unmatched characteristic features that can be utilized [35]. In this regard, the optical characteristics of metallic nanostructures such as Au and Ag nanoparticles (NPs) have been developed and utilized to create simple, fast-responding, and low-cost nanodiagnostic and nanotherapeutic smart systems due to their chemical stability and biocompatibility [36]. In fact, due to their intense interactions with light, AuNPs and AgNPs are specifically studied for their optical features [37].

Masterson et al. reported the bottom-up synthesis of AuNPs, AuNRs [38]. There are many methods used to fabricate plasmon nanostructures with various morphologies, that is, nanoplates, nanorods, nanosphere, nanoarrays, etc. [39] as shown in **Table 1**. Kim and co-workers reported the nanoarrays using electron beam lithography, for detection of avian DNA-Influenza utilizing the SPR [45]. In 2018, Liu et al. reported the Au nanoplates using the hydrothermal synthesis for the sensing of, [46].

### 2.2.5 The limitation of plasmonic biosensors

The inability to consistently detect minor changes in refractive index brought on by substances in low concentration at the sensor surface is one of the primary issues preventing the further development of SPR applications. The expense of noble metals used in plasmonic biosensors. In addition, there are still many obstacles to overcome, both now and in the future, despite the recent boom in the development of nanomaterial-based plastic sensors for POC facilities applications. Among the technology bottleneck, researcher mostly discuss the plasmonic biosensors that are urgent which limits the development of biosensors. The first one is the Covid-19 global pandemic,

Fabrication method	Materials	Application	Ref
Template method	Au nano slit		[40]
Chemical reduction	Ag nanoparticles		[41]
Seed-mediated growth	Au nanorod	Detection of tuberculosis	[42]
Electrodeposition	Au, Ag, Cu	Antigen-antibody detection	[43]
Hydrothermal/solvothermal	Au nanoplates	SERS enhancement	[44]

**Table 1.** Summarized list of methods for the synthesis of various nanostructures morphology and their applications.

which requires rapid, POC diagnostic facility to urgent identify contraction of the (SARS-COV-2) virus. Another challenge I to quickly develop the accurate, reliable plasmonic biosensor that is flexible in realization of 4IR and machine-learning tool that can easily use to predict the sensing properties of the nanoparticles [44].

### **3. Biosensing for environmental monitoring**

The increased industrial and agricultural activities have increased the levels of chemical and biological substances being release into the environment. Thus, environmental monitoring is mandatory. This drives the need for real-life detection with rapid measurements that allows environmental monitoring in various real-life situations. Plasmonic biosensors have shown the potential to detect pollutants directly and reliably in the environment. The most common analytes detected by biosensors for environmental monitoring include heavy metals in water, pesticides, and potentially toxic and dangerous chemicals such as explosives [19, 23, 47–49]. Conventional sensing substrates have been improved with plasmonic materials for enhanced performance. The design of specific plasmonic structures made it possible for easy binding of analytes, bringing the pollutants close to the surface of the plasmonic sites [47].

#### **3.1 Heavy metals**

Heavy metals such as Cu, Hg, Pb, and Cd are among the harmful inorganic pollutants released into the environment from industrial and agricultural activities [50–52]. They do not decompose naturally and thus become persistent in water streams and agricultural land. Since their presence is regulated, their detection is mandatory to prevent diseases, protect the environment and strategize viable treatment plans to meet regulation requirements [53].

One of the most common plasmonic biosensors are colorimetric sensors. They offer convenient, rapid in field pollutant response that can be observed with the naked eye. This type of sensing is possible because the local surface Plasmon resonance peaks of the biosensors fall within the visible spectrum and the aggregation that occurs in the presence of the pollutant/analytes cause changes in color [47]. For instance, detection of  $\text{Hg}^{2+}$  ions were demonstrated using mercaptopropionic acid (MPA) capped Au NPs, where Hg ions complexed with carboxylic acid groups of MPA revealing a color change from red to colorless. The selectivity of  $\text{Hg}^{2+}$  ions among other metals was improved in the presence of 2,6-pyridinedicarboxylic acid (PDCA) due to increased complexation coefficient. As a result, a quantitative detection range of 250–500 nM with a limit of detection of 100 nM was established [54].

In another development, a rapid color change from blue to red was observed in the detection of  $\text{Pb}^{2+}$  ions with DNA zyme assembly of Au NPs (**Figure 4**) [55]. The DNA zyme assembly forms a hybrid with Au NPs, which resulted in aggregation. Furthermore, the presence of lead catalyzes the hydrolytic cleavage, which disassembles the hybrid into dispersed Au NPs bringing the color, back to red (**Figure 4**) [55].

#### **3.2 Pesticide and explosives**

The release of organic pollutants such as pesticides (used in agriculture) and polycyclic aromatic hydrocarbons (PAHs), polychlorinated biphenyls, phenol, dioxins (by-products of combustion, incineration, and chemical manufacturing processes)

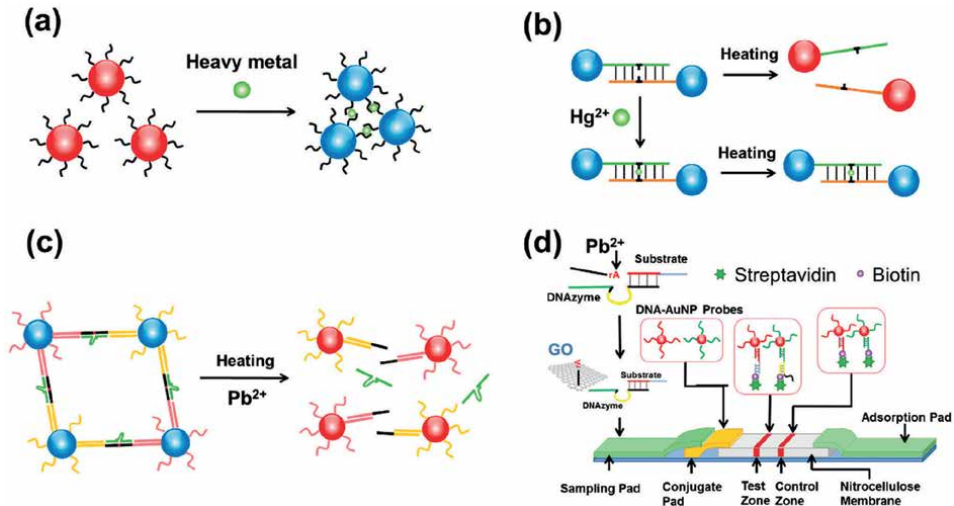


**Figure 4.** DNA zyme-directed assembly formation and cleavage of Au NPs during  $Pb^{2+}$  ion colorimetric sensing. Reprinted with permission from Reference [55].

into the environment presents a concern for environmental protection. For example, pesticides and PAHs can accumulate in soil and water and they pose endocrine-disrupting activity, which can be a threat to human health and local ecosystems [56, 57]. Many SPR-based immunosensors have shown potential in the detection of these environmental pollutants such as atrazine, Dichloro-Diphenyl Trichloroethane (DDT), 2,3,7,8-tetrachlorodibenzo-p-dioxin, carbaryl, 2,4-D, benzo[a]pyrene (BaP), biphenyl derivatives, and trinitrotoluene (TNT) [22, 58, 59]. Recently, signal amplification for the detection of TNT was demonstrated using LSPR-based AuNPs. TNT detection occurred through the formation of a Meisenheimer complex with

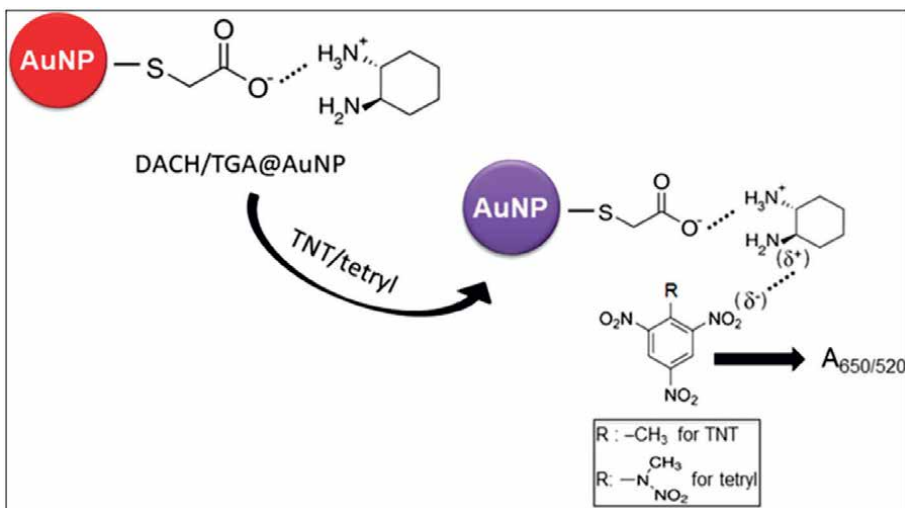


**Figure 5.** The formation of Meisenheimer complex between L-cysteine capped Au NPs and TNT. Reprinted with permission from Reference [60].

L-Cysteine capped AuNPs (**Figure 5**). The electrostatic attraction between the TNT and L-cysteine capped Au NPs resulted in aggregation of the NPs. The material could detect TNT in shampoo solution demonstrating good selectivity [61]. SERS substrates based on AuNRs were applied for the detection of low levels of three dithiocarbamate fungicides. Their interaction between the pesticides and the Au-NRs resulted in the formation of Au-S covalent bonds on the surface between the pesticides and the Au-NRs. Detection limits of 34, 26, and 13 nM were discovered for thiram, firmam, zeram, respectively [60].

## **4. Plasmonic nanostructures in diagnostics**

### **4.1 Molecular diagnostics assays**

Historically, molecular diagnostics assays polymerase chain reaction (PCR) have played a key role in society in curbing the spread and effects of various infectious diseases through early detection [36, 62]. Even though, this technology provides fast and reliable results and do not require any post processing, its limitations are still the expensive machinery, lengthy assay times and sophisticated operational processes that often require a trained personnel [63, 64]. The fast development of nanotechnology and their use in biotechnology has shone a new light towards the use of molecular diagnostics. Specifically, the use of plasmonic nanoparticles has had a significant impact on the clinical and life science [65]. Plasmonic optical properties make them ideal for use in molecular diagnostics because they improve sensitivity, selectivity, efficiency in drug delivery and specificity [66, 67]. K. Jiang et al. reported the use plasmonic magnetic nanoparticles covered with silica core shell for the detection of DNA ranging from  $0.5 \text{ ng } \mu\text{L}^{-1}$  to  $3 \text{ fg } \mu\text{L}^{-1}$  within 20 minutes using cPCR [62, 67]. This study shows the importance of using plasmonic nanoparticles for the detection of diseases in real time that is acquit of traditional molecular diagnosis limitations such as lengthy assay times. In this study, the plasmonic magnetic nanoparticles were used for their dual function of thermal cycling and magnetic separation and detectable color change [62].

### **4.2 Surface-enhanced Raman scattering immunoassays**

SERS-based immunoassays are a promising tool and integral for the identification of biological threats through early detection of biomarkers, which is crucial for disease control [68]. The SERS technology the plasmonic nanoparticles are functionalized with Raman reporters, which are attached to protein binding membranes. The binding membrane facilitates the detection of diseases and shows high sensitivity [69]. Gold, silver, copper, and platinum nanoparticles have been used to improve sensitivity and enhancement factor of the SERS substrate [70]. The schematic illustration of a typical SERS immunoassay is shown in **Figure 6**.

However, in recent years the SERS technology has been moving away from the use of pristine spherical nanoparticles and moving towards the different morphologies and composites. The reason for the observed shifts is due to the realization that plasmonic using pristine spherical nanoparticles does not realize the full potential of SERS in point of care tests. S. Nyembe et al. performed a comparison study of gold nanowires (diameter of 10 nm) with various gold nanoparticles (14, 30 and 40 nm) and the results showed that gold nanowires had a better enhancement factor than

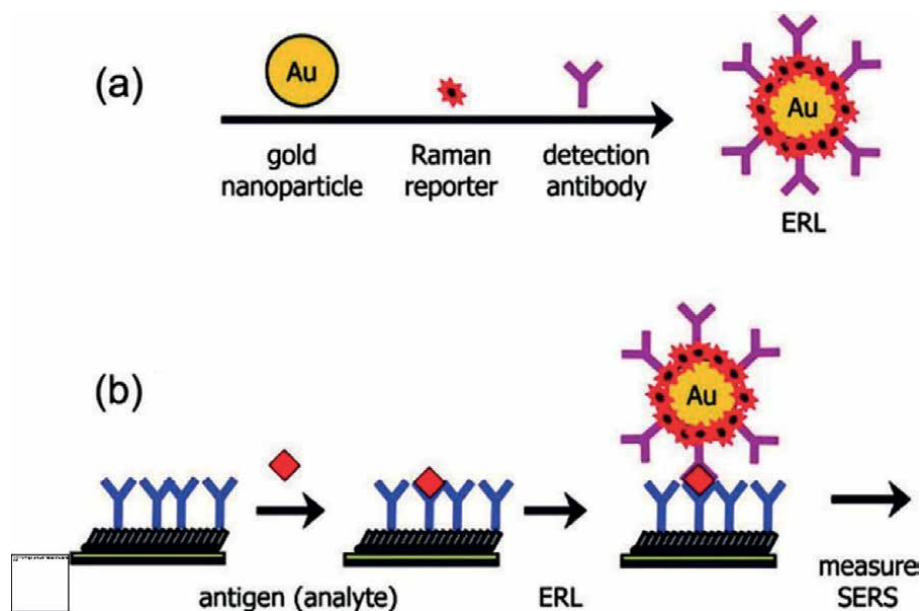


**Figure 6.** Schematic illustration of a typical SERS sandwich immunoassay for biomarker detection [71].

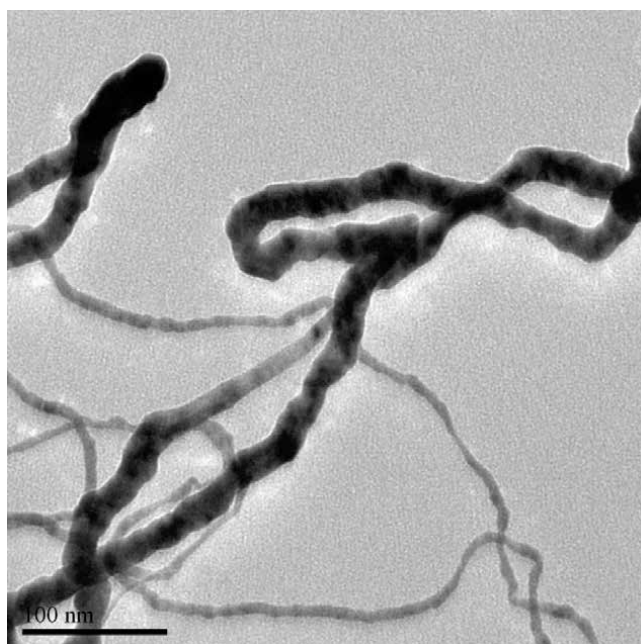


**Figure 7.** TEM image of gold nanowires [72].

the spherical gold nanoparticles [72]. The higher enhancement factor was due to better adsorption capacity due to higher surface area and from entrapment caused by interstices formed by their network as shown in **Figure 7** [72].

## **5. Prospects of molecular diagnostics and biosensing using plasmonic nanostructures**

### **5.1 Gold standard methods**

Covid-19 is an acute respiratory disease that has infected over 500 million people worldwide and has taken lives of over 6 million people (as of November 2021). During the pandemic, governments offered tests sights in various locations to test as many people as possible using traditional testing methods. However, long queues, registering procedures and traveling proved to be major challenges. To curb the spread of this virus government required diagnostic sensors that are timely, portable, and accurate POC so that more people could be tested [44].

There are diagnostic methods that are regarded as gold standards for detection of infectious diseases such as detection of TB and HIV using immunoassay and Covid-19 via PCR [73]. These diagnostic standards are regarded as low cost, extremely sensitive and easy to operate with low limit of detection [74]. However, the recent 2020 worldwide Covid-19 pandemic forced a divergence use of the traditional gold standards methods. The gold standards methods often requires a well-trained physicians and it is time consuming. The alternative testing such as lateral flow immunoassay and other plasmonic nano sensors significantly reduces the time for results down to 15 minutes with an added advantage of portability. Even though the detection limit of the gold standard methods is superior to the plasmonic nano sensors, there is a consensus prospects that these diagnostic nano sensors based on plasmonic nanoparticles would be use more in the future to reach masses for screening of infectious diseases [44].

### **5.2 Miniaturization**

The optical biosensors often require a reliable light source and an optical read out instrument. The optical biosensors mostly relies on the natural sun light as the source of light and the human eye as the photo-detector in the visible wavelength. A good example of these optical biosensors are the colorimetric pregnancy tests [44]. Where the nanoparticles such as gold produces LSPR that induces light absorption change detectable by the naked eye. The future of this technology heavily depends on the development of semiconductor technology to produce extremely sensitive, reliable and enhance resolution results. The fast growing semiconductor technology in the cell phone industry means that cell phones are now equipped with powerful computing power and high resolution cameras. These cell phone capabilities means that in the future, the light emitted diode (LED) from cell phones, could be used as a light source with accurately controlled wavelength and intensity. The high-resolution camera of a cell phone could be used as sensitive photo-detectors for the sensing. Hence, in the future, cell phones would be used to provide real-time diagnostic results via analysis of optical signal analyzed with complex algorithms [44].

### **5.3 Theranostics**

Theranostics is a nanomedicine that comprises of both diagnosis and therapies of illnesses achieved by using a biomaterial based nanoplatform. This nanomedicine technology uses nanostructures within the 1 to 100 nm range that are functionalised with organic or inorganic materials and often with an engineered compound such

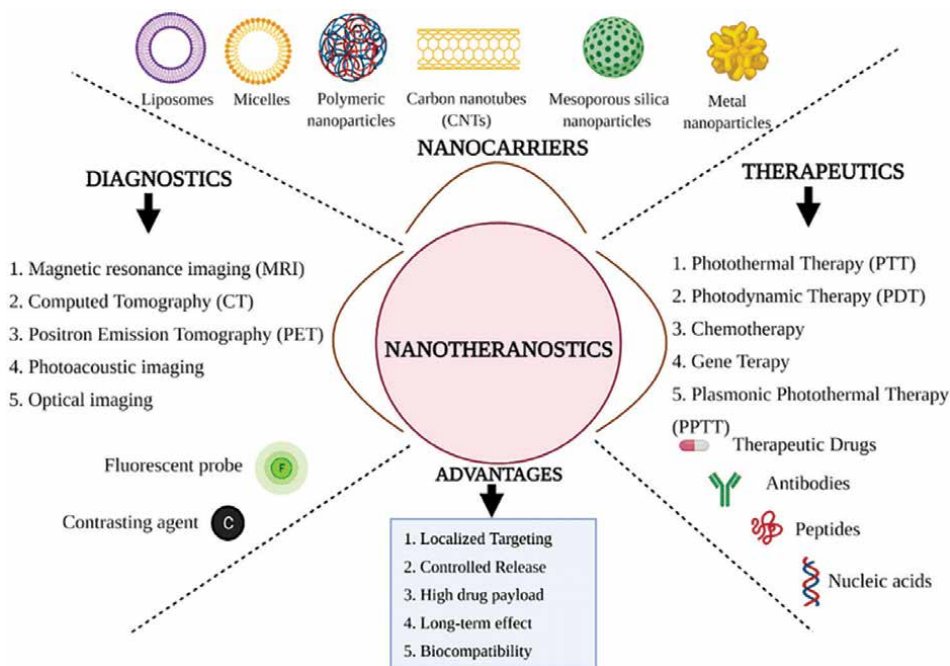


**Figure 8.** Various therapies and diagnostic approaches used for the theranostic concept [75].

as phthalocyanine that could disrupt the functionality of the cells of the infectious disease [75]. The functional groups on the surface of the nanoparticles usually directs them to the desired location of the infectious disease that could be detected using ultrasound, MRI, or CT scans (diagnosis). Once at the target site, the engineered compounds are activated by energy source such as laser (phototherapy), causing them to release energy causing a cell destruction (therapy) such as stubborn cancer cells. The advantages of theranostics technology that would make this the technology of choice in the future are; improved targeting effect, reduced systematic toxicity and enhanced solubilizing potential to hydrophobic drugs [76]. **Figure 8** shows a schematic of the dual effects of theranostic approaches.

Even though application of plasmonic materials in bio-molecular sensing has seen great leaps in the past couple of decades and has circumvented multiple challenges. The areas that are leading the path into the future for the biosensing technologies is machine learning and artificial intelligence.

#### 5.4 Machine learning

Plasmonic biosensors uses plasmonic nanoparticles to enhance the surface Plasmon effect, which highly depends on the morphology of the nanoparticles. The different morphology of these nanoparticles offer difference optical properties. Hence, it is crucial to design the plasmonic nanoparticles to suit its application [77, 78]. Difference morphology are often required for the detection of different infectious diseases such as human immunodeficiency virus (HIV), tuberculosis (TB), hepatitis B virus (HBV) with varying limits of detection. The various morphology of plasmonic nanoparticles is shown in **Table 1**.

The prospects of using plasmonic nanoparticles would depend on better understanding and accurate prediction of the plasmonic properties of the nanoparticles. Often optical properties of nanoparticles are computed using molecular modeling. However, it is challenging to predict with a high degree of accuracy the perfect nanoparticle morphology with the required optical properties. Furthermore, molecular modeling is time consuming [79, 80]. The recent developments of machine learning and artificial intelligence are the answer for this challenge and holds hope for future applications. Machine learning is more accurate in predicting the required properties for the application. Furthermore, machine learning has the capabilities to optimize the design parameters of the plasmonic nanoparticles to achieve the required optical properties [81]. Hence, machine learning serves as the powerful tool that can be used extensively in various plasmonic image analysis for better understanding their optical properties.

## **6. Conclusion**

Plasmonic nanostructures with various morphologies have sparked interest for use in biomarker sensing and rapid diagnostics. Spherical plasmonic nanoparticles such as gold and silver have played an integral part of these technologies, however, in recent years other morphologies such as rods and nanowires have been of interest due to their high aspect ratios and high surface area. In this chapter, the fundamental plasmon properties were explored for various diagnostic and biosensing applications in infectious diseases and common water pathogens. We also explored the prospects for rapid diagnostics and biomarker technologies in a world that requires test results efficiently, reliably, and quickly. The fate of traditional diagnostic technologies was also discussed with some new developments that would help this technology soon.

## **Acknowledgements**

Analytical chemistry division at Mintek, Johannesburg, South Africa, supported this work. The Department of Science and Innovation (DSI) supported this work, South Africa, through the DSI/Mintek, Nanotechnology Innovation Centre (NIC). The authors wish to acknowledge NIPMO (The National Intellectual Property Management Office—South Africa).



## **Author details**

Sanele Nyembe<sup>1\*</sup>, Andile Mkhohlakali<sup>1</sup>, Bambesiwe May<sup>1</sup> and Nikiwe Mhlanga<sup>2</sup>


1 Analytical Chemistry Division/Mintek, Johannesburg, South Africa

2 DST/Mintek Nanotechnology Innovation Centre, Advanced Materials Division, Mintek, Johannesburg, South Africa

\*Address all correspondence to: [saneleny@mintek.co.za](mailto:saneleny@mintek.co.za)

## **IntechOpen**

---

© 2022 The Author(s). Licensee IntechOpen. This chapter is distributed under the terms of the Creative Commons Attribution License (<http://creativecommons.org/licenses/by/3.0>), which permits unrestricted use, distribution, and reproduction in any medium, provided the original work is properly cited. 

## References

- [1] Li Z, Leustean L, Inci F, Zheng M, Demirci U, Wang S. Plasmonic-based platforms for diagnosis of infectious diseases at the point of care. *Biotechnology Advances*. 2019;**37**(8):107440
- [2] Yu T, Wei Q. Plasmonic molecular assays: Recent advances and applications for mobile health. *Nano Research*. 2018;**11**(10):5439-5473
- [3] Shrivastav AM, Cvelbar U, Abdulhalim I. A comprehensive review on plasmonic-based biosensors used in viral diagnostics. *Communications Biology*. 2021;**4**(1):1-12
- [4] Wu F, Singh J, Thomas PA, Ge Q, Kravets VG, Day PJ, et al. Ultrasensitive and rapid detection of malaria using graphene-enhanced surface plasmon resonance. *2D Materials*. 2020;**7**(4):045019
- [5] Panda A, Pukhrambam PD. Modeling of high-performance SPR refractive index sensor employing novel 2D materials for detection of malaria pathogens. *IEEE Transactions on NanoBioscience*. 2021;**5**:312-319
- [6] Loyez M, Wells M, Hambÿe S, Hubinon F, Blankert B, Wattiez R, et al. PfHRP2 detection using plasmonic optrodes: Performance analysis. *Malaria Journal*. 2021;**20**(1):1-9
- [7] Hsieh S-C, Chang C-C, Lu C-C, Wei C-F, Lin C-S, Lai H-C, et al. Rapid identification of *Mycobacterium tuberculosis* infection by a new array format-based surface plasmon resonance method. *Nanoscale Research Letters*. 2012;**7**(1):1-6
- [8] Prabowo BA, Alom A, Secario MK, Masim FCP, Lai H-C, Hatanaka K, et al. Graphene-based portable SPR sensor for the detection of *Mycobacterium tuberculosis* DNA strain. *Procedia Engineering*. 2016;**168**:541-545
- [9] Maphanga C, Ombinda-Lemboumba S, Manoto S, Mthunzi-Kufa P. Surface plasmon resonance (SPR) based biosensor for *Mycobacterium tuberculosis* diagnosis. In: Cote GL, editor. *Optical Diagnostics and Sensing XXI: Toward Point-of-Care Diagnostics*. Rochester, NY, United States of America: International Society for Optics and Photonics; 2021. pp. 1-8
- [10] Sarcina L, Mangiatordi GF, Torricelli F, Bollella P, Gounani Z, Österbacka R, et al. Surface plasmon resonance assay for label-free and selective detection of HIV-1 p24 protein. *Biosensors*. 2021;**11**(6):180
- [11] Lugongolo MY, Manoto SL, Maphanga C, Ombinda-Lemboumba S, Thobakgale SL, Mthunzi-Kufa P. Label-free detection of mutations in the HIV genome using a surface plasmon resonance biosensor. In: Vo-Dinh T, editor. *Plasmonics in Biology and Medicine XVIII*. San Francisco, United States of America: International Society for Optics and Photonics; 2021. pp. 6-12
- [12] Basso CR, Malossi CD, Haisi A, de Albuquerque Pedrosa V, Barbosa AN, Grotto RT, et al. Fast and reliable detection of SARS-CoV-2 antibodies based on surface plasmon resonance. *Analytical Methods*. 2021;**13**(29):3297-3306
- [13] Yang Y, Murray J, Haverstick J, Tripp RA, Zhao Y. Silver nanotriangle array-based LSPR sensor for rapid coronavirus detection. *Sensors and Actuators B: Chemical*. 2022;**359**:131604

- [14] Yang Q, Zhu G, Singh L, Wang Y, Singh R, Zhang B, et al. Highly sensitive and selective sensor probe using glucose oxidase/gold nanoparticles/graphene oxide functionalized tapered optical fiber structure for detection of glucose. *Optik*. 2020;**208**:164536
- [15] Chang C-Y, Lin H-T, Lai M-S, Shieh T-Y, Peng C-C, Shih M-H, et al. Flexible localized surface plasmon resonance sensor with metal-insulator-metal nanodisks on PDMS substrate. *Scientific Reports*. 2018;**8**(1):1-8
- [16] Mauriz E. Clinical applications of visual plasmonic colorimetric sensing. *Sensors*. 2020;**20**(21):6214
- [17] Soler M, Lechuga LM. Principles, technologies, and applications of plasmonic biosensors. *Journal of Applied Physics*. 2021;**129**(11):111102
- [18] Shavanova K, Bakakina Y, Burkova I, Shtepliuk I, Viter R, Ubelis A, et al. Application of 2D non-graphene materials and 2D oxide nanostructures for biosensing technology. *Sensors (Switzerland)*. 2016;**16**(2):223
- [19] Fatima A, Younas I, Ali MW. An overview on recent advances in biosensor technology and its future application. *Archives of Pharmacy Practice*. 2022;**13**(1):5-10
- [20] Firdous S, Anwar S, Rafya R. Development of surface plasmon resonance (SPR) biosensors for use in the diagnostics of malignant and infectious diseases. *Laser Physics Letters*. 2018;**15**(6):065602
- [21] Zeng Y, Hu R, Wang L, Gu D, He J, Wu SY, et al. Recent advances in surface plasmon resonance imaging: Detection speed, sensitivity, and portability. *Nano*. 2017;**6**(5):1017-1030
- [22] Long F, Zhu A, Shi H. Recent advances in optical biosensors for environmental monitoring and early warning. *Sensors (Switzerland)*. 2013;**13**(10):13928-13948
- [23] Hamza ME, Othman MA, Swillam MA. Plasmonic biosensors: Review. *Biology (Basel)*. 2022;**11**(5):621
- [24] Wang G, Wang C, Yang R, Liu W, Sun S. A sensitive and stable surface plasmon resonance sensor based on monolayer protected silver film. *Sensors (Switzerland)*. 2017;**17**(12):2777
- [25] Lance Kelly K, Coronado E, Zhao LL, Schatz GC. The optical properties of metal nanoparticles: The influence of size, shape, and dielectric environment. *The Journal of Physical Chemistry*. 1991;**90**(5):183-185
- [26] Zhou J, Wang Y, Zhang L, Li X. Plasmonic biosensing based on non-noble-metal materials. *Chinese Chemical Letters*. 2018;**29**(1):54-60. DOI: 10.1016/j.ccl.2017.09.003
- [27] Minopoli A, Acunzo A, Della Ventura B, Velotta R. Nanostructured surfaces as plasmonic biosensors: A review. *Advanced Materials Interfaces*. 2022;**9**(2):2101133
- [28] Fan M, Thompson M, Andrade ML, Brolo AG. Silver nanoparticles on a plastic platform for localized surface plasmon resonance biosensing. *Analytical Chemistry*. 2010;**82**(15):6350-6352
- [29] Du X, Sun J, Jiang D, Du W. Non-noble metal plasmonic enhanced photoelectrochemical sensing of chlorpyrifos based on 1D TiO<sub>2</sub>-x/3D nitrogen-doped graphene hydrogel heterostructure. *Analytical and Bioanalytical Chemistry*. 2021;**413**(21):5373-5382
- [30] Chen Y, Xin Y, Congfei Yao YM. Non-noble metal Bi/BiVO<sub>4</sub> photoanode

for surface plasmon resonance-induced photoelectrochemical biosensor of hydrogen peroxide detection. *Journal of Solid State Electrochemistry*. 2012;**26**:1323-1331

[31] Zhu C, Wang X, Shi X, Yang F, Meng G, Xiong Q, et al. Detection of dithiocarbamate pesticides with a spongelike surface-enhanced Raman scattering substrate made of reduced graphene oxide-wrapped silver nanocubes. *ACS Applied Materials & Interfaces*. 2017;**9**(45):39618-39625

[32] Zhang X, Guo Q, Cui D. Recent advances in nanotechnology applied to biosensors. *Sensors*. 2009;**9**(2):1033-1053

[33] Pitkethly MJ. Nanomaterials – The driving force. *Materials Today*. 2004;**7**(12 SUPPL.):20-29. DOI: 10.1016/S1369-7021(04)00627-3

[34] Zhang Y, Zhou Q, Zhu J, Yan Q, Dou SX, Sun W. Nanostructured metal chalcogenides for energy storage and electrocatalysis. *Advanced Functional Materials*. 2017;**27**(35):1-34

[35] Nocerino V, Miranda B, Tramontano C, Chianese G, Dardano P, Rea I, et al. Plasmonic nanosensors: Design, fabrication, and applications in biomedicine. *Chem*. 2022;**10**(5):150

[36] Katsanis SH, Katsanis N. Molecular genetic testing, and the future of clinical genomics. *Nature Reviews Genetics*. 2013;**14**(6):415-426

[37] Loiseau A, Asila V, Boitel-Aullen G, Lam M, Salmain M, Boujday S. Silver-based plasmonic nanoparticles for and their use in biosensing. *Biosensors*. 2019;**9**(2):1-40

[38] Masterson AN, Liyanage T, Kaimakliotis H, Gholami Derami H,

Deiss F, Sardar R. Bottom-up fabrication of plasmonic nanoantenna-based high-throughput multiplexing biosensors for ultrasensitive detection of microRNAs directly from cancer patients' plasma. *Analytical Chemistry*. 2020;**92**(13):9295-9304

[39] Ou X, Liu Y, Zhang M, Hua L, Zhan S. Plasmonic gold nanostructures for biosensing and bioimaging. *Microchimica Acta*. 2021;**188**(9):304

[40] Lee KL, Chen PW, Wu SH, Bin HJ, Yang SY, Wei PK. Enhancing surface plasmon detection using template-stripped gold nanoslit arrays on plastic films. *ACS Nano*. 2012;**6**(4):2931-2939

[41] Mahmudin L, Ulum MS, Farhamsa D, Suharyadi E, Utomo ABS, Abraha K. The effect of variation of reducing agent concentration on optical properties of silver nanoparticles as active materials in surface plasmon resonance (SPR) biosensor. *Journal of Physics Conference Series*. 2019;**1242**(1):2-7

[42] Sun W, Yuan S, Huang H, Liu N, Tan Y. A label-free biosensor based on localized surface plasmon resonance for diagnosis of tuberculosis. *Journal of Microbiological Methods*. 2017;**142**(May):41-45. DOI: 10.1016/j.mimet.2017.09.007

[43] Qin LX, Li Y, Li DW, Jing C, Chen BQ, Ma W, et al. Electrodeposition of single-metal nanoparticles on stable protein 1 membranes: Application of plasmonic sensing by single nanoparticles. *Angewandte Chemie, International Edition*. 2012;**51**(1):140-144

[44] Jin C, Wu Z, Molinski JH, Zhou J, Ren Y, Zhang JXJ. Plasmonic nanosensors for point-of-care biomarker detection. *Materials Today Bio*.

2022;**14**(April):100263. DOI: 10.1016/j.mtbio.2022.100263

[45] Kim SA, Byun KM, Kim K, Jang SM, Ma K, Oh Y, et al. Surface-enhanced localized surface plasmon resonance biosensing of avian influenza DNA hybridization using subwavelength metallic nanoarrays. *Nanotechnology*. 2010;**21**:355503

[46] Liu Y, Yang L, Shen Y. Hydrothermal synthesis of gold nanoplates and their structure-dependent LSPR properties. *Journal of Materials Research*. 2018;**33**(18):2671-2679

[47] Wei H, Hossein Abtahi SM, Vikesland PJ. Plasmonic colorimetric and SERS sensors for environmental analysis. *Environmental Science. Nano*. 2015;**2**(2):120-135. DOI: 10.1039/C4EN00211C

[48] Tashev T, Deliyski R. Biosensors for environmental monitoring. *Challenges for Higher Education and Research*. 2014;**12**(3):123-127

[49] Liu J, Jalali M, Mahshid S, Wachsmann-Hogiu S. Are plasmonic optical biosensors ready for use in point-of-need applications? *The Analyst*. 2020;**145**(2):364-384

[50] Mitra S, Chakraborty AJ, Tareq AM, Emran T Bin, Nainu F, Khusro A, et al. Impact of heavy metals on the environment and human health: Novel therapeutic insights to counter the toxicity. *Journal of King Saud University - Science*. 2022;**34**(3):101865. DOI: 10.1016/j.jksus.2022.101865

[51] Xiang Y, Lu Y. An invasive DNA approach toward a general method for portable quantification of metal ions using a personal glucose meter. *Chemical Communications*. 2013;**49**(6):585-587

[52] Sarıöz Ö, Sürme Y, Muradoğlu V. Heavy-metal extraction capability of chalcogenoic aminophosphines derived from 1-amino-4-methylpiperazine. *Chemical Papers*. 2013;**67**(10):1345-1349

[53] Addo-Bediako A, Malakane K. Preliminary assessment of chemical elements in sediments and larvae of gomphidae (Odonata) from the blyde river of the olifants river system, South Africa. *International Journal of Environmental Research and Public Health*. 2020;**17**(21):1-10

[54] Huang CC, Chang HT. Parameters for selective colorimetric sensing of mercury (II) in aqueous solutions using mercaptopropionic acid-modified gold nanoparticles. *Chemical Communications*. 2007;**12**:1215-1217

[55] Liu J, Lu Y. A colorimetric lead biosensor using DNAzyme-directed assembly of gold nanoparticles. *Journal of the American Chemical Society*. 2003;**125**(22):6642-6643

[56] Tanabe S. Contamination and toxic effects of persistent endocrine disruptors in marine mammals and birds. *Marine Pollution Bulletin*. 2002;**45**(1-12):69-77

[57] Petrovic M, Radjenovic J, Postigo C, Kuster M, Farre M, Alda ML, et al. Emerging contaminants in waste waters: Sources and occurrence. *The Handbook of Environmental Chemistry Vol 5 Water Pollut*. 2008;**5** S1(April):1-35

[58] Long F, Gao C, Shi HC, He M, Zhu AN, Klibanov AM, et al. Reusable evanescent wave DNA biosensor for rapid, highly sensitive, and selective detection of mercury ions. *Biosensors & Bioelectronics*. 2011;**26**(10):4018-4023

[59] Shankaran DR, Gobi KV, Miura N. Recent advancements in surface plasmon resonance immunosensors for detection

of small molecules of biomedical, food and environmental interest. *Sensors and Actuators B: Chemical*. 2007;**121**(1):158-177

[60] Saute B, Premasiri R, Ziegler L, Narayanan R. Gold nanorods as surface enhanced Raman spectroscopy substrates for sensitive and selective detection of ultra-low levels of dithiocarbamate pesticides. *The Analyst*. 2012;**137**(21):5082-5087

[61] Dasary SSR, Singh AK, Senapati D, Yu H, Ray PC. Gold nanoparticle based label-free SERS probe for ultrasensitive and selective detection of trinitrotoluene. *Journal of the American Chemical Society*. 2009;**131**(38):13806-13812

[62] Jiang K, Wu J, Qiu Y, Go YY, Ban K, Park HJ, et al. Plasmonic colorimetric PCR for rapid molecular diagnostic assays. *Sensors and Actuators B: Chemical*. 2021;**337**:129762

[63] Yang T, Luo Z, Tian Y, Qian C, Duan Y. Design strategies of AuNPs-based nucleic acid colorimetric biosensors. *Trends in Analytical Chemistry*. 2020;**124**:115795

[64] Ottesen EA, Hong JW, Quake SR, Leadbetter JR. Microfluidic digital PCR enables multigene analysis of individual environmental bacteria. *Science*. 2006;**314**(5804):1464-1467

[65] Zou L, Shen R, Ling L, Li G. Sensitive DNA detection by polymerase chain reaction with gold nanoparticles. *Analytica Chimica Acta*. 2018;**1038**:105-111

[66] Liu X, Wu Z, Zhang Q, Zhao W, Zong C, Gai H. Single gold nanoparticle-based colorimetric detection of picomolar mercury ion with dark-field microscopy. *Analytical Chemistry*. 2016;**88**(4):2119-2124

[67] Zhou W, Gao X, Liu D, Chen X. Gold nanoparticles for in vitro diagnostics. *Chemical Reviews*. 2015;**115**(19):10575-10636

[68] Frimpong R, Jang W, Kim J-H, Driskell JD. Rapid vertical flow immunoassay on AuNP plasmonic paper for SERS-based point of need diagnostics. *Talanta*. 2021;**223**:121739

[69] Hwang J, Lee S, Choo J. Application of a SERS-based lateral flow immunoassay strip for the rapid and sensitive detection of staphylococcal enterotoxin B. *Nanoscale*. 2016;**8**(22):11418-11425

[70] Chen S-Y, Lazarides AA. Quantitative amplification of Cy5 SERS in 'warm spots' created by plasmonic coupling in nanoparticle assemblies of controlled structure. *The Journal of Physical Chemistry C*. 2009;**113**(28):12167-12175

[71] Li D, Wang Y. Plasmonic nanostructures as surface-enhanced Raman scattering (SERS) substrate for protein biomarker sensing. In: Barbillon G, editor. *Nanoplasmonics – Fundamentals and Applications*. London: IntechOpen; 2017. pp. 1-19. [cited 2022 Jun 18]. Available from: <https://www.intechopen.com/chapters/55189>. DOI: 10.5772/intechopen.68164

[72] Nyembe S, Shumbula P, Moloto N, Ndlovu G, Mhlanga N, Sikhwivhilu L. Raman activity of HS-(CH<sub>2</sub>)<sub>n</sub>-NH-Coumarin molecule adsorbed on the surface of gold nanostructures with various morphologies. *Advances in Theoretical & Computational Physics*. 2021;**4**(3):259-265

[73] Tymms C, Zhou J, Tadimety A, Burklund A, Zhang JXJ. Scalable COVID-19 detection enabled by lab-on-chip biosensors. *Cellular and Molecular Bioengineering*. 2020;**13**(4):313-329

[74] Lei R, Huo R, Mohan C. Current, and emerging trends in point-of-care

urinalysis tests. *Expert Review of Molecular Diagnostics*. 2020;**20**(1):69-84

[75] Shete MB, Patil TS, Deshpande AS, Saraogi G, Vasdev N, Deshpande M, et al. Current trends in theranostic nanomedicines. *Journal of Drug Delivery Science and Technology*. 2022;**71**:103280

[76] Jeelani S, Reddy RJ, Maheswaran T, Asokan G, Dany A, Anand B. Theranostics: A treasured tailor for tomorrow. *Journal of Pharmacy & Bioallied Sciences*. 2014;**6**(Suppl. 1):S6

[77] Li X, Shu J, Gu W, Gao L. Deep neural network for plasmonic sensor modeling. *Optical Materials Express*. 2019;**9**(9):3857-3862

[78] Ballard ZS, Shir D, Bhardwaj A, Bazargan S, Sathianathan S, Ozcan A. Computational sensing using low-cost and mobile plasmonic readers designed by machine learning. *ACS Nano*. 2017;**11**(2):2266-2274

[79] Tang L, Li J. Plasmon-based colorimetric nanosensors for ultrasensitive molecular diagnostics. *ACS Sensors*. 2017;**2**(7):857-875

[80] Tadimety A, Wu Z, Molinski JH, Beckerman R, Jin C, Zhang L, et al. Rational design of on-chip gold plasmonic nanoparticles towards ctDNA screening. *Scientific Reports*. 2021;**11**(1):1-10

[81] Rai P, Kumar BK, Deekshit VK, Karunasagar I, Karunasagar I. Detection technologies and recent developments in the diagnosis of COVID-19 infection. *Applied Microbiology and Biotechnology*. 2021;**105**(2):441-455





# Plasmonic Optical Nano-Antenna for Biomedical Applications

*Rasha H. Mahdi and Hussein A. Jawad*

## Abstract

Plasmonics attract significant attention of the researchers due to Plasmon's surpassing ability to match free space electromagnetic (EM) excitation into the nano-scale size and conduct the light-tissue interaction in this scale. Plasmonic nano-antennas (PNAs) is a coupling of EM waves into Localized Surface Plasmon Resonance (LSPR) which is considered as an interesting subject for theoretical and experimental study. This presents a new concept of the confinement of light in subwavelength scales with huge local fields which can generate very high near field intensities because of their LSPR. The generated field is invested in various applications that are depending on near field enhancement produced by plasmonic optical nano-antennas (PONAs) such as Surface-Enhanced Raman Spectroscopy (SERS), biosensing, spectral imaging and cancer treatment. Bowtie shape PNAs (PBNAs) can transfer the light field efficiently by converting the light from external space into a subwavelength spectral region with the improvement at an optical wavelength in a tiny area between its antenna arms. The local EM field production in a gap area is the main reason to suggest PBNAs shape if the frequency of the incident EM waves coincide the structural resonance peak so it is acting as a tunable hot spot.

**Keywords:** plasmonics, laser cancer treatment, biomedical applications

## 1. Introduction

The back bone of numerous applications in the recent years is the plasmonic nano-antennas especially in the optical spectral regions due to their unique properties, as high enhancement and subwavelength confinement of the electrical field. One of the attractive application is the treatment of the cancer cells where the diffusion of heat could be controlled via plasmonic nano-antennas and hence the temperature is confined in the diseased tissue. Nano-antennas are consisting of adjacent metallic nano-particles with nano-scales gaps (in particular the bowtie shape) which have excessively strong field confinement and enhancement in the gap region. The generated field is invested in various applications that are depending on near field enhancement produced by plasmonic optical nano-antennas (PONAs) such as cancer treatment. The heat produced and the thermal diffusion in the plasmonic structure are not richly investigated might be due to the shortage in the experiments. Vigorous potentials are conducted into the development of new techniques for the controlled temperature at the nano-scale and the destroying cell by the temperature rise due to the converting heat is also included.

In this chapter we try to highlight on the important aspects of the interaction of laser light with proposed cancer cells. A case study was designed and studied represented by a plasmonic bowtie nano-antenna. First of all, we have to design a suitable cell of nano-antenna considering the dimensions in nano scale. The second step is to select the shape because it represents the enhanced field source in addition to an appropriate noble metal due to the application of plasmonic bow-tie nano-antennas is conducted inside the human body. The wavelength of the laser used should be selected depending on the resonance frequency because the absorption is regarded the first step of the plasmonic generation. The field distribution is quite important to kill the diseased cells so, the angle of laser incidence and the distance to the tissue play the essential role in the effective process. The virtual tissue is irradiated by two laser wavelengths (532, 1064) nm through a single bowtie nano-antenna, The absorption of EM field that is transferred to heat in the human body depending on the incident EM power density is measured via SAR. It is written as Eq. (1) [1].

$$SAR = \sigma |E|^2 / 2\rho (Kg / w) \quad (1)$$

Where:

$\sigma$  = conductivity of the tissue-simulating material (S/m).

$E$  = total Root Mean Square (RMS) field strength (V/m).

$\rho$  = mass density of tissue-simulating material (kg/m<sup>3</sup>).

From the thermal energy deposited on the proposed tissue, the temperature elevation could be estimated as the following equation:

$$dQ = \rho V C dT \quad (2)$$

Where:

$Q$  = the thermal energy (J).

$V$  = the volume (m<sup>3</sup>).

$C$  = the specific heat (J /K. kg).

$T$  = the temperature in Kelvin (K).

Both sides in the equation could be divided by ( $\rho V dt$ ), then the terms are rearranged, so the following equation could be written as:

$$(dQ / dt) / \rho V = C.dT / dt \quad (3)$$

The specific absorption rate and the temperature elevation detection via the time period calculation are the main considered parameters. Finally, the main conclusions are extracted from the obtained results of the case study.

## **2. Plasmonics nano-antenna**

The optical field could be transformed into localized energy via a structure called optical nano-antennas (ONAs). Their structures have an ability to control and manipulate the optical field at subwavelength scales [2].

ONAs require engineering accuracies of the characteristic dimensions down to a few nano-meters while about to the wavelength scale in other antennas [3–6].

However, this downscaling holds the technological challenges of nano-scale antenna engineering [6, 7]. The antenna performance can be strongly enhanced by plasmon resonances that lead to high and confined fields. The optical excitation of ONAs with a suitable wavelength can produce very high near-field because of their LSPR [4].

The interaction of an intense electromagnetic field with electrons ejected freely at the interface between dielectric/metal results in a quantum electromagnetic phenomenon called surface plasmon resonance (SPR). Plasmonic is a field that deals with SPR. The interesting potential for engineering many devices and patterns involving nano-photonics are based on plasmonic nano-structures.

Plasmonic nano-antennas (PNAs), are able to controlling and confining EM field at the nano-scale. The performance evaluation of PNAs is depending on two important parameters, the absorption of the light and field improvement locally. A wide research areas invest the high light absorption, such as thermal emitters, solar thermal applications, thermal photoluminescences, and sensors. The improved electric fields at resonance wavelength can modulate the optical properties in the vicinity of molecules, so that, enhancing their light-matter interactions [8–10].

The tuning of the plasmon resonance for both absorption and emission to the excitation or the emission of species is the interesting research recently. The exciting EM field is enhanced several order of magnitude due to the production of what so-called hot spots when perfect nano-structures are designed. The structures working at plasmonic resonances open the ability to implement antennas working in the visible. The hot areas could be used to excite the effects at nonlinear regime so to match the EM field effectively. SERS and tip-enhanced Raman spectroscopy are the practical techniques that show the influence of such hot areas to observe the emitters with its sensitivity down to a single molecule [11].

The construction structure of PNAs is depending mainly on putting a gap at the sub-wavelength scale between two metallic areas, are gained distinguishable importance. This is mainly because of the hot spots in PNAs produce intensive EM field in nano-size overcoming the restriction of the diffraction. The confinement of the light field by BNAs is observed to be several order of magnitudes in the nano-scale smaller than the incident wavelength, as improved by the dimensions of the gap [12].

The resonance wavelength decisively depends on the shape, dimensions, and material of the antenna, a numerous variation of plasmonic antenna structures published proposed, such as bowties, nano-rings, nano-rod, and Yagi-Uda antennae. The sharp resonance wavelengths with narrow-band spectra with sharp are a major challenge for applications that require devices operating over a wide range of frequencies. For example, antennas used to improve energy harvesting efficiency of photovoltaic devices. Broadband PNAs are also highly wanted for SERS, fluorescence enhancement, and higher harmonic generation, which are multi-wavelength and broadband in nature [13].

## **2.1 Metal nano-antennas**

The intensity of the light, the dimensions of the components, and the material used are the essential parameters that produce plasmons excited by optical frequency. The suitable matters for this type of excitation are noble metals (i.e., gold (Au), silver (Ag), copper (Cu), and aluminum (Al)) so result in an important enhancement of the design and devices.

The nano-structures of metals with around area included in any design of optimized parameters need mainly the optical properties of PNAs especially in the

medical field. Among many metals, gold is a perfect metal against high-temperature oxidation with the best plasmonic characteristics and especially suitable for biocompatible applications.

Distinguished spectroscopic features (spatial, spectral) are observed in noble metal nano-antennas (MNAs) such as Au NPs and Ag NPs. MNAs have those features resulting from the oscillations of electrons collectively in the conduction band, which is LSPR [10].

MNAs can confine and improve near IR and visible field in superficially by the excitation of LSPR. The 'EM hot region (spot)' that could be created on the nano-antennas has excessively utilized the absorption of light locally leading to an increase the weak intensity in the nonlinear optical process [14].

Au nano-particles (Au NPs) could effectively absorb IR and visible field energy in quite concentrated sizes, getting them properly controllable heat source in subwavelength size. In addition to the great importance the mechanism of those phenomena to be investigated, the capability to generate point like heat nano-heat encourage a broad area of research in physics, chemistry, and biology. The aforementioned properties of Au NPs especially as a nano-sources are promising researchers in the catalysis at nano-size, photonics, and in the field of medicine for cancer cells destroying photo-thermally [15].

### **3. Heat generation in nano-antenna**

PNAs cause an exaggerated heat produced in the metal after the excitation of the external light source, producing a side hot areas—i.e., the elevation of the temperature in a restricted region which is a mainly undesirable effect in various research namely spectroscopy, sensing, and optical signal processing. Localized heat of PNAs, in another hand, is very useful in a group of applications such as nano-engineering, cancer treatment, nano-manipulation, hot vapor generation, and catalysis [14].

The local temperature elevation of MNAs is quite low thermal radiation in the mid-to-far IR wavelength spectral region. In addition, if (the mean free path) of the substrate materials is larger than the nano-antenna size, the heat converted the volume of metal volume may be reduced [16]. It is well known that the metals in nano-size create regional temperature gradients after external light exposure, quite enough to generate subwavelength areas of super-heated water surrounding the species [17].

Photo-induced heating of nano-antennas can vary their geometry because of the metal melting. The melting process can minimize the nano-range properties so, directly nano-antennas becomes nano-spheres if temperature increment is established. The variation of the morphology may affect on the antennas' spectral response and can decrease the near-field generation. The melting temperature of metal can take place at higher surface melting temperatures of nano-antennas [18, 19].

The pioneering author is previously shown that the structures of hybrid plasmonic have good selectivity and huge improvement of the near-field intensity due to effective trapping with re-cycling of photons in near IR and visible in photonic modes [20–22].

The IR thermal radiation could be produced and enhanced by the selection of the optimum parameters of materials and the dimensions regarding the geometry on a range at or under the emitted thermal peak resonance wavelength [14]. The convective and radiative cooling represent other ways to diffuse heat intensity from

nano-sizes, where became effective if the thermal conductivity is disturbed because of the particles in the nano-size [23].

#### **4. Specific absorption rate**

The extension result of the EM field is the elevation temperature of the tissue in a limited region caused by the generated heat which could affect on the biological system. The heat diffusion and its influence on the tissue are specified by the Specific Absorption Rate (SAR). SAR magnitude can not increase above the level of irradiation which becomes harmful. SAR magnitude is depending mainly on various factors such as the position of the antenna related the human tissue, the intensity field of the antenna, and the power.

The specific absorption rate (SAR) is an indication tool of absorption where the EM field exposure in the human body could be estimated. SAR is mainly used to measure the absorbed power in the tissues after irradiation by external field so that it gets the heat of tissue to be increased. The biological tissue heat could be checked via a safe method which is mainly depending on measuring the temperature elevation in tissues. It is mentioned that the temperature and SAR are evaluated in the human tissues so the precaution measures are verified. SAR is a function of many factors. Those factors affect on the absorption of EM field. SAR variations are depending on the properties of the wave, properties of the body and environment properties. Regarding the properties of the wave, the extent of SAR changes is depending directly on the features of the signal, such as frequency and polarization. In another side the dependence with the tissue human body, the SAR value depends on the type of tissue (e.g., geometry, size, age, and dielectric properties) and tissue orientation/exact location (e.g., the situation of the body; front or back incidence). SAR, in addition, depends on the exposure states, e.g., environmental exposure (indoor and outdoor) and influences of other objects in the field near the exposed body [24].

It is important to understand SAR calculation with respect to averaging design. There are two procedures to accomplish SAR calculations: first is point SAR, and second is averaging SAR (i.e., mass or volume). Point SAR is the value regardless of the averaging of the mass and the maximum SAR of all the grid cells is provided. When the absorbed power in each grid divided by grid mass, the point SAR is evaluated. While in the averaged SAR, a cube of known mass, e.g., 1 or 10 g, is utilized for every point, then the loss of the power density is integrated on this region. Then, the power loss in the integral form is divided by the mass cube [1, 24].

Because the electric field is usually not spatially uniform, SAR is averaged over a volume of tissue regarding the type of the source. It is useful to mention that the electric field is not fixed in time, so that, the probe is used for short-term time-averaging [1].

#### **5. Time period estimation**

The temperature is elevated in human tissues due to the absorption of power from EM fields. An irreversible damage of the tissue can take place due to the absorption of high power. The dielectric and thermal features of the proposed tissue model are used to evaluate the relationship between the temperature and the point SAR, it could be estimated considering the equation of heat (2) [25].

The SAR value is represented in the left side, so that the thermal distribution in tissues for a period of ( $\Delta t$ ) can be determined.

It can rewrite Eq. (4) as:

$$F=P/A. \quad (4)$$

It is worth to mention that the short time period is quite important in the treatment of the diseased tumor cells because of the generated heat does not dissipated to the surrounding healthy tissues, for this reason the calculated time period in this study does not possible unless using the laser either in pulse mode or in chopped mode.

## **6. Design of nano-antenna**

From the various type of optical nano-antenna, the bowtie shape is the preferred choice in this study, as compared with a dipole [26]. Plasmonic BNAs is usually designed due to the confinement of the electric field in the gap region, working at higher frequencies, and keeping the whole size much smaller (nano-meter) [9]. Regarding the sharp tips of the two arms of the bowtie antenna, the group and phase velocities of surface plasmonic waves decrease with the distance of propagation and finally become zero [27]. BNAs are expected to possess a relatively broad bandwidth because they represent the two-dimensional analogue of a biconical antenna [28]. The localized plasmonic near-field, which is highly sensitive to the refractive index of its surrounding medium can be tuned by adapting the nano-structure shape. Geometrical parameters such as size, gap distance, height, and bowtie apex angle have a direct effect in the LSPR [29].

## **7. Single unit plasmonic bowtie nano-antenna**

Bowtie shape PNAs (PBNAs) can transfer the light field efficiently by converting the light from external space into a subwavelength spectral region with the improvement at an optical wavelength in a tiny area between its antenna arms.

First of all, initial dimensions are selected to design primary bowtie shape nano-antenna by sitting the length of nano-antenna is ( $L$ ), the width is ( $W$ ), the thickness is ( $T$ ), the apex width is ( $A$ ), the gap width is ( $G$ ) and the bowtie apex angle is ( $\Theta_0$ ) [30], as shown in **Figure 1a**.

The bowtie structure is normally illuminated by linearly polarized waveguide excitation source along the x-axis (x-polarization). The surrounding environment of the design structure is assumed to be air. as shown in **Figure 1b**.

## **8. The proposed tumor tissue model**

The proposed tumor represents cancer cells in the skin tissue located in the center of the skin structure as shown in **Figure 2**.

The thermal properties of the tissue are listed in **Table 1**. In addition, the dielectric properties of the tissue play an important role in the investigation of the

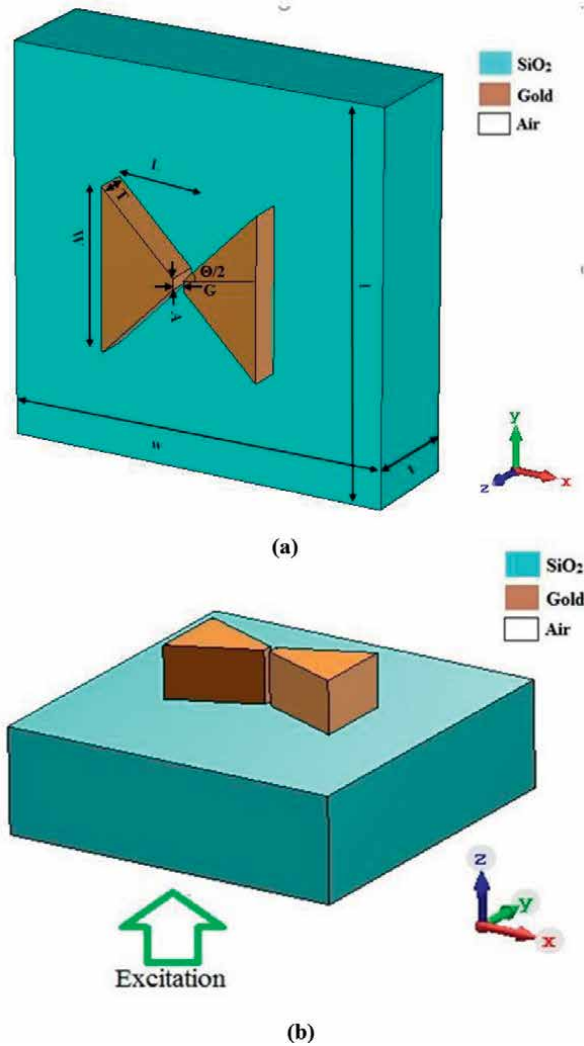


**Figure 1.**  
(a) Schematic diagram of single 3D plasmonic nano-antenna with dimensions of the length of nano-antenna is ( $L$ ), the width is ( $W$ ), the thickness is ( $T$ ), the apex width is ( $A$ ), the gap width is ( $G$ ) for the gold and the length ( $l$ ), width ( $w$ ), thickness ( $t$ ) for the  $\text{SiO}_2$ , and (b) the direction of excitation.

propagation characteristic of the plasmonic optical nano-antenna. These properties are mainly depending on tissue type and the wavelength of interest.

### 8.1 Exposing the tumor to the designed nano-antenna

The designed tissue is subjected to the plasmonic nano-antenna (single and an array) radiation at different distances, the resulted pattern is shown in **Figure 3**.

The designed structure was illuminated normally by a waveguide source linearly polarized along the x-axis as shown in **Figure 3**. The proposed tissue is located in the upper edge of the antenna and centered in front of the gap of the nano-antenna. The structure is surrounded by the air.

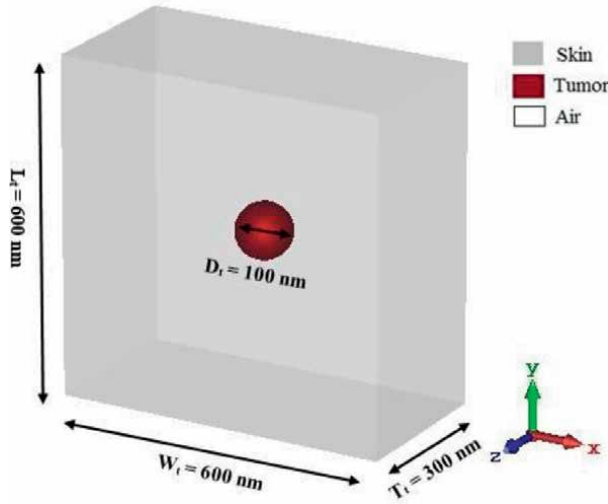


**Figure 2.** 3D schematic view of the tumor embedded in the skin tissue. The dimensions are ( $L = W = 600$  nm and  $T = 300$  nm).

Tissue	Thermal conductivity K (W/m)	Specific heat C (kJ/K/kg)	Mass density $\rho$ (kg/m <sup>3</sup> )
Skin	0.2	3.6	1200
Tumor	0.5	3.6	1050

**Table 1.** The properties of the tissues.

## 9. Specific absorption rate calculations

The estimation of the temperature distribution of any tumor embedded in a tissue exposed to a light source is quite complicated due to the nature and the location of tissues. In the present study, the time of reaching the temperature to be fair enough for destroying the diseased cells is estimated through the calculation of SAR.

### 9.1 Specific absorption rate at 532 nm for single nano-antenna

The optimized single NA working at resonance wavelength 532 nm is located at different distances from the tissue (100, 200, 300 and 400) nm to calculate the SAR for each as illustrated in **Figure 4a–d**. The point SAR inside the proposed tissue are ( $1.83 \times 10^{11}$ ,  $1.19 \times 10^{11}$ ,  $8.22 \times 10^{10}$ , and  $4.72 \times 10^{10}$ ) W/kg for distances (100, 200, 300 and 400) nm respectively. It is observed clearly that the SAR reduces with increases the distance because the reduction of the strength of the receiving far-field. The field is concentrated in the center of the tumor which means that the surrounding tissues are not affected by the field.

The behavior of SAR related to the distance from the proposed tissue at the wavelength of 532 nm for single NAs is shown in **Figure 5**. The SAR is increased with closer distance and the maximum value of SAR is detected for single unit.



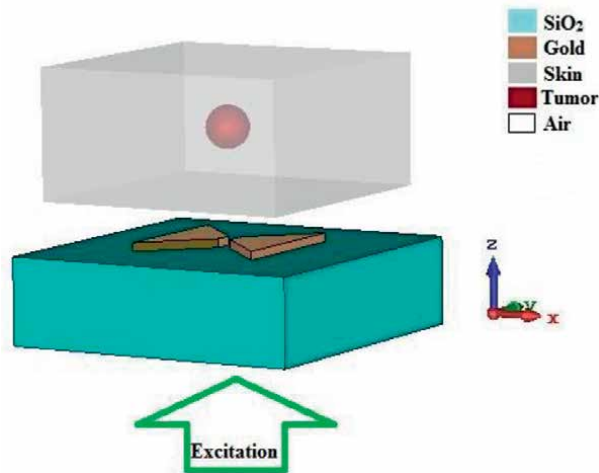


**Figure 3.**  
*The final pattern of bowtie nano-antenna in front of the designed tissue.*

## 9.2 Specific absorption rate calculations at 1064 nm single nano-antenna

**Figure 6a–d** shows the distribution of the field in the tissue after subjecting to single NA at 1064 nm for various distances (100, 200, 300 and 400) nm. The point SAR inside the proposed tissue could be calculated. The maximum values of SAR are  $(2.28 \times 10^{11}, 1.17 \times 10^{11}, 8.49 \times 10^{10}, \text{ and } 8.11 \times 10^{10})$  W/kg for distances (100, 200, 300, and 400) nm respectively. It is noticed that the point SAR value is not varied clearly at this wavelength.

**Figure 7** shows the behavior of SAR as a function of different distances at the wavelength of 1064 for single NAs. Similar behavior is detected for both wavelengths but it is noticed that sharp reduction from single to an array structures.

It is obvious that the distribution of the far-field in the tumor is varied for two resonance wavelengths (532 and 1064) nm where the field is appeared out the tumor in the case of 1064 nm. This distribution may affect on the healthy surrounding tissues which are not preferred in this type of application although the strength of the field is suitable. In addition, it is well observed that the SAR increases with the closest distance.

## 10. Time period estimation

The temperature elevation in the irradiated tissues could be estimated easily related to the SAR calculations owing to Eq. (1). It is noticed from this equation that the temperature elevation in the tissue is depending mainly on the time period of exposing to NAs for a certain SAR, so the time period should be selected carefully to verify the wanted temperature for tumor cells killing.

### 10.1 Time period estimation in tumor tissue at single nano-antenna

The main goal of the treatment of the tumors is the temperature rise over the normal level to cause cells damage which could be estimated by  $(60^\circ\text{C})$ . **Table 2**

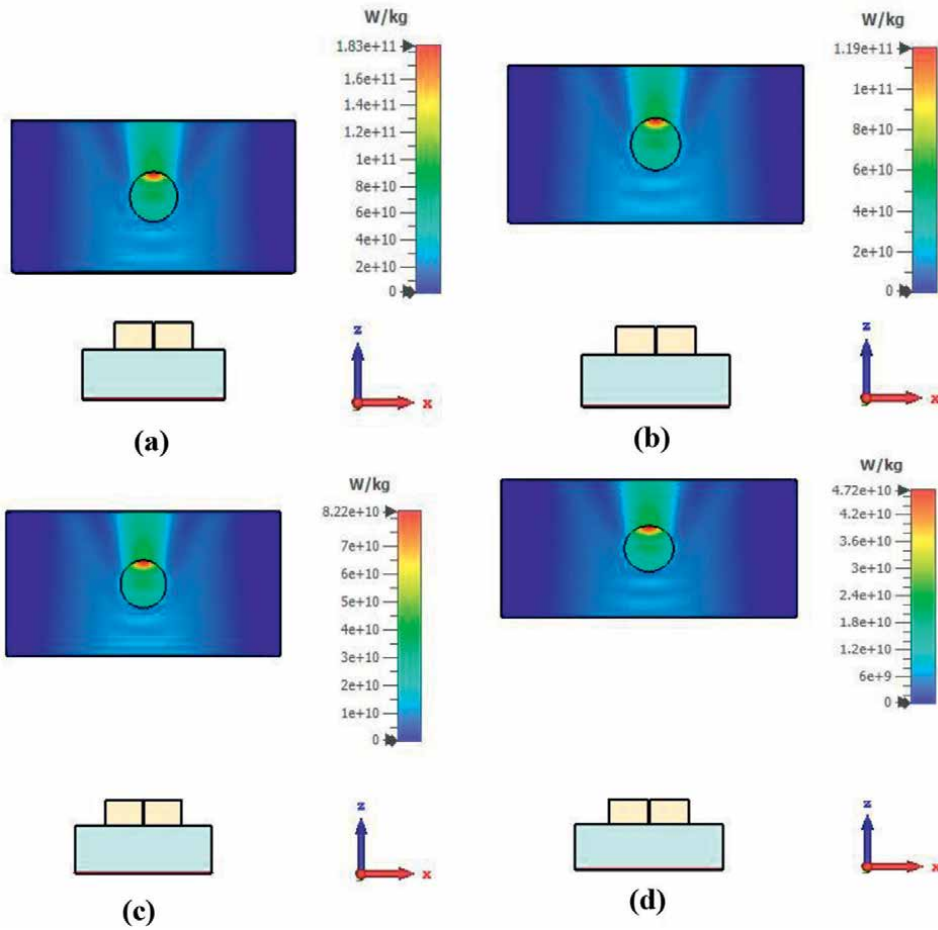


**Figure 4.** The calculated SAR in the proposed tumor tissue exposed to a single NA at 532 nm for different distances. (a) 100 nm, (b) 200 nm, (c) 300 nm, and (d) 400 nm.

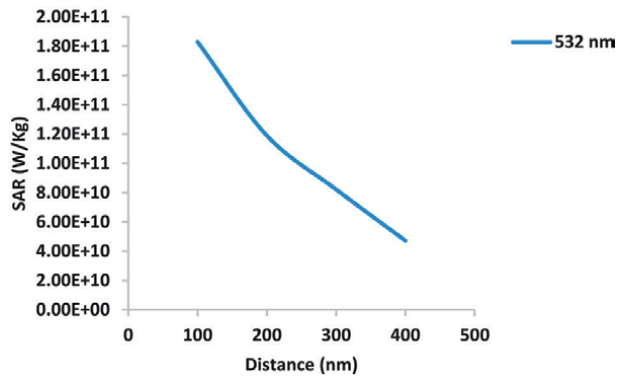


**Figure 5.** Specific absorption rate as a function of the distance from the tissue at single unit for 532 nm.

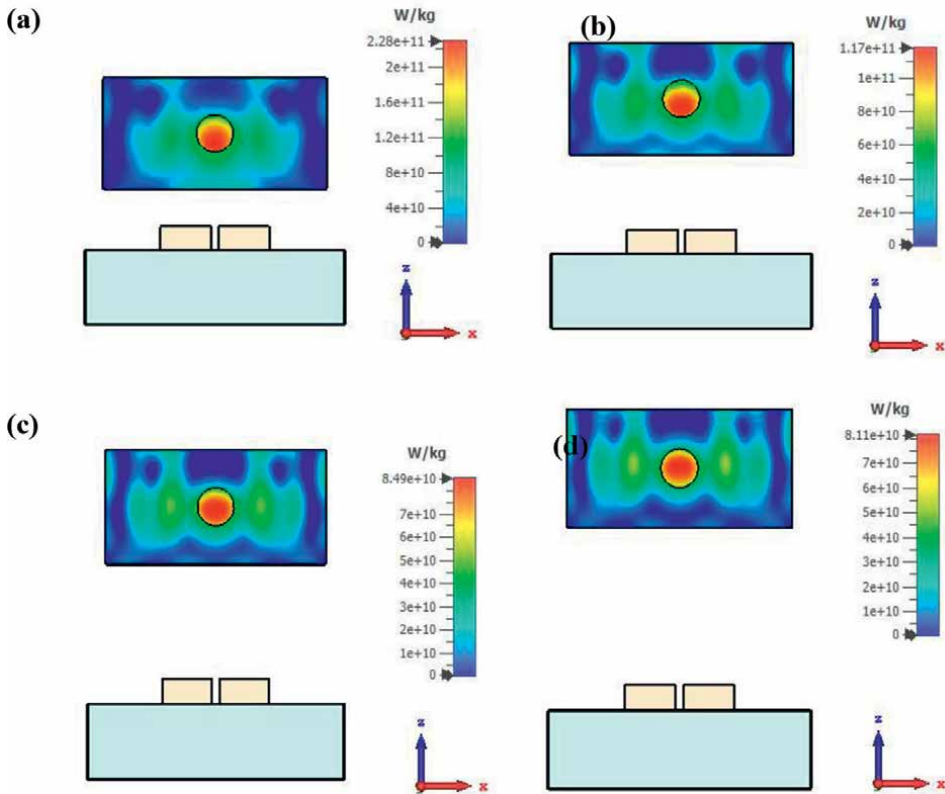


**Figure 6.** The calculated SAR in the proposed tumor tissue subjected to single NA at 1064 nm at different distances (a) 100 nm, (b) 200 nm, (c) 300 nm, and (d) 400 nm.

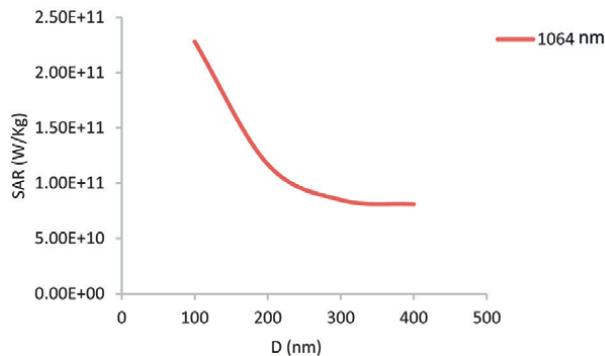


**Figure 7.** The specific absorption rate as a function of the distance from the proposed tissue at 1064 nm for single unit.

represents the time period estimation to attain the required temperature in the proposed tumor tissue for single NA at two wavelengths (532 and 1064) nm for different distances (100, 200, 300 and 400) nm from the tissue. It is clear that the time period is shorter for closer distance from the tissue for both wavelengths while it shortest for

Distance D (nm)	Time period ( $\mu$ s)	
	532 nm	1064 nm
100	6.55	5.26
200	10.1	10.2
300	14.6	14.1
400	25.4	14.8

**Table 2.**

*The calculation of the time period in the proposed for distances (100, 200, 300 and 400) at two wavelengths (532 and 1064) nm for single nano-antenna.*

longer wavelength (1064 nm). It is observed from the results that the time period is varied related to the field distribution in the tissue and how much regular and hence for SAR calculation.

It is worth to mention that the short time period is quite important in the treatment of the diseased tumor cells because of the generated heat does not dissipated to the surrounding healthy tissues, for this reason the calculated time period in this study does not possible unless using the laser either in pulse mode or in chopped mode.

The optical plasmonic nanoantenna proves high ability to destruct the tumor tissues especially the cancer cells due to those antennas are considered as a hot point source which means that the desired tissue could be destroyed without affecting the surrounding healthy tissues. Our purpose is to estimate the thermal distribution in the tissue at different distances from the nanoantenna. The bow tie shape of plasmonic nanoantenna is selected because in the sharp tip the group and phase velocities of surface plasmonic waves decreases with the distance of propagation and finally become zero. The generated field could be enhanced several order of magnitude in the gap, so the gap width should be selected accurately. The calculated results of the SAR proved that the best value is the closest to the tissue which causes to the higher temperature generated in it, knowing that the resonance wavelength is varied related to every distance and does not represent the best.

The maximum temperature generated in the tissue under the influence of optical plasmonic bow tie nanoantenna is detected at a distance of 100 nm, which gives a clear indication that the distance from the tissue affects on the distribution field in the tissue and hence on the temperature elevation.

## 11. Conclusions

Plasmonic Bowtie nanoantennas are designed for single structure at two resonance wavelengths (532, 1064) nm then applied to a proposed skin tissue with a certain environment. The temperature elevation in the tissues is evaluated to estimate its ability to use it as an effective tool for destroying the cancer cells. From the extracted results, it could be concluded:

- The design parameters have a mutual effect on each other at various rates but the length of antennas seems the higher influence.
- Higher near field intensity is detected for single NA at 532 nm than for 1064 nm while the near-field is improved for the resonance wavelength 1064 nm.

- The detected far-field intensity is higher for 532 nm in a single wavelength.
- The distribution of the intensity field in the skin tissues is directly influenced by the resonance wavelength and hence its strength.
- The closest distance of different structures to the treated tissue the better field distribution that raises the temperature.
- The SAR results are higher for short distance (100 nm) according to the field intensity distribution in the tissue.
- The required time period is depending on the SAR taken into account the required temperature for killing tumor cells.
- It is finally concluded that this technique is encouraged to be an effective therapy for destroying the cancer cells.

## **Author details**

Rasha H. Mahdi<sup>1\*</sup> and Hussein A. Jawad<sup>2</sup>


1 Laser and Optoelectronics Department, College of Engineering, Al-Nahrain University, Jadriya, Baghdad, Iraq

2 Institute of Laser for Postgraduate Studies, University of Baghdad, Baghdad, Iraq

\*Address all correspondence to: [rasha.h.mahdi@nahrainuniv.edu.iq](mailto:rasha.h.mahdi@nahrainuniv.edu.iq)

## **IntechOpen**

---

© 2022 The Author(s). Licensee IntechOpen. This chapter is distributed under the terms of the Creative Commons Attribution License (<http://creativecommons.org/licenses/by/3.0>), which permits unrestricted use, distribution, and reproduction in any medium, provided the original work is properly cited. 

## References

- [1] Hochwald BM, Love DJ, Yan S, Jin J. SAR codes. In: 2013 Information Theory and Applications Workshop (ITA). Conference. San Diego, CA, USA: IEEE; 2013. pp. 1-9
- [2] Novotny L, van Hulst N. Antennas for light. *Nature Photonics*. 2011;5(2):83-90
- [3] Mühlischlegel P, Eisler H-J, Martin OJF, Hecht B, Pohl DW. Resonant optical antennas. *Science*. 2005;308(5728):1607-1609
- [4] Taminiou TH, Moerland RJ, Segerink FB, Kuipers L, van Hulst NF.  $\lambda/4$  resonance of an optical monopole antenna probed by single molecule fluorescence. *Nano Letters*. 2007;7(1):28-33
- [5] Ghenuche P, Cherukulappurath S, Taminiou TH, van Hulst NF, Quidant R. Spectroscopic mode mapping of resonant plasmon nanoantennas. *Physical Review Letters*. 2008;101(11):116805
- [6] Kinkhabwala A, Yu Z, Fan S, Avlasevich Y, Müllen K, Moerner WE. Large single-molecule fluorescence enhancements produced by a bowtie nanoantenna. *Nature Photonics*. 2009;3(11):654-657
- [7] Kalkbrenner T, Håkanson U, Schädle A, Burger S, Henkel C, Sandoghdar V. Optical microscopy via spectral modifications of a nanoantenna. *Physical Review Letters*. 2005;95(20):200801
- [8] Anger P, Bharadwaj P, Novotny L. Enhancement and quenching of single-molecule fluorescence. *Physical Review Letters*. 2006;96(11):113002
- [9] Yousif BB, Samra AS. Modeling of optical nanoantennas. *Physical Review Letters*. 2012;2012(321075):10
- [10] Li Y, Li D, Chi C, Huang B. Achieving strong field enhancement and light absorption simultaneously with plasmonic nanoantennas exploiting film-coupled triangular nanodisks. *Journal of Physical Chemistry C*. 2017;121(30):16481-16490
- [11] Fischer H, Martin OJF. Engineering the optical response of plasmonic nanoantennas. *Optics Express*. 2008;16(12):9144-9154
- [12] Li Z, Hattori HT, Parkinson P, Tian J, Fu L, Tan HH, et al. A plasmonic staircase nano-antenna device with strong electric field enhancement for surface enhanced Raman scattering (SERS) applications. *Journal of Physics D: Applied Physics*. 2012;45(30):305102
- [13] Yong Z, Gong C, Dong Y, Zhang S, He S. Broadband localized electric field enhancement produced by a single-element plasmonic nanoantenna. *RSC Advances*. 2017;7(4):2074-2080
- [14] Boriskina SV, Weinstein LA, Tong JK, Hsu W-C, Chen G. Hybrid optical-thermal antennas for enhanced light focusing and local temperature control. *ACS Photonics*. Sep. 2016;3(9):1714-1722
- [15] Baffou G, Girard C, Quidant R. Mapping heat origin in plasmonic structures. *Physical Review Letters*. 2010;104(13):136805
- [16] Chen G. Nonlocal and nonequilibrium heat conduction in the vicinity of nanoparticles. *Journal of Heat Transfer*. 1996;118(3):539-545
- [17] Carlson MT, Green AJ, Richardson HH. Superheating water by CW excitation of gold nanodots. *Nano Letters*. 2012;12(3):1534-1537

- [18] Roxworthy BJ, Bhuiya AM, Inavalli VVGK, Chen H, Toussaint KC. Multifunctional plasmonic film for recording near-field optical intensity. *Nano Letters*. 2014;**14**(8):4687-4693
- [19] Ahn W, Boriskina SV, Hong Y, Reinhard BM. Electromagnetic field enhancement and spectrum shaping through plasmonically integrated optical vortices. *Nano Letters*. 2012;**12**(1):219-227
- [20] Boriskina SV, Reinhard BM. Adaptive on-chip control of nano-optical fields with optoplasmonic vortex nanogates. *Optics Express*. 2011;**19**(22):22305-22315
- [21] Ahn W, Boriskina SV, Hong Y, Reinhard BM. Photonic-plasmonic mode coupling in on-chip integrated optoplasmonic molecules. *ACS Nano*. 2012;**6**(1):951-960
- [22] Boriskina SV, Reinhard BM. Spectrally and spatially configurable superlenses for optoplasmonic nanocircuits. *Proceedings of the National Academy of Sciences*. 2011;**108**(8):3147-3151
- [23] Chen G. Nonlocal and Nonequilibrium Heat Conduction in the Vicinity of Nanoparticles. *Journal of Heat Transfer*. 1996;**118**(3):539-545
- [24] Hamed T, Maqsood M. SAR Calculation & Temperature Response of Human Body Exposure to Electromagnetic Radiations at 28, 40 and 60 GHz mmWave Frequencies. *Progress In Electromagnetics Research*. 2018;**73**:47-59
- [25] Sallomi AH. A theoretical approach for SAR calculation in human head exposed to RF signals. *Journal of Engineering and Development*. 2012;**16**:10
- [26] Fischer H, Martin OJF. Engineering the optical response of plasmonic nanoantennas. *Optics Express*. 2008;**16**(12):9144-9154
- [27] Jayaswal G, Belkadi A, Meredov A, Pelz B, Moddel G, Shamim A. A zero-bias, completely passive 28 THz rectenna for energy harvesting from infrared (waste heat). In: 2018 IEEE/MTT-S International Microwave Symposium—IMS. Conference. Philadelphia, PA, USA: IEEE; 2018. pp. 355-358
- [28] Calderón J, Alvarez J, Pastor JM, Hill D. Bowtie plasmonic nanoantenna arrays for polarimetric optical biosensing. In: *Frontiers in Biological Detection: From Nanosensors to Systems VI*. Conference. Vol. 8933. San Francisco, California, United States: SPIE; 2014. p. 893301
- [29] Biagioni P, Huang J-S, Hecht B. Nanoantennas for visible and infrared radiation. *Reports on Progress in Physics*. 2012;**75**(2):024402
- [30] Mahdi RH, Jawad HA. Thermal response of skin diseased tissue treated by plasmonic nanoantenna. *International Journal of Electrical and Computer Engineering*. 2020;**10**(3):2969-2977



*Edited by Patrick Steglich*

Plasmonics includes the fundamentals of surface plasmon polaritons in metals, and its rapidly increasing applications in biochemistry, nanotechnology, optical communication, sensing, and medicine. Surface plasmon polaritons have become popular because of their ultrasensitive optical measurement capabilities, and in recent years they have also been employed for ultra-high-speed data transfer. This book presents recent advances in the broad field of plasmonics, covering not only current progress and the latest breakthroughs in emergent applications but also geometry optimizations and the fundamentals of physical interactions.

Published in London, UK

© 2023 IntechOpen  
© Iuchschen / iStock

**IntechOpen**

